



UNIVERSIDAD NACIONAL AUTÓNOMA DE MÉXICO
PROGRAMA DE POSGRADO EN CIENCIAS DE LA TIERRA
CENTRO DE GEOCIENCIAS
GEOQUÍMICA Y PETROLOGÍA

MODELO HIDROGEOLOGÍCO MULTIDISCIPLINARIO DE LA CUENCA DE SAN JUAN DEL RÍO, QUERÉTARO, MEXICO.

TESIS QUE PARA QUE PARA OPTAR POR EL GRADO DE:
DOCTORADO EN CIENCIAS DE LA TIERRA

PRESENTA:
MSc. ELISEO HERNÁNDEZ PÉREZ

TUTOR PRINCIPAL
Dr. GILLES PIERRE RENÉ LEVRESSE
Centro de Geociencias, UNAM Campus Juriquilla

MIEMBROS DEL COMITÉ TUTOR
Dra. DORA CELIA CARREÓN-FREYRE
Dr. JAIME JESÚS CARRERA-HERNÁNDEZ
Centro de Geociencias, UNAM Campus Juriquilla

CDMX, OCTUBRE 2022



UNAM – Dirección General de Bibliotecas

Tesis Digitales
Restricciones de uso

DERECHOS RESERVADOS ©
PROHIBIDA SU REPRODUCCIÓN TOTAL O PARCIAL

Todo el material contenido en esta tesis está protegido por la Ley Federal del Derecho de Autor (LFDA) de los Estados Unidos Mexicanos (Méjico).

El uso de imágenes, fragmentos de videos, y demás material que sea objeto de protección de los derechos de autor, será exclusivamente para fines educativos e informativos y deberá citar la fuente donde la obtuvo mencionando el autor o autores. Cualquier uso distinto como el lucro, reproducción, edición o modificación, será perseguido y sancionado por el respectivo titular de los Derechos de Autor.

HOJA EN BLANCO

DECLARATORIA DE ÉTICA

Declaro conocer el Código de Ética de la Universidad Nacional Autónoma de México, plasmado en la Legislación Universitaria. Con base en las definiciones de integridad y honestidad ahí especificadas, aseguro mediante mi firma al calce que el presente trabajo es original y enteramente de mi autoría. Todas las citas de, o referencias a la obra de otros autores aparecen debida y adecuadamente señaladas, así como acreditadas mediante los recursos editoriales convencionales.



Eliseo Hernández Pérez

AGRADECIMIENTOS.

El desarrollo de este estudio fue posible gracias al patrocinio del proyecto CONACYT CB-255070 otorgado a Gilles Levresse, UNAM-DGAPA PAPIIT IV100117 otorgado a Luca Ferrari, Gilles Levresse y José Antonio Hernandez Espriú, y al programa de beca CONACYT otorgado que me fue otorgado. Agradezco al Centro de Geociencias de la Universidad Autónoma de México (UNAM), campus Juriquilla por recibirme permitirme ser parte de su comunidad por el apoyo económico, logístico y de infraestructura que me permitió desarrollar mis estudios de doctorado. Agradezco especialmente al Dr. Gilles Levresse por aceptarme como estudiante, por sus enseñanzas y por la confianza depositada en mí. Agradezco a la Dra. Dora Celia Carreón Freyre, Dr. Jaime Jesús Carrera Hernández, Dra. Penélope López Quiroz, Dr. Juventino Martínez Reyes, Dr. Jaime Alejandro Carrillo Chávez, Dr. Luis Walter Daesslé, Dr. Pedro Abelardo Morales Puente, Dr. José Antonio Hernández Espriú, Dr. Luis Mariano Cerca Martínez, Dra. Rocío García Martínez, por ser parte del comité y asesores que me apoyaron y enriquecieron el proyecto con sus observaciones y comentarios a través de las diferentes evaluaciones. Al Dr. Fernando Corbo-Camargo, Ing. Raúl Roberto Sánchez García por su apoyo en el tratamiento, inversión e interpretación de la geofísica. A Marta Pereda Miranda, Blanca Lilia Rendón Juárez, Armando Ramírez Morán, Alexander Correa-Metrio por su invaluable apoyo a través de la oficina de Posgrado. A Lic. Dionisio León Salas, Ing. José Guadarrama Delgadillo, Ing. Carlos Hernández Cabrera, Ángel Muñoz Torres, José Alberto Arévalo, Asucena Ortega Correa, Ing. Emilio Nava, Liliana Cabrera Hernández, Rodolfo Hernández Fuentes y todo el personal administrativo del Centro de Geociencias por su apoyo en las actividades administrativas, trabajo de campo y asistencia a congresos realizadas a través de este periodo. Al laboratorio de Geoquímica Ambiental del Centro de Geociencias, UNAM y la M. en C. Carolina Muñoz Torres por sus enseñanzas y el apoyo prestado en el trabajo analítico de las muestras. Al laboratorio de Geoquímica de Aguas del Centro de Geociencias, UNAM y Fabián González Quijas por su apoyo en la preparación de material de campo y tratamiento de muestra. Al laboratorio LUGIS del Instituto de Geología y al Dr. Pedro Morales Puente, M. en C. Edith Cienfuegos

Alvarado y M. en C. Francisco Javier Otero Trujano por su apoyo en el tratamiento de muestras y análisis de isotopía. Al laboratorio de Fluidos Corticales del Centro de Geociencias, UNAM y a la Dra. Marina Vega González por el apoyo en el tratamiento de muestra y uso del equipo de DRX y la interpretación de resultados. Al laboratorio de Mecánica Multiescalar de Geosistemas del Centro de Geociencias UNAM y a Ricardo Carrizosa Elizondo por su apoyo en las actividades realizadas. A todos los Doctores y Maestros que han aportado a mi formación. A la Dra. Lucía Capra Pedol, Dr. Gerardo Carrasco Nuñez, Juan Pablo Bernal Uruchurtu, Dr. Angel Nieto, Dra. Susana Alaniz, Dr. Adrián Ortega, Dra. Marina Vega. Al Dr. Luca Ferrari y a la Dra. Paola Andrea Montoya Lopera, así como a Seequent Limited por otorgar una licencia académica del software Leapfrog Geo. A Karen Velázquez Pedroza, Andrea Billarent Cedillo, Argelia Silva Fragoso, Jorge López Alvis, Claudio Inguaggiato y Löic Peiffer por su apoyo en las salidas de campo, cursos y escritura. Agradezco sinceramente a el Ing. Ignacio Ortiz Villaseñor y personal de la Comisión Estatal de Aguas Querétaro. Al Lic. Enrique Raúl Bustos Zúñiga la Junta de Agua Potable y Alcantarillado Municipal que apoyaron al desarrollo del proyecto con información, soporte logístico y acceso a las instalaciones a lo largo de este estudio. Ing. Audel Torres Vallejo y a personal del Comité Técnico de Aguas Subterráneas del Acuífero del Valle de Amazcala, Ing. Francisco Javier Sancén Contreras†, Lic. Cynthia Paola Ramírez Hernández y personal del Comité Técnico de Aguas Subterráneas del Acuífero del Valle de San Juan del Río. A la M. en C. María Eugenia Ortega Morín, Dr. Miguel Ángel Rea López, Dr. Miguel Ángel Rico, Q. A. María Leonor Barrón Lugo†, M en C. Gustavo Pedraza Aboytes y todos mis maestros, colegas y alumnos de la Facultad de Química de la Universidad Autónoma de Querétaro. A mis amigos Fernando Jáquez Sanabria, Agustín Valencia Trejo, Adolfo Pacheco Castro, Emmanuel Ramírez, Ernesto López Briceño, Avith Mendoza Ponce, Joselin de Lourdes Almaguer Rodríguez, Vania Ferrer Parra, Oscar Ávila Vargas, Lenin Valdez, Pedro Vitor Franco, Rodrigo León Loya, Francisco Chacón Hernández y a todos mis compañeros de CGeo con los cuales tuve convivencia en salidas de campo, organización y asistencia a congresos. Muchas Gracias a todos por haber formado parte de esta gran etapa.

RESUMEN:

El agua subterránea es una de las principales fuentes de abastecimiento de agua potable para la población, agricultura y actividades industriales. En México el 70% del territorio está conformado por zonas áridas y semiáridas; por lo que el agua subterránea se convierte en un recurso indispensable para el desarrollo social y económico de estas zonas. Los sistemas hidrogeológicos en el centro de México son complejos ya que a lo largo del ciclo hidrológico interviene varios factores limitantes en la recarga y flujo subterráneo, tanto ambientales, climáticos, geológicos y geoquímicos.

El acuífero del Valle de San Juan del Río (AVSJR) es el acuífero más grande en el estado de Querétaro, con una extensión de 2,800 km². Con un volumen de extracción concesionado que representa el 47% del total concesionado a nivel estatal. Actualmente se reporta un déficit de recarga anual de 130 millones de m³ causando un abatimiento en los niveles de agua subterránea de entre 4 a 7 m al año. La evolución geológica del Valle de San Juan del Río es muy compleja al encontrarse en los límites de las provincias geológicas de la Faja Volcánica Trans Mexicana (FVTM), La Sierra Madre Occidental (SMOc) y la Sierra Madre Oriental (SMOr) y en el centro de las calderas volcánicas de Amazcala, Amealco y Huichapan.

El modelo geológico/geofísico de la cuenca San Juan del Río se realizó a partir de la integración de literatura científica, registros de perforación, registros litológicos, reinterpretación de métodos geofísicos (SEV, TEM) y análisis de Difracción de Rayos X (DRX). En este trabajo, se logró definir la geometría del acuífero, así como sus principales unidades hidroestratigráficas, y principales zonas

que están siendo afectadas por alteración hidrotermal. El acuífero de San Juan del Río se conforma de 3 reservorios principales 1) un acuífero colgado en la zona serrana del Sierra de Vaquerías 2) acuífero libre pseudogranular en el valle con un espesor de entre 100 y 200 m que sobreyace a 3) un acuífero fracturado con espesores de entre 150 y 300 m de profundidad. El modelo geológico/geofísico reveló una unidad de baja resistividad electromagnética en la porción sur de la cuenca. El modelo hidrogeoquímico permite identificar 3 grupos de agua subterránea, así como, diferenciar las aguas de recarga meteóricas locales e hidrotermales de carácter regional.

Los datos de isotopía estable obtenidos en las aguas meteóricas permiten determinación de una Línea Meteórica Local (LMWL; $\delta^2\text{H}=7.61\delta^{18}\text{O}+5.89$) así como tres líneas de evaporación local a elevaciones de 2600, 2300 y 2000 msnm ($\text{LML}_1=\delta^2\text{H}=7.61\delta^{18}\text{O}+5.89$; $\text{LML}_2=\delta^2\text{H}=7.61\delta^{18}\text{O}+5.89$, $\text{LML}_3=\delta^2\text{H}=7.61\delta^{18}\text{O}+5.89$ respectivamente). El gradiente isotópico en la precipitación por efecto de altitud es de $\delta^2\text{H}=1.90\text{‰}$ y $\delta^{18}\text{O}=0.28\text{‰}$ por cada 100 m de elevación. La composición isotópica del vapor de agua atmosférico ($n = 47$) tiene un promedio de -79.4‰ ($\sigma = 24.3$) para $\delta^2\text{H}$; y de -13.2‰ ($\sigma = 3.5$) para $\delta^{18}\text{O}$. El modelo de evaporación isotópico de Craig-Gordon indica una perdida por evaporación del 53% en volumen, lo que representa un equivalente de 531 y 768 mm para los años 2016 y 2017 respectivamente. Los isótopos de $\delta^{13}\text{C}$ y $\Delta^{14}\text{C}$ permiten diferenciar dos acuíferos someros, uno en el valle de San Juan del Río con tiempo de residencia de 5,400 a 9,000 años y otro colgado en la Sierra de Vaquerías con tiempos de residencia del agua subterránea de 1,000 a 2,000 años.

El modelo de mezcla fue realizado a partir de un análisis de componentes principales (PCA) con los 3 reservorios hidrogeoquímicos principales identificados, permite estimar los porcentajes de mezcla para las aguas subterráneas en el valle de San Juan del Río. El Miembro Terminal meteórico de agua fría (A; de bajo de

30°C) se caracteriza por una composición de Ca-Mg-HCO₃ y un miembro final hidrotermal es enriquecido en Na, K, SO₄ y Cl, con temperatura hasta 90°C. La proporción principal es de origen meteórica (Componente A) con porcentaje de entre 40% a 60% del agua total. El agua almacenada en el acuífero (Componente B) con porcentajes de entre 18% a 38% representa el segundo reservorio por importancia. Por fin, flujo vertical ascendente de carácter hidrotermal (Componente C) con aportes de entre 2.4% a 41.6 % completa la estimación. A pesar de su rango de temperatura anómalo, del componente hidrotermal (C), Las relaciones isotópicas de helio muestran el aporte de fluidos hidrotermales y su mezcla con aguas someras en regiones tectónicamente activas. Lo que sugieren que la fuente de He proviene del manto sublitosférico a través de flujo regional falla regionales corticales de dirección principales N-S.

Palabras Claves

Isótopos estables de δ²H-δ¹⁸O-δ¹³C, Modelo Craig-Gordon, Hidrogeoquímica, Fechamiento por radiocarbono, Isótopos de helio Extensión cortical, Energía geotérmica, Ambiente semiáridos.

ABSTRACT:

Groundwater is one of the main sources of water supply for the population, agriculture and industrial activities. In México, 70% of the territory is made up of arid and semi-arid zones; Therefore, groundwater becomes an important resource for social and economic development in these areas. Hydrogeological systems in central Mexico are complex since several limiting factors (environmental, climatic, geological and geochemical) are involved in groundwater recharge and underground flow, throughout the hydrological cycle.

The San Juan del Río Valley aquifer (AVSJR) is the largest aquifer in the state of Querétaro, with an area of 2,800 km². With an authorized groundwater extraction volume that represents 47% of the total in the the state level. Currently, an annual recharge deficit of 130 million m³ is reported, causing a drop in groundwater levels of between 4 to 7 m per year. The geological geometry of the San Juan del Río Basin aquifer is very complex; as it is located on the limits of the geological provinces of the Trans-Mexican Volcanic Belt (FVTM), the Sierra Madre Occidental (SMOc) and the Sierra Madre Oriental (SMOr) and in the center of the volcanic calderas of Amazcala, Ameaco and Huichapan.

The geological/geophysical model of the San Juan del Río basin was assembled from the integration of scientific literature, drilling records, lithological records, reinterpretation of geophysical methods (SEV, TEM) and X-Ray Diffraction (XRD) analysis. In this work, it was possible to define the geometry of the aquifer, as well as its main hydrostratigraphic units, and main areas that are being affected by hydrothermal alteration. The San Juan del Río aquifer is made up of 3 main reservoirs: 1) a perched aquifer in the Sierra de Vaquerías mountain area 2) a pseudogranular unconfined aquifer in the valley with a thickness of between 100 and 200 m that overlies 3) an aquifer fractured with thicknesses between 150 and 300 m deep. The

geological/geophysical model revealed a low electromagnetic resistivity unit in the southern portion of the basin. The hydrogeochemical model allows the identification of 3 groups of groundwater, as well as the differentiation of local meteoric and hydrothermal recharge waters of a regional nature.

The stable isotopy data obtained in the meteoric waters allow the determination of a Local Meteoric Line (LMWL; $\delta^2\text{H}=7.61\delta^{18}\text{O}+5.89$) as well as three local evaporation lines at elevations of 2600, 2300 and 2000 masl ($\text{LML}_1=\delta^2\text{H}=7.61\delta^{18}\text{O}+5.89$, $\text{LML}_2\delta^2\text{H}=7.61\delta^{18}\text{O}+5.89$, $\text{LML}_3\delta^2\text{H}=7.61\delta^{18}\text{O}+5.89$ respectively). The isotopic gradient in precipitation due to the altitude effect is $\delta^2\text{H}=1.90\text{\textperthousand}$ and $\delta^{18}\text{O}=0.28\text{\textperthousand}$ for every 100 m of elevation. The isotopic composition of atmospheric water vapor ($n = 47$) averages $-79.4\text{\textperthousand}$ ($\sigma = 24.3$) for $\delta^2\text{H}$; and $-13.2\text{\textperthousand}$ ($\sigma = 3.5$) for $\delta^{18}\text{O}$. The Craig-Gordon isotopic evaporation model indicates an evaporation loss of 53% in volume, which represents an equivalent of 531 and 768 mm for the years 2016 and 2017, respectively. The isotopes of $\delta^{13}\text{C}$ and $\Delta^{14}\text{C}$ allow us to differentiate two shallow aquifers, one in the San Juan del Rio valley with a residence time of 5,400 to 9,000 years and another hanging in the Sierra de Vaquerías with groundwater residence times of 1,000 to 2,000 years.

The mixing model made from a principal component analysis (PCA) with the 3 main hydrogeochemical reservoirs identified, allows estimating the mixing percentages for groundwater in the San Juan del Rio valley. The meteoric terminal member of cold water (A; below 30°C) is characterized by a composition of Ca-Mg-HCO₃ and a hydrothermal final member is enriched in Na, K, SO₄ and Cl, with temperatures up to 90°C. The main proportion is of meteoric origin (Component A) with a percentage of between 40% and 60% of the total water. The water stored in the aquifer (Component B) with percentages between 18% and 38% represents the second most important reservoir. Finally, vertical ascending hydrothermal flow (Component C) with contributions between 2.4% and 41.6% completes the

estimate. Despite its anomalous temperature range, of the hydrothermal component (C), helium isotopic ratios show the contribution of hydrothermal fluids and their mixing with shallow waters in tectonically active regions. Which suggest that the source of He comes from the sublithospheric mantle through regional crustal fault regional flow main direction N-S.

Keywords

$\delta^2\text{H}$ - $\delta^{18}\text{O}$ - $\delta^{13}\text{C}$ stable isotopes, Craig-Gordon model, Hydrogeochemistry, Radiocarbon ages, helium isotopes, Continental extension, Geothermal energy, Semi-arid environment.

TABLA DE CONTENIDO

Declaración de ética.....	iii
Agradecimientos	iv
Resumen.....	vi
Abstract.....	ix
Tabla de Contenido.....	12
Capítulo I. Introducción general.....	14
1.1. Introducción.....	14
1.2. Objetivos.....	18
1.3. Procedimientos Analíticos.....	20
Capítulo II. Short term evaporation estimation in a natural semiarid environment: New perspective of the Craig – Gordon isotopic model.....	25
Capítulo III. Geochemical and isotopic multi-tracing ($\delta^{18}\text{O}$, $\delta^2\text{H}$, $\delta^{13}\text{C}$, $\Delta^{14}\text{C}$) of groundwater flow dynamics and mixing patterns in the volcanoclastic aquifer of the semiarid San Juan del Río Basin in Central México.....	38
Capítulo IV. Mantellic degassing of helium in an extensional active tectonic setting at front of magmatic arc (Central Mexico).....	62
Capítulo V: Conclusiones.....	76
Capítulo VI: Referencias.....	80
Capítulo VII: Anexos.....	99

- Anexo 1.** Material Suplementario del artículo: Hernández-Pérez, E., Levresse, G., Carrera-Hernández, J., & García-Martínez, R. (2020). Short term evaporation estimation in a natural semiarid environment: New perspective of the Craig – Gordon isotopic model. *Journal of Hydrology*, 587(April), 124926. <https://doi.org/10.1016/j.jhydrol.2020.124926>.....100
- Anexo 2.** Material Suplementario del artículo: Hernández-Pérez, E., Levresse G., Carrera-Hernandez, J.J., Inguaggiato, C., Vega-González, M., Corbo-Camargo, F., Carreón-Freyre D.C., Billarent-Cedillo, A., Sancén Contreras, F.J., Ramírez Hernández, C.P. (2022). Geochemical and isotopic multi-tracing ($\delta^{18}\text{O}$, $\delta^2\text{H}$, $\delta^{13}\text{C}$, $\Delta^{14}\text{C}$) of groundwater flow dynamics and mixing patterns in the volcanoclastic aquifer of the semiarid San Juan del Río Basin in Central México.....101
- Anexo 3.** Material Suplementario del artículo: Billarent-Cedillo A., Hernández-Pérez, E., Levresse G., Inguaggiato C., Ferrari, L., Inguaggiato, S., Lopez-Alvis, J., Silva-Fragoso, A. Mantellic degassing of helium in an extensional active tectonic setting at front of magmatic arc (Central México). (2022).....102

Capítulo I :

Introducción general

1.1 Introducción.

La sobreexplotación del agua subterránea en México representa un problema serio, 100 de los 188 acuíferos más importantes en el país se encuentran sobreexplotados (Cruz-Ayala & Megdal, 2020) con abatimientos en los niveles piezométrico de 2.5 m año^{-1} en algunas regiones (Carrera-Hernández et al., 2016). La mitad del territorio mexicano se constituye de ambientes áridos y semiáridos y paradójicamente estas regiones son las que concentran la mayor actividad agropecuaria, económica y de crecimiento poblacional. Actualmente las ciudades más importantes del país ya sufren de eventos recurrentes de escasez del recurso hídrico. La seguridad hídrica de la población en general está comprometida en muchas regiones, y este fenómeno parece ser amplificado por los efectos del cambio climático. Los principales impactos reconocidos que se pueden mencionar son el abasto para consumo humano, saneamiento de agua residual, contaminación emergente de corrientes y desastres por fenómenos naturales y antropogénicos, así como desastres hidrometeorológicos tales como tormentas severas, inundaciones y sequías (Arreguín-Cortés et al., 2020).

En el norte y centro de México la principal fuente de abastecimiento es el agua subterránea contenida en los acuíferos. Los acuíferos de tipo volcánico en el centro de México son sistemas hidrogeológicos complejos con limitaciones meteorológicas, climáticas, hidrográficas, geológicas y antropogénicas. Otro factor limitante es la complejidad geológica de estas cuencas que se encuentran limitadas por las estructuras regionales del tipo “Basin and Range”; formando acuíferos siliciclásticos someros que generalmente se describen como modelos geológicos compartimentados multicapa (Carrera-Hernández et al., 2016).

A pesar de que el agua subterránea es la principal fuente de agua disponible para el uso de la población en México, existe un desconocimiento de las interacciones entre los diferentes reservorios del ciclo del agua y en particular las fuentes de procedencia de los aportes al acuífero (meteórica/subterránea y local/regional). Lo que lleva a estimaciones simplistas en el balance hídrico y de recarga en los acuíferos (Cruz-Ayala & Megdal, 2020)

Es por esta complejidad que surge la necesidad de realizar una investigación hidrogeológica multidisciplinaria; que permita la integración de la información geofísica, geológica, hidrogeoquímica, de isotopía estables (C-O-H) y radiogénicos (C-He) para entender el comportamiento del sistema hidrológico de una manera integral (Alazard et al., 2015; Durand et al., 2006; Hernández-Antonio et al., 2015; Troldborg et al., 2007).

La generación de un modelo conceptual geológico-geofísico robusto es la primera etapa a desarrollar. La geometría del reservorio es fundamental para entender el flujo del agua subterránea; por lo que la comprensión de la historia geológica y sus modificaciones en escala geológica por la actividad tectónica, así como la integración con información geofísica permite definir un modelo robusto y su influencia en el almacenamiento y flujo del agua.

La caracterización geoquímica y de isótopos estables en el agua subterránea, superficial, meteórica y atmosférica es de fundamental importancia para reconocer y establecer las condiciones hidrogeoquímicas e isotópicas iniciales del agua en un sistema hidrogeológico y su evolución a través de las diversas etapas de recarga hacia un acuífero (Fritz & Fontes, 1986; Khalil et al., 2015). La principal fuente de recarga de agua subterránea es representada por la precipitación, sin embargo, es importante conocer los procesos que se están llevando a cabo en el sistema hidrogeológico y cuantificar el volumen que es afectado por la evaporación, evapotranspiración, escorrentía e infiltración para definir un balance de recarga que permita una evaluación del recurso hídrico. Los isótopos proporcionan un complemento herramienta para distinguir diferentes fuentes de agua y zonas de recarga. Los isótopos $\delta^2\text{H}$ y $\delta^{18}\text{O}$ son considerados como

trazadores ideales ya que se reparten selectivamente en cada paso del ciclo hidrológico, desde la evaporación primaria sobre los océanos su movimiento a través de la atmósfera, condensación y precipitación e infiltración hasta llegar a la recarga de las aguas subterráneas y la escorrentía de vuelta a los mares (Clark & Fritz, 1997). Los principales procesos que afectan la composición isotópica del agua a través del ciclo hidrológico son:

1. Evaporación y formación de masas de vapor atmosférico en las cuencas oceánicas y su acarreo a través de las masas de aire continentales.
2. Condensación de masas de vapor atmosférico y precipitación con variaciones en la composición en función de origen de fuente de humedad atmosférica, elevación topográfica de la precipitación, variaciones en temperatura ambiental y humedad relativa, efectos continentales por ubicación geográfica.
3. Reevaporación de aguas superficiales e infiltración del agua hacia el subsuelo, así como enriquecimiento en la fracción no evaporada del agua a través de los procesos de infiltración hacia el acuífero
4. Procesos de mezcla entre diferentes reservorios durante la recarga y el flujo del agua subterránea
5. Intercambio de isótopos durante las reacciones de interacción (disolución, solubilidad, alteración geoquímica) entre las fases líquidas-sólidas (aguaroja) y líquidas-gaseosa (agua-gases).

Este último proceso de intercambio de isótopos con minerales y gases es importante en circunstancias muy excepcionales de entornos geológicos profundos (por ejemplo, aguas geotérmicas y salmueras) o altamente aguas contaminadas (por ejemplo, vertederos), sin embargo, el contenido de isótopos en el agua subterránea retiene la firma meteórica primaria de precipitación y recarga por lo que puede ser empleado para identificar la evolución isotópica en el sistema hidrogeológico (Clark & Fritz, 1997).

Finalmente, la Cuenca del valle de San Juan del Río y sus áreas circundantes (SJR-Qro-Cel) se encuentran dentro de la intersección entre dos sistemas de fallas tectónicas regionales; los sistemas de fallas Taxco-San Miguel de Allende y Chapala-Tula. El agua subterránea presenta una recarga por fluidos hidrotermales que puede ser significativa (hasta 12%).

Este estudio se enfoca en identificar las posibles fuentes y vías de flujo para fluidos corticales y del manto sobre la aparición de diversas zonas de manantiales hidrotermales de alta y baja entalpía en la región del Bajío. Así como el entendimiento de la dinámica de flujo, el tiempo de residencia del agua subterránea en un acuífero multi compartimentado de tipo volcánico en una cuenca semiárida en el Centro de México.

1.2 Objetivos.

1.2.1 Objetivos generales.

El objetivo de este estudio doctoral es de generar un modelo conceptual integral del ciclo del agua en la cuenca de San Juan del Rio, Querétaro.

1.2.2 Objetivos particulares

Para lograr este objetivo se plantearon las siguientes acciones:

- Desarrollar y validar una metodología para recolectar vapor de agua proveniente de la humedad atmosférica para realizar análisis de isótopos de $\delta^2\text{H}$ y $\delta^{18}\text{O}$.
- Aplicar el modelo Craig and Gordon en estanques agrícolas, para evaluar el impacto de la evaporación en un entorno isotópico cerrado y semiárido.
- Comparar la tasa de evaporación isotópica mensual calculada por el modelo Craig-Gordon con el modelo físico de evaporación Penman-Monteith utilizado como validación externa.
- Establecer un modelo conceptual integrando la información geológica y geofísica de carácter científico y técnico disponibles.
- Realizar una caracterización físico-química e isotópica de las aguas atmosférica, meteórica, superficial y subterránea.
- Identificar y caracterizar las relaciones entre los diferentes reservorios de agua en el ciclo hidrológico mediante datos físicos-químicos e isotópicos.
- Caracterizar los procesos de interacción agua-roca en los diferentes reservorios de aguas subterráneas a partir de la información hidrogeoquímica e isotópica.
- Determinar los tiempos de residencia de las aguas subterráneas en los diferentes acuíferos identificados en la cuenca del Río San Juan.
- Determinar la presencia y fuente de aguas termales en los acuíferos por medio de la hidrogeoquímica, isótopos estables y gases disueltos en el agua subterránea.

- Determinar y cuantificar las proporciones de mezcla de los miembros terminales hidrogeoquímicos, así como su procedencia de los diferentes reservorios (aguas meteóricas vs aguas hidrotermales) y la dinámica de flujo en los diferentes acuíferos en la cuenca del Río San Juan.
- Identificar el papel de los sistemas de fallamiento geológico; así como las posibles intrusiones magmáticas hacia el agua subterránea en los acuíferos someros y la generación de manantiales hidrotermales de alta a baja entalpía en el límite norte del arco magmático activo (el Cinturón Volcánico Trans Mexicano, TMVB)

1.3 Procedimientos analíticos

Con el objetivo de obtener datos analíticos que permitan evaluar los objetivos propuestos, en este estudio doctoral integraran diferentes técnicas analíticas que permiten caracterizar los procesos que conforman el ciclo hidrológico en la cuenca de San Juan del Río y en el centro de México.

1.3.1 Difracción de Rayos X

Se realizó la revisión y selección de muestras de 56 pozos distribuidos en la cuenca hidrológica. Las muestras fueron molidas y secadas para su caracterización mediante Difracción de rayos X (DRX) en la Laboratorio de Fluidos Corticales del Centro de Geociencias, UNAM. La composición mineralógica fue identificada usando un difractor de polvo Miniflex de Rigaku con anticátodo de cobre CuKa ($\lambda = 1.5406\text{\AA}$), con un generador de alto voltaje (40 kV, 10 MA, 1200 W) acoplado al software SmartLab Studio. Los picos de los difractogramas fueron identificados mediante la comparación con la biblioteca de A.S.T.M (American Society for Testing and Materials). Un análisis semicuantitativo fue realizado para la mineralización total y la fracción arcillosa teniendo un error estimado de $\pm 5\%$.

1.3.2 Recolección de vapor atmosférico.

La recolección y condensación de vapor atmosférico se realizó mediante un sistema de reflujo de aire en un condensador tipo Graham. El sistema de condensación fue diseñado, elaborado y validado en el Laboratorio de Fluidos Corticales del Centro de Geociencias, UNAM. El vapor atmosférico fue colectado en una locación única (COTAS SJR) durante el periodo de junio 2016 a noviembre 2017. La elección de la ubicación responde a varios criterios que permiten asegurar

un buen rendimiento, como: una superficie horizontal con buena ventilación, sin exposición directa a la luz del sol, libre de vegetación, fauna silvestre o ganado y cuerpos de agua cercanos, alejada de cualquier fuente de calor y de aire (caliente o frío) o emisiones atmosféricas (humo, combustión, etc.).

La trampa de humedad fue de tipo “push and trap” y el ensamble del material se realizó con tubería de látex asegurando que todas las conexiones se encuentren libre de fugas. El flujo fue ajustado a 450 cc/min a régimen de flujo continuo constante. El líquido de recirculación fue etilenglicol comercial + CO_{2(s)} a -7 ± 2 °C evitando la formación de la fase sólida de agua en el interior del serpentín. Al inicio del experimento se realiza una purga del aire en el sistema antes de comenzar la condensación/colección de humedad atmosférica. El tiempo de muestreo es de 5 horas o hasta colectar 2 mL de muestra. Una vez recolectado el volumen de agua requerido se transfiere a un vial, se cierra y sella con papel parafilm y se almacena a 4°C para hasta el análisis isotópico.

1.3.3 Elementos mayores, menores y trazas en agua meteórica, superficial y subterránea.

La recolección de muestras en la cuenca de San Juan del Río incluyó agua de lluvia (n=12), bordos agrícolas (n= 3), manantiales artesianos (n=16) y agua subterránea (n=37) en la cuenca de San Juan del Río, durante los años 2016 y 2017. El agua subterránea fue recolectada directamente en la llave de toma de muestra en el pozo. La conductividad eléctrica, la temperatura y el pH fueron medidas *in situ* durante la toma de muestra usando un equipo multiparámetro Thermo-Orion Five Star Plus, una vez que las muestras fueron estabilizadas. La alcalinidad total fue determinada usando un equipo de titulación portátil HACH digital. Las muestras para análisis elemental fueron filtradas a través de una membrana de acetato de celulosa de 0.45 µm y almacenadas en botellas de HDPE fueron selladas y almacenadas a 4° hasta la realización del análisis químico. Los aniones fueron analizados mediante un HPLC – IC Dionex (LC20 con supresor ASRS ultra 300 y

detector ED50) en el Laboratorio de Geoquímica Ambiental del Centro de Geociencias, UNAM. Los metales mayores, menores y trazas fueron medidos usando un espectrómetro Thermo (iCAP 6500 Duo) en el Laboratorio de Geoquímica Ambiental del Centro de Geociencias, UNAM. La calidad de los datos fue verificada mediante el balance de cargas iónicas; en el que los análisis son rechazados en caso de que el error sea mayor a 5%.

1.3.4 Isótopos de $\delta^2\text{H}$ y $\delta^{18}\text{O}$ en aguas.

Se colectaron un total de 137 muestras para el análisis de isótopos de $\delta^2\text{H}$ y $\delta^{18}\text{O}$. Las relaciones isotópicas del vapor atmosférico ($n=47$), agua de lluvia ($n=12$) y agua superficial ($n=78$) fueron analizadas con un Analizador elemental de conversión de alta temperatura (TC/EA) acoplado a un espectrómetro de relaciones isotópicas Thermo Finnigan Delta Plus XL de flujo continuo en el Laboratorio Universitario de Geoquímica Isotópica del Instituto de Geología en la Universidad Nacional Autónoma de México. La metodología y los resultados fueron realizados, normalizados y reportados en relación al VSMOW (Coplen, 1988; Werner and Brand, 2001). Las incertidumbres analíticas del $\delta^{18}\text{O}$ and $\delta^2\text{H}$ fueron calculadas en el 0.12‰ and 1.2‰, respectivamente

1.3.5 Isótopos $\delta^{13}\text{C}$ y $\Delta^{14}\text{C}$ en aguas subterráneas.

Para realizar los fechamientos e identificar los procesos del carbono en la cuenca de San Juan del Rio se seleccionó un grupo de veinte muestras a partir de las muestras colectadas de agua subterránea, las cuales fueron analizadas para medir la relación isotópica de $\delta^{13}\text{C}$ y la actividad del $\Delta^{14}\text{C}$. Estos análisis isotópicos se realizaron en los laboratorios de Beta Analytics en Miami, USA. La medición de la actividad del $\Delta^{14}\text{C}$ es realizada mediante Espectrometría de Masas con Acelerador (AMS). El análisis se realiza en grafito producido por la reducción de una muestra de CO_2 sobre un catalizador de Cobalto. El CO_2 se obtiene de la combustión de la muestra a más de 800° en una atmósfera con 100% de oxígeno. El CO_2 se seca primero con metanol/hielo seco y se colecta en nitrógeno líquido para su

subsecuente reacción de grafitización. El resultado analítico (“BP” o “pMC”) se obtiene al medir la razón $^{14}\text{C}/^{13}\text{C}$ de la muestra relativo al $^{14}\text{C}/^{13}\text{C}$ en ácido oxálico II (NIST-4990C) usando un acelerador de partículas en conjunto con un Thermo Fisher GasBench 2.0. El headspace muestrado por aguja de doble vía a usando un flujo de He como fase móvil para acarreo de $\text{CO}_2 + \text{He}$ hacia el GasBench donde es separado de cualquier otro gas remanente a través de una columna de Cromatografía de Gases. La detección de CO_2 fue mediante GC con un control ISODAT. La corrección de la deriva fue aplicada mediante la normalización con los estándares internos a los valores esperados.

1.3.6 Gases nobles e isótopos de ^3He , ^4He y ^{20}Ne en aguas subterráneas

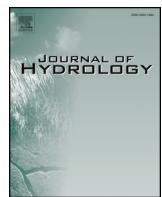
Se recolectaron seis muestras de agua subterránea en pozos con profundidades de 25 a 300 m en las cuencas de Querétaro y San Juan del Río, así como una muestra de gas proveniente de un pozo geotérmico en el campo geotérmico de Celaya. La colecta se realizó en botellas de vidrio de 121 ml, siendo llenadas y selladas bajo el agua con septos de goma para evitar la contaminación por gases atmosféricos durante el procedimiento de toma de muestra. Una vez colectada la muestra las botellas se sumergieron en agua para evitar contaminación por gases atmosféricos durante el almacenamiento. Una muestra de la fase gaseosa se colectó en la boca del pozo geotérmico en la ciudad de Celaya.

La determinación de la composición química de gases y el análisis isotópico de gases nobles se realizaron en el Laboratorio de Geoquímica del Istituto Nazionale di Geofisica e Vulcanologia – Palermo (INGV-Pa). La composición química de los gases disueltos se analizó mediante un cromatógrafo de gases Agilent 7890 utilizando Ar como gas portador. El cromatógrafo de gases está equipado un detector de conductividad térmica (TCD) para el análisis de He, H₂,

O₂, N₂ y un detector de llama (FID) para el análisis de CO, CO₂ y CH₄ (Capasso e Inguaggiato, 1998). El error analítico fue inferior al 5%. Los gases nobles se purificaron a partir de la mezcla de gases a través de una línea de ultra alto vacío de acero inoxidable en el que fueron separados criogénicamente e injectados en un espectrómetro de masas de gases nobles de tubo dividido (GVI® Helix SFT) para los isótopos de He y en un espectrómetro de masas multicolector de gases nobles (Thermo® Helix MC) para los isótopos de Ne. El Ar fue analizado mediante un espectrómetro de masas multicolector (GVI® Helix MC) según lo descrito por Rizzo et al., (2015). Se midieron las concentraciones isotópicas de ³He, ⁴He y ²⁰Ne para calcular las relaciones ³He/⁴He y ⁴He/²⁰Ne. El método para la extracción de gas y los análisis isotópicos se describen en detalle en Inguaggiato y Rizzo (2004). El error analítico es inferior al 3% en una determinación de una sola masa

Capítulo II :

Short term evaporation estimation in a natural semiarid environment: New perspective of the Craig – Gordon isotopic model.



Research papers

Short term evaporation estimation in a natural semiarid environment: New perspective of the Craig – Gordon isotopic model

Eliseo Hernández-Pérez^a, Gilles Levresse^{b,*}, Jaime Carrera-Hernández^b, Rocio García-Martínez^c^a Posgrado en Ciencias de la Tierra, Campus, Juriquilla, Universidad Nacional Autónoma de México, 3001 Querétaro 76000, Mexico^b Centro de Geociencias, Campus, Juriquilla, Universidad Nacional Autónoma de México, Mexico^c Instituto de Estudios Ambientales, Ciudad de México, Universidad Nacional Autónoma de México, Mexico

ARTICLE INFO

This manuscript was handled by Huaming Guo, Editor-in-Chief, with the assistance of Philippe Negrel, Associate Editor

Keywords:
 $\delta^2\text{H}$ - $\delta^{18}\text{O}$ stable isotopes
 Evaporation
 Craig-gordon model
 Penman-monteith equation
 Semi-arid areas

ABSTRACT

Evaporation is one of the most important processes in the hydrologic cycle and is considered as one of the lead factors governing climate in terrestrial environments, particularly in arid areas. In natural open systems, evaporation should be considered as a time dependent function and a cumulative process. We applied and compared Craig-Gordon isotopic model with the Penman-Monteith physical evaporation model, after a biannual hydrologic cycle characterization in a natural semi-arid environment to determine annually reliable balance budgets and estimations. Our results show that isotopic evaporation rates reflect a sinusoidal behavior during isotopic fractioning rather than a linear and constant evaporation rate. This sinusoidal behavior exhibits the influence of solar radiation and other meteorological variables that have not yet been considered in the C-G isotopic mass balance model. The estimation of isotopic evaporation in natural environments are reliable during the dry season while estimations of isotopic loss fraction (f) in the wet season behave as an isotopic mixing model of evaporated water-precipitation-runoff. Physical and isotopic methodologies are difficult to relate due to basic fundamentals and development conceptualizations: accordingly, further work is required to enhance the Craig-Gordon and Gonfiantini evaporation model and its relationship with physical methodologies in order to improve the estimation of evaporation in natural semiarid environments.

1. Introduction

The evolution of $\delta^2\text{H}$ - $\delta^{18}\text{O}$ isotopic ratios throughout the water cycle are widely used to identify water sources, recharge zones, and hydrological processes caused by water mixing, water/rock interaction and evaporation, thus providing insight into the dynamics of groundwater flow (Fritz and Fontes, 1986; Gat, 2002, 1996; Gat and Levy, 1978; Gibson, 2002; Gibson and Bursey, 1993; Gonfiantini, 1986; Issar et al., 1984; Tsujimura et al., 2007; Verma et al., 2000). The characterization of isotopic composition in each isotopic reservoir, namely atmospheric vapor – precipitation – runoff – groundwater, is essential to properly identify isotopic evolution and fractioning processes involved in each step of the hydrological cycle. Evaporation is one of the most important processes in the atmospheric part of the hydrological cycle; in fact it is considered as one of the lead factors governing climate in terrestrial environments (Gonfiantini et al., 2018), being also the most difficult parameter to estimate (Gat et al., 1994, 2005).

Physical estimations of evaporation are generally classified according to the way in which it is determined: pan coefficient,

temperature and radiation, mass-transfer energy budget, and combination methods (Alazard et al., 2015; Ali et al., 2008; Majidi et al., 2015). Several evaporation estimation methodologies have been compared concluding that the Penman-Monteith method is the most robust and reliable physical method (Alazard et al., 2015; Ali et al., 2008; Majidi et al., 2015).

In contrast to the different available approaches to estimate physical evaporation, the chemical methodologies are limited to the Craig-Gordon and Gonfiantini (C-G) isotopic evaporation model. The C-G isotopic model is based on air vapor and liquid phase isotopic relationship in an open or closed isotopic system. This model was successively improved by Fontes and Gonfiantini (1967) and Zimmerman (1979) as an isotopic mass balance method which uses enrichment in isotopic composition to estimate the short-term evaporated fraction (f) in lakes and hydrological basins (Fellman et al., 2011; Gat et al., 1994; Gibson, 2002; Gibson et al., 2008, 2016; Skrzypek et al., 2015). The Craig and Gordon (1965) and Gonfiantini (1986) isotopic evaporation model is the most accepted chemical method and has recently been unified into a unique model that considers several environmental

* Corresponding author.

E-mail address: glevresse@geociencias.unam.mx (G. Levresse).

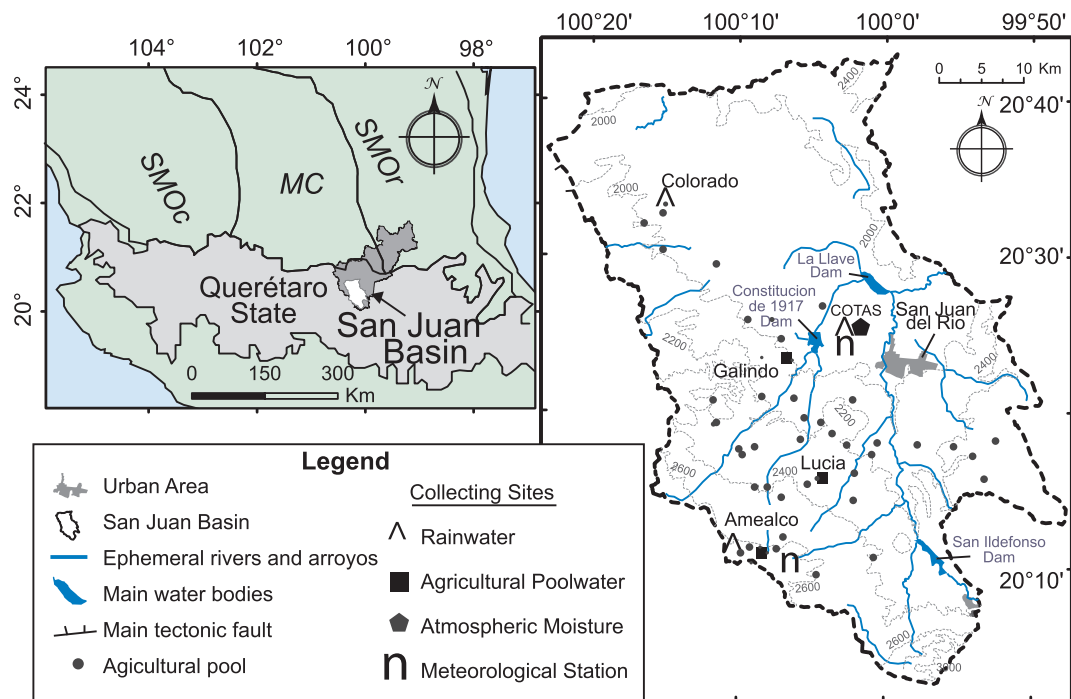


Fig. 1. Location of San Juan Basin in Central México. Location of rainwater, agricultural poolwater, meteorological stations and atmospheric moisture collecting sites.

variables such as initial water composition, atmospheric relative humidity, environmental temperature, atmospheric water vapor composition and water salinity fitting into almost all evaporation experiments (Gonfiantini et al., 2018). Despite these known limitations, lakes, ponds and other natural water bodies usually have enough water mass to ensure that isotopic averaging occurs while smoothing the impact of short-term variations in the environmental variables. In these cases the use of longer-term average air temperature or relative humidity values may be feasible with some precautions (Gonfiantini et al., 2018).

In this work we present, discuss and improve the acquisition and reliability of both physical and chemical data required to apply the C-G model in agricultural pools located in a closed isotopic and semiarid environment. Finally, we compare the monthly isotopic evaporation rate with the commonly used physical Penman-Monteith evaporation model as an external validation.

2. Theory

The evaporative loss fraction (f) of surface water is calculated following the model of Craig–Gordon (Craig and Gordon, 1965), modified by Gonfiantini (1986), (Gat et al., 1994), Gibson and Reid (2010), and Gonfiantini et al. (2018) using non-steady-state conditions, as described by Fellman et al. (2011).

$$f = 1 - \left[\frac{(\delta_L - \delta^*)}{(\delta_p - \delta^*)} \right]^{(1/m)} \left[\frac{(\delta_L - \delta^*)}{(\delta_p - \delta^*)} \right]^{(1/m)} \quad (1)$$

where f is the evaporated fraction, δ_p is the isotopic composition of rainwater ($\delta^2\text{H}$, $\delta^{18}\text{O}$), δ_L is the isotopic composition of pool water, m is the equation that relates the isotopic composition of air vapor removed by evaporation and the isotopic composition of the liquid (Gibson, 2002; Welhan and Fritz, 1977), while δ^* is the composition where no fractioning occurs—this term is also known as the local limiting isotopic composition.

$$\delta^* = \frac{h\delta_A + \varepsilon}{(h - \varepsilon/1000)} \quad (2)$$

The δ^* value was determined under local meteorological conditions,

following the procedure described in Gat and Levy (1978) and Gat (1981), where h is the relative humidity, the temperature recorded at meteorological stations in the basin, ε is the total isotopic fractioning, and δ_A is obtained from direct measurements of atmospheric moisture.

The parameter m is obtained by the equation (Gibson, 2002):

$$m = \frac{\frac{(h - \varepsilon)}{1000}}{\frac{(1 - h + \varepsilon_k)}{1000}} \quad (3)$$

where ε_k is the kinetic isotope fractionating factor calculated by:

$$\varepsilon_k = (1 - h)C_k \quad (4)$$

where C_k is the kinetic fractioning constant 14.2‰ for $\delta^{18}\text{O}$ and 12.5‰ for $\delta^2\text{H}$ (Araguás-Araguás et al., 2000; Gonfiantini, 1986). The total isotope fractioning ε (‰) was calculated using the following equation:

$$\varepsilon = \varepsilon^* + \varepsilon_k \quad (5)$$

where ε^* is the equilibrium isotope fractioning factor (Horita and Wesolowski, 1994).

To solve the Craig and Gordon (1965) and Gonfiantini, (1986) evaporation models, both physical and isotopic measurements are needed. Temperature and relative humidity data were obtained from an automatic meteorological station while the long-term average atmospheric moisture (δ_A) was obtained by isotopic characterization of sampled atmospheric water vapor. The total isotopic fractioning factor ($\varepsilon = 9.3982\%$) was obtained by the validation procedure of the water vapor condensation-sampling collector. The acquisition and validation of the data used is given in the methodology section.

3. Study area

The San Juan del Rio Basin lies in the southeastern corner of the Mesa Central geological province (Fig. 1). Regionally, the San Juan del Rio Basin is surrounded by the Trans-Mexican Volcanic Belt (TMVB) in the south and Sierra Madre Oriental (SMOR) on the east (Fig. 1). Locally, it is an intermountain exorheic basin in Querétaro State, with an extension of 2,800 km² and an altitude that varies from 1900 to 3200 m above sea level (m a.s.l.). The San Juan del Rio Basin (SJR) is a

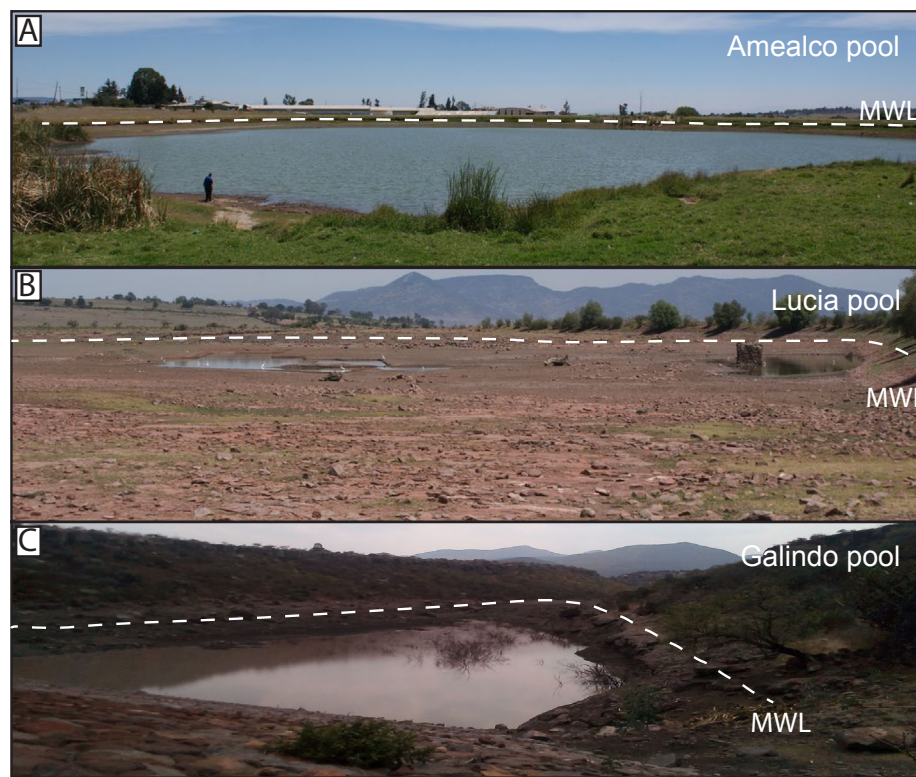


Fig. 2. Panorama view of the agricultural pools near the localities of A) Amealco (2600 masl), B) Lucia (2300 masl) and C) Galindo (2000 masl, see Fig. 1). Pictures were taken at the end of dry season (may of 2017) when the water level reaches its minimum. White dashed line indicates the maximum water flooding (September of 2017).

semiarid area that receives humid air masses from both the Atlantic and Pacific oceans during a short rainy season period (Carrera-Hernández et al., 2016; Luna-Niño and Cavazos, 2018; Van Der Ent et al., 2010). The San Juan del Rio Basin is part of the upper watershed of the Pánuco Basin which drains into the Gulf of Mexico. The SJRB has a dendritic drainage network formed by numerous ephemeral arroyos that flow mainly during the rainy season. The two main water bodies in the study area are San Ildefonso and Constitución de 1917 with an estimated storage volume of $\sim 75 \text{ Mm}^3$. To sustain seasonal agriculture in this region, numerous pools were built in the basin (Fig. 1), which have small volumes ($< 0.1 \text{ Mm}^3$) and are characterized by wide water areas with shallow water depths ($< 5 \text{ m}$; Figs. 1 and 2).

4. Materials and methods

4.1. Atmospheric vapor, rainwater and pool water sampling.

Atmospheric water vapor samples (δ_{A}) were collected at the Comité Técnico de Aguas Subterráneas (COTAS) facility near San Juan del Rio (Fig. 1) from June 2016 to November 2017. To collect the vapor samples, we used the push and trap method to condense and collect moisture with a flow of 4 l min^{-1} into a kitazato flask connected to a Graham condenser. We used a 50% mixture of ethylene glycol + water + $\text{CO}_{2(\text{s})}$ as refrigerant liquid with a temperature selected of $-7^\circ\text{C} \pm 1^\circ\text{C}$ to avoid freezing and further isotope fractioning due to vapor-liquid-solid phase changes of the collected sample. It took 6 h to obtain a volume of 5 mL of each sample needed for analysis. Once the sample was condensed, it was transferred to a test tube, perfectly sealed, and sent to the Laboratorio Universitario de Geoquímica Isotópica (LUGIS) of the Universidad Nacional Autónoma de México for analysis.

Rainwater samples were collected in three different sites located throughout the San Juan del Rio Basin (Fig. 1), during the wet season of 2017. The rainwater collector design is comparable to that described by Calva-Hernández (2011) and to prevent evaporation, we added 1 cm of low-density oil into the collector.

Agricultural pool water was sampled during a three-year period from May 2015 to October 2017 and the collecting sites ($n = 3$) were chosen to be agricultural perennial pools with a similar volume. These sites are located near the towns of Amealco (2600 m.a.s.l.), Lucia (2300 m.a.s.l.), and Galindo (2000 m.a.s.l.; Figs. 1 and 2). After the water was collected it was filtered with a $0.45 \mu\text{m}$ Millipore membrane filter and stored in a 125 mL Nalgene HDPE bottle sealed with parafilm and preserved at 4°C to prevent evaporation before its analysis.

4.2. Meteorological data

The meteorological data for this study were obtained from two automatic weather stations (Vantage Pro 2 from Davis Instruments, administrated by Queretaro's Water State Commission) located in the Amealco and Pedro Escobedo municipalities (Fig. 1). These stations record meteorological data every 10 min, and the data between October 2015 and September 2017 were used in this work.

4.3. Stable isotope analysis

Isotopic ratios of $\delta^{2\text{H}}$ and $\delta^{18\text{O}}$ were analyzed with a High Temperature Conversion Elemental Analyzer (TC/EA) coupled to a Thermo Finnigan Delta Plus XL continuous flow isotope ratio spectrometer at the laboratory Laboratorio Universitario de Geoquímica Isotópica of the Instituto de Geología, Universidad Nacional Autónoma de México. Methodology and results were conducted and normalized and reported relative to VSMOW (Coplen, 1988; Werner and Brand, 2001). The $\delta^{18\text{O}}$ and $\delta^{2\text{H}}$ analytical uncertainties are calculated as 0.12‰ and 1.2‰, respectively.

5. Results

5.1. Local meteorology

Annual relative air humidity ranges from 14% to 100%, although it is usually larger than 40% during the wet season (Fig. 3A, Table AE-1).

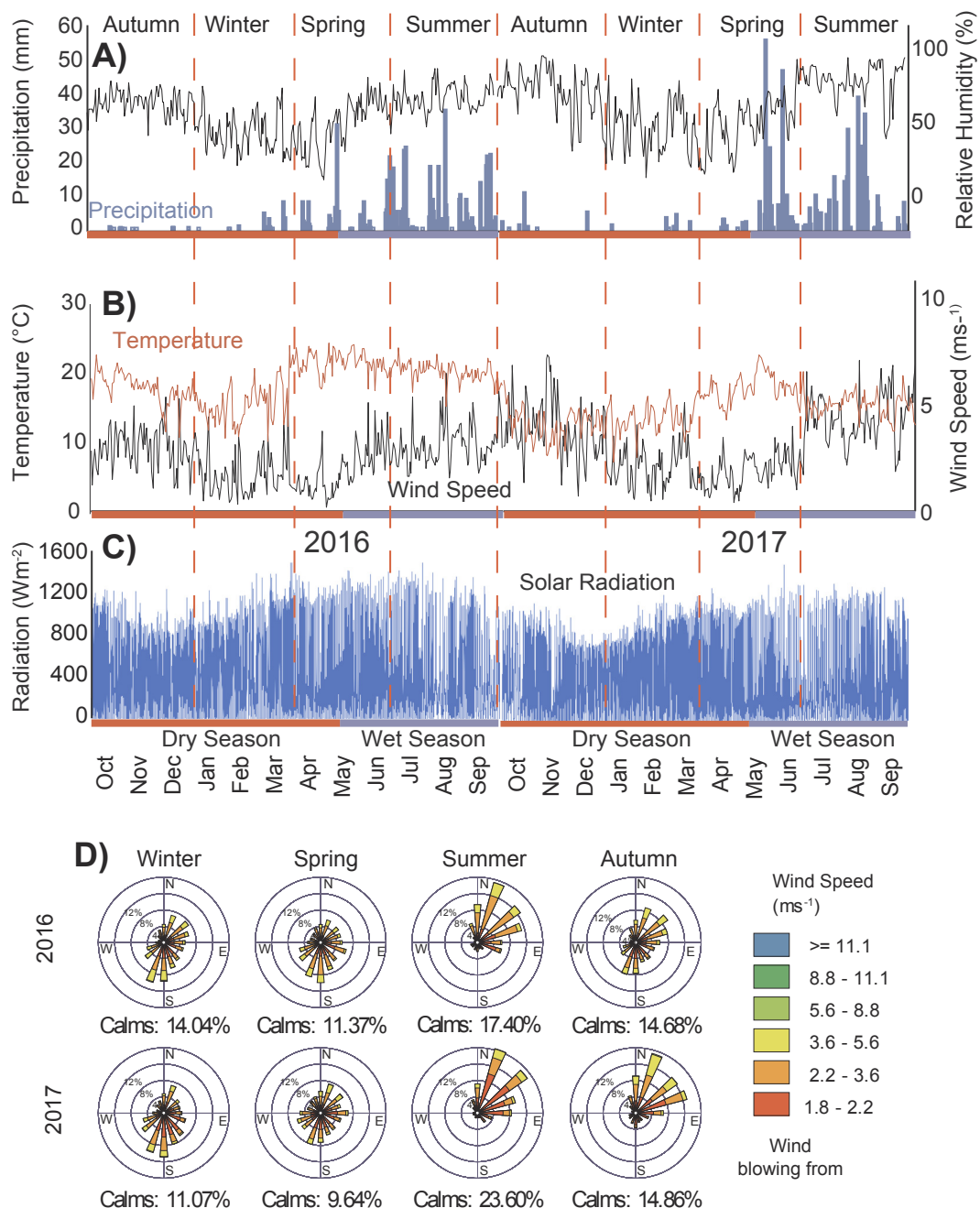


Fig. 3. A) Daily averaged relative humidity (%) and accumulated precipitation (mm) during 2016 and 2017; B) Daily averaged values for temperature ($^{\circ}\text{C}$), and wind speed (ms^{-1}) C) daily solar radiation (Wm^{-2}) and D) Wind Rose plots for 2016 and 2017 years. Data were collected from Vantage Pro II meteorological station in Amealco city. Calms (less than 1 knot or 0.5 ms^{-1}).

The annual air temperature ranges from $0.9 ^{\circ}\text{C}$ to $33.9 ^{\circ}\text{C}$, with an annual average of $17 ^{\circ}\text{C}$. The daily mean air temperature data display a sinusoidal behavior with maximum daily mean temperatures from March to September, and lowest daily mean temperatures than annual average from October to February (Fig. 3B). The solar radiation shows a long-term sinusoidal behavior (Fig. 3C). The crests (highs) of the sinusoidal curve correspond to the summer solstice with maximum daily solar radiation of 1376 Wm^{-2} in August 2016 and 1494 Wm^{-2} in June 2017. Minimum daily solar radiation intensities correspond to the winter solstice where maximum radiation intensity reaches 1085 and 854 Wm^{-2} for February and December 2016. The annual accumulated precipitation in the SJRB was 612 mm in 2016 and 540 mm in 2017. Precipitation during the wet season (June–September) accounts for 80% of the total annual rainfall volume (420 and 435 mm in 2016 and

2017, respectively). In this region, the intensity of precipitation can reach even 10% of the total annual value in a few hours – as observed in May 28th, 2017. The wind speed registered in the study area ranges from 0.31 ms^{-1} to 7.56 ms^{-1} with a frequency of calms from 9.64% to 23.6% (Fig. 3D). Winds are classified from 0 to 3 or light to moderate breeze in the Beaufort scale (Lindau, 1995). Wind speed and its direction in a rose plot reflects different conditions between winter-spring and summer-autumn season (Fig. 3D). The atmospheric conditions in summer-autumn season are stable with dominant calm periods (17.4% and 23.6% for 2016 and 2017, respectively) and northeast dominant winds blowing between 2.1 and 5.7 ms^{-1} (27% of the data points). In contrast during winter-spring season, dominant winds (25%) blow gently from the south (under 3.6 ms^{-1} ; 16% of the data points).

5.2. Evaporation estimates based on penman–monteith method for open water.

To estimate the coherence of the isotopic evaporative loss fraction (f) we determined the physical evaporation rates through the Penman–Monteith (1981) standard equation for water bodies, that combines an aerodynamic and a radiative component (Cai et al., 2007):

$$E_0 = \frac{\frac{R_n}{l} + \frac{\gamma E_a}{\Delta}}{1 + \frac{\gamma}{\Delta}} \quad (6)$$

where E_a is evaporation calculated according to Dalton-Rohwer equation (Eq. (7)), R_n is net radiation ($\text{MJ m}^{-2} \text{d}^{-1}$), l is latent heat of evaporation ($l = 2.45 \text{ MJ kg}^{-1}$), Δ the slope of the curve of saturation vapour pressure as a function of temperature ($\text{kPa}^\circ\text{C}^{-1}$), and γ is the psychrometric constant.

The Rowher (1931) approach assumes that evaporation is a function of wind speed and of the difference between the vapour pressure of the water surface and the atmosphere. It uses an empirical mass transfer coefficient to explain the relation between the different parameters through the wind function.

$$E_0 = 0.4(e_s - e_a)(1 + 0.17u_2) \quad (7)$$

where u_2 is the wind velocity measured at a height of 2 m (ms^{-1}), e_s is the pressure of saturated water vapour at the temperature of the water surface (mbar) and e_a is the water vapour pressure above the evaporating surface (mbar) as a function of relative humidity (RH), and air temperature (T_{air}). We used the term (μu_2) as a linear wind function where μ is the Dalton empirical constant estimated for each study site multiplied by u_2 . As has been done previously by other authors (Ali et al., 2008; Alazard et al., 2015). The empirical constant μ was computed using its relationship with water surface area proposed by Harbeck (1962). We used wind, atmospheric pressure, relative humidity and air temperature data from the Amealco municipality.

In Fig. 4 we present the time series evaporation estimates and accumulated evaporation based on Amealco station (Fig. 1) meteorological data, calculated with Dalton-Rohwer and Penman-Monteith equations (Fig. 4A). Both equations give a very similar daily and monthly evaporation estimates and accumulation patterns (Fig. 4A, B). The Penman-Monteith equation generally reaches larger evaporation values than the Dalton's method as it integrates aerodynamic and radiative components that have not been considered in Dalton's method. With the Penman-Monteith equation, the daily evaporated volumes range from 0.13 to 5.39 mm day^{-1} , with the bulk of the data distribution average of 1.8 ($\sigma = 0.6$) mm day^{-1} (Table EA6). The larger evaporation rates are observed during the hot and dry days, while the lower evaporation rates correspond to the raining and winter periods.

To represent a comparable mass balance process, both physic and isotopic data sets are present on a monthly basis (Fig. 4B) and precipitation is integrated in the Penman-Monteith equation. The data evolution in the diagram not only represents the monthly evaporation rate and accumulation but a hydrologic mass balance between evaporation and precipitation (Fig. 4B). In this case, if the mass-balance and evaporation patterns are comparable during the dry season, the amplitude of the sinusoidal function increases during the wet season as is dominated by precipitation volumes (Fig. 4B). As previously shown, the Penman-Monteith evaporation estimations are larger than those calculated by the Dalton-Rohwer equation.

The wet to dry season transition is highlighted in the annual evaporation accumulation curve by a changing slope point (Fig. 4C). The annual evaporation accumulation in Amealco municipality reaches 531.0 mm in 2016 and 768.6 mm in 2017 (Table EA6 and Fig. 4B) which is comparable to the annual precipitation accumulation normal in the region (1971–2000, 565 mm; Carrera-Hernandez et al., 2016). In the San Juan Basin (Fig. 1), the Amealco area hydrological balance, is almost at equilibrium along the analyzed period (2016–2017), with a

low precipitation excess (81.2 mm) in 2016 and some precipitation deficit (226.1 mm) in 2017 (Fig. 4C).

5.3. Isotopic rainwater composition ($\delta^2\text{H}-\delta^{18}\text{O}$)

The San Juan del Rio Basin is the upper watershed of the Pánuco Basin and rainwater is the only water input in the local hydrologic cycle, thus making this basin suitable to estimate evaporation. As a first step we setup the Local Meteoric Water Line (LMWL) as it is required to determine the initial isotopic composition of the water input and illustrates its evolution throughout the hydrological cycle.

Twelve samples were collected monthly during the 2017 raining period (06/2017–09/2017) at three different locations and elevations: (1) Amealco (2620 m.a.s.l.), (2) COTAS facility near San Juan del Rio city (1920 m.a.s.l.), and (3) Colorado (1925 m.a.s.l.; Fig. 1). The $\delta^2\text{H}-\delta^{18}\text{O}$ rainwater results are presented in Table EA2 and Fig. 5, where it can be seen that the variation of $\delta^2\text{H}$ through the period shows a high dispersion varying from -108.8‰ to 12.9‰ with a mean value of -66.0‰ ($\sigma = 31.6$). In contrast, $\delta^{18}\text{O}$ presents a lower dispersion ranging from 15.1‰ to 0.9‰ and a mean value of -9.5‰ ($\sigma = 0.1$). The lighter isotopic rainwater samples were collected from the Amealco sites after intense precipitation events (Table EA2).

To improve the Local Meteoric Water Line, we added regional historical data to our dataset ($n = 16$; Cortés et al., 2000, and this study). Both collected and historical data display a unique linear dispersion, to which the following linear relationship was adjusted $\delta^2\text{H} = 7.61 \delta^{18}\text{O} + 5.89$ ($r^2 = 0.9927$; Fig. 5; Table EA2). The slope and intercept of the Local Meteoric Water Line in the San Juan Del Rio Basin are slightly lower than those defined for nearby basins $\delta^2\text{H} = 8.18 \delta^{18}\text{O} + 12.8$ in the San Luis Potosi State (Calva-Hernández, 2011) and $\delta^2\text{H} = 7.95 \delta^{18}\text{O} + 11.7$, Sierra de las Cruces in Mexico (Cortés-Silva and Farvolden, 1989). These isotopic variations reflect differences in meteorological conditions, greater aridity and precipitation effect as humid air masses travel inland.

5.4. Atmospheric water vapor isotope composition ($\delta^2\text{H}-\delta^{18}\text{O}$)

The isotopic composition of atmospheric water vapor ($n = 47$, Table EA3) was collected in a unique location (COTAS facilities; Fig. 1) from June 2016 to November 2017. During this period, the isotopic vapor composition varies from -157.7‰ to -25.7‰ with a mean value of -79.4‰ ($\sigma = 24.3$) for $\delta^2\text{H}$; and from -22.0‰ to -2.0‰ with a mean value of -13.2‰ ($\sigma = 3.5$) for $\delta^{18}\text{O}$.

The time series of the $\delta^2\text{H}$ and $\delta^{18}\text{O}$ ratios show that isotopic composition are sensitive to air temperature and the seasonal variation of humidity (Fig. 6). The variation of $\delta^2\text{H}-\delta^{18}\text{O}$ composition is larger during wet ($\sigma_{\delta^2\text{H}} = 29.4$; $\sigma_{\delta^{18}\text{O}} = 4.2$) than dry ($\sigma_{\delta^2\text{H}} = 15.6$; $\sigma_{\delta^{18}\text{O}} = 2.7$) seasons.

The beginning of the wet season is highlighted by progressively decreases in the isotopic atmospheric vapor composition $\delta^2\text{H}$ and $\delta^{18}\text{O}$ ratios that is correlated with the intensification of precipitation (Fig. 6).

When the meteorological conditions during wet season are well established, the $\delta^2\text{H}$ and $\delta^{18}\text{O}$ isotopic atmospheric vapor ratios fluctuate as a result of the presence and intensity of rainfall events.

5.5. Composition of $\delta^2\text{H}-\delta^{18}\text{O}$ in pool water

The isotopic composition of pool water ($n = 78$) was defined monthly in three different locations: Amealco (2600 m.a.s.l.), Lucia (2300 m.a.s.l.) and Galindo (2000 m.a.s.l.) sites from May 2015 to October 2017.

Isotopic ratios of pool water in the Lucia pool range from -82.6‰ to 17.3‰ for $\delta^2\text{H}$ and -11.5‰ to 6.0‰ for $\delta^{18}\text{O}$, while ratios in the Galindo pool display variations from -88.4‰ to 13.1‰ for $\delta^2\text{H}$ and -12.3‰ to 6.5‰ for $\delta^{18}\text{O}$ (Fig. 7). Finally, the isotopic ratios of pool water in the Amealco site range from -57.0‰ to -13.0‰ for $\delta^2\text{H}$ and

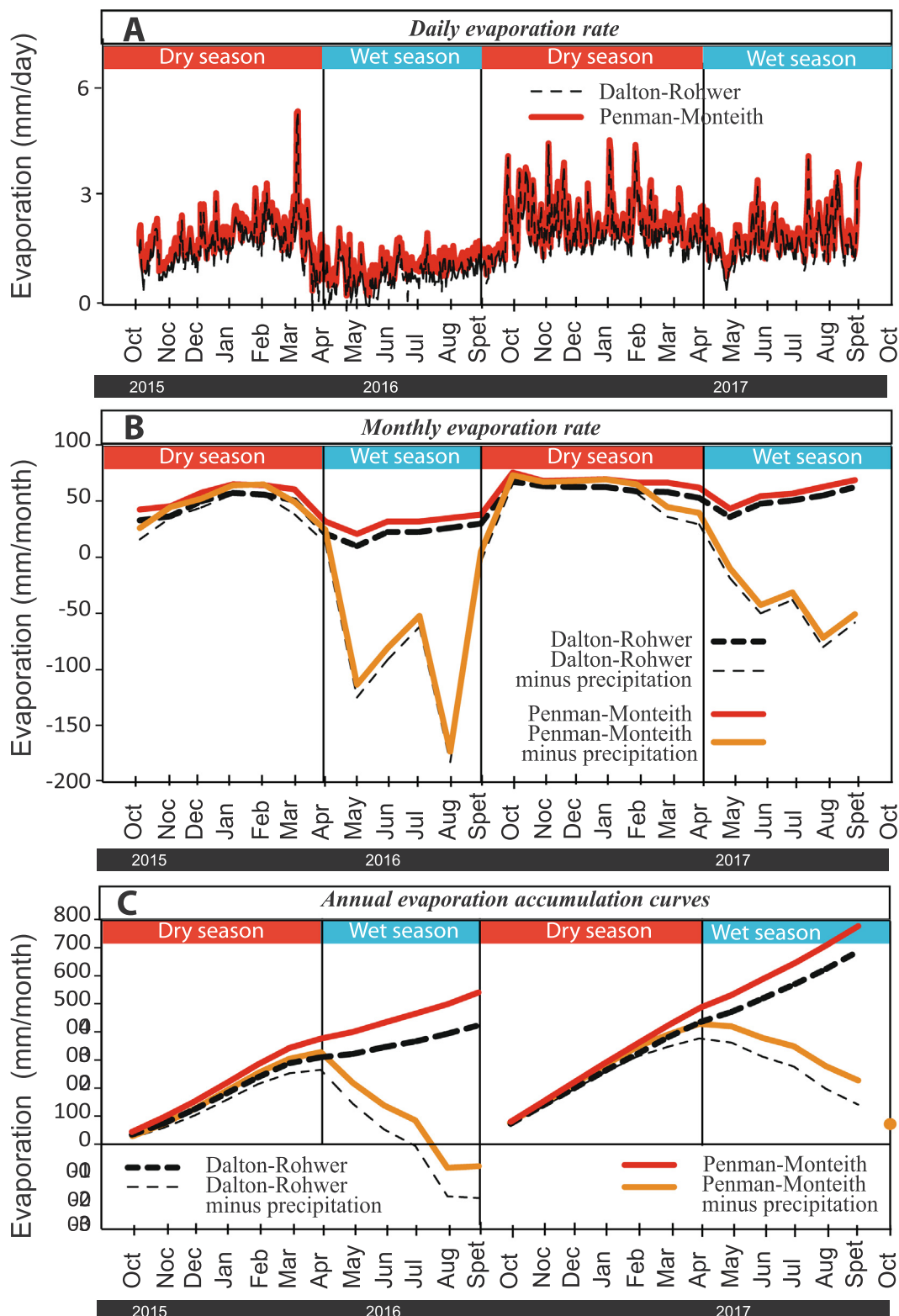


Fig. 4. Time series of physical evaporation in Amealco municipality. (A) Monthly physical evaporation estimates from Penman-Monteith and Dalton-Rohwer equations and monthly hydrologic balance (evaporation estimate less precipitation); (B) Monthly physical evaporation accumulated from Penman-Monteith and Dalton-Rohwer equations and monthly hydrologic balance (accumulated evaporation less precipitation).

-7.6‰ to -0.6‰ for $\delta^{18}\text{O}$, displaying less variability in the isotopic composition of pool water relative to Lucia (2300 m.a.s.l.) and Galindo (2000 m.a.s.l.) sites.

Over time, all pools present a comparable sinusoidal isotopic evolution pattern (Fig. 7) and a progressive heavy isotope enrichment of

pool water is observed during the dry season from September to May/June illustrating the evaporation process. The changes in the evaporation pattern caused by the inputs of precipitation and runoff into the pools are highlighted by a rapid fall of the $\delta^2\text{H}-\delta^{18}\text{O}$ isotopic ratio values during May/June to July. The depletion in the isotopic ratios can

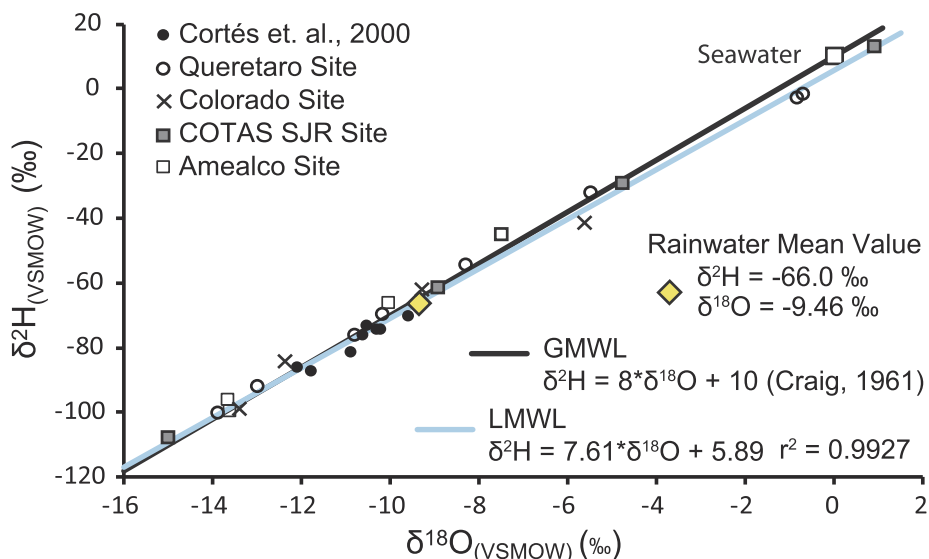


Fig. 5. New isotopic data of local precipitations and Local Meteoric Water Line (LMWL) for San Juan Basin in Central Mexico.

be up to 100‰ in $\delta^2\text{H}$ and 18‰ in $\delta^{18}\text{O}$. Such large depletion in the isotopic values illustrate the mixing process between the small amount of water from which evaporation has already occurred and the large volumes of rainwater rapidly added in the pools.

The pool water isotopic compositions for the Amealco, Galindo and Lucía pools are compared to GMWL and the previously defined LMWL (this study) in Fig. 8. The isotopic composition of pool water in the three sites present a common distribution along a local evaporation water line (LEL). Such distribution confirms that the only input to the shallow pools is the local precipitation and runoff rather than groundwater (Fellman et al., 2011). Furthermore, it is possible to distinguish a proper regression line for each sampled pool (Fig. 8). The equations for the Amealco pool (LEL_1), Lucía pool (LEL_2), and Galindo pool (LEL_3) are $\delta^2\text{H} = 5.91 \times \delta^{18}\text{O} - 11.08$ ($r^2 = 0.9648$), $\delta^2\text{H} = 5.73 \times \delta^{18}\text{O} - 14.96$ ($r^2 = 0.9796$), and $\delta^2\text{H} = 5.38 \times \delta^{18}\text{O} - 19.84$ ($r^2 = 0.9839$)

respectively, which show a slight decrease with altitude (Fig. 8). Such variations are usually attributed to temperature, relative humidity and the altitude gradient within the basin (Gonfiantini, 1986). The intersections of the LELs with the LMWL are considered representative of the initial $\delta^2\text{H}$ and $\delta^{18}\text{O}$ isotopic composition of pool water prior to evaporation. These intersections also represent the local mean $\delta^2\text{H}$ - $\delta^{18}\text{O}$ isotopic composition of rainwater, only if the pool reaches a complete desiccation during the dry season and is not connected to groundwater. The LELs – LMWL intersections values are in Amealco (2600 m.a.s.l.), $\delta^2\text{H} = -70.1\text{\textperthousand}$, $\delta^{18}\text{O} = -10.0\text{\textperthousand}$, in Lucía (2300 m.a.s.l.), $\delta^2\text{H} = -76.6\text{\textperthousand}$, $\delta^{18}\text{O} = -11.1\text{\textperthousand}$ and in Galindo (2000 m.a.s.l.) $\delta^2\text{H} = -81.4\text{\textperthousand}$, $\delta^{18}\text{O} = -11.6\text{\textperthousand}$. The differences in the compositions at the intersections were used to calculate the isotopic elevation gradients which are estimated to be 1.90‰ for $\delta^2\text{H}$ and 0.28‰ in $\delta^{18}\text{O}$ per 100 m. These values are within those published for mountainous

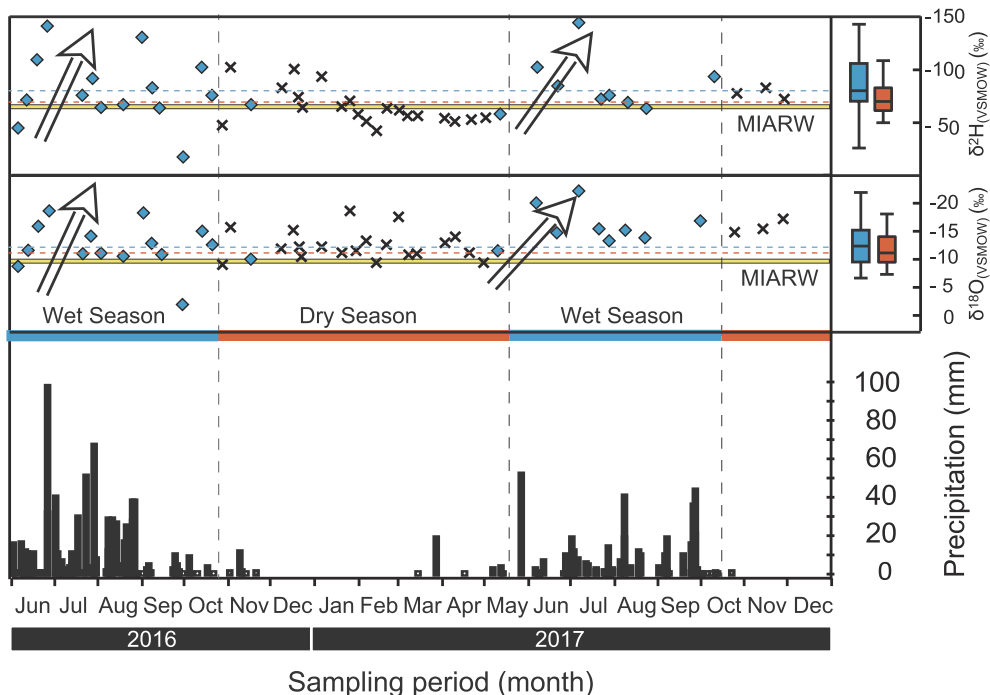


Fig. 6. Time series of $\delta^2\text{H}$ and $\delta^{18}\text{O}$ atmospheric vapor values, compared with precipitation intensity. MIARW: mean isotopic annual rainwater.

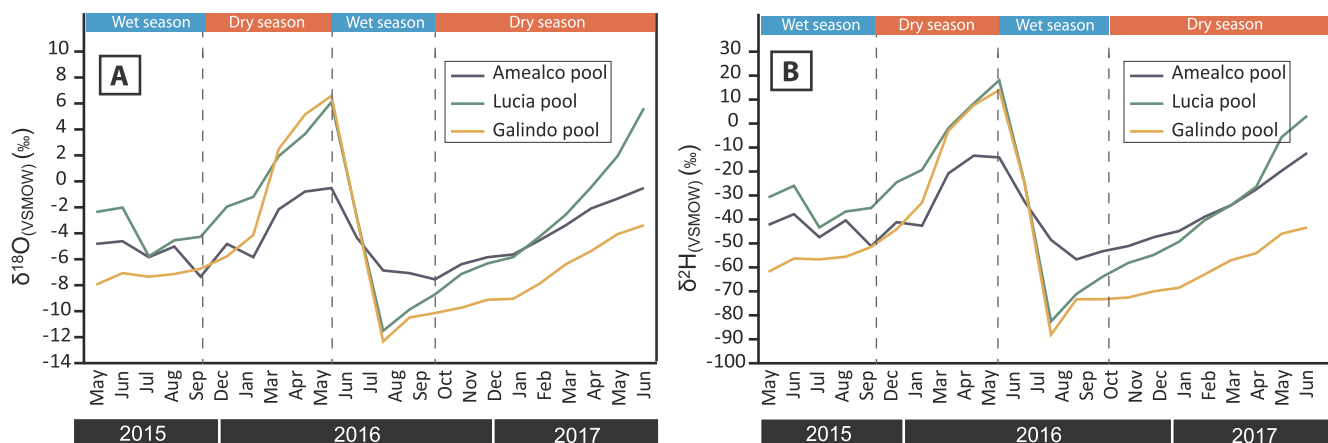


Fig. 7. Time series of (A) $\delta^{18}\text{O}$ and (B) $\delta^2\text{H}$ isotopic seasonal evolution of Amealco, Lucia and Galindo agricultural poolwaters from May 2015 to June 2017.

tropical areas (Pérez-Quezadas et al., 2015; Siegenthaler and Oeschger, 1980).

6. Isotopic evaporation model

Before solving the Craig and Gordon (1965) and Gonfiantini, (1986) evaporation models, we need to calculate the isotopic local limiting composition (δ^*), the (m) parameter and the total isotopic fractioning factor (Table EA5). The isotopic local limiting composition (δ^*) represents the maximum $\delta^{18}\text{O}$ - $\delta^2\text{H}$ isotopic ratio in the liquid fraction at which fractioning takes place. Above this value, the isotopic composition would not reflect the evaporation process, so the Craig-Gordon isotopic model would no longer be applicable. The calculated values of δ^* in all pools range from 0.29 to 33.06‰ for $\delta^{18}\text{O}$ and from 6.82 to 188.96 for $\delta^2\text{H}$. The $\delta^{18}\text{O}$ - $\delta^2\text{H}$ isotopic enrichment in the three agricultural pools never reached these conditions (Table EA5), and thus it can be assumed that C-G model is suitable and reliable. The m parameter describes the relationship between δ_e and δ_l at any instant at measured air temperature and relative humidity. The variation of the m value is comparable in all the studied pools and range from 0.65 to 4.49 for $\delta^{18}\text{O}$ and from 0.54 to 4.59 for $\delta^2\text{H}$ (Table EA5). The total isotopic fractioning factor (ϵ) is obtained solving Horita and Wesolowski (1994) equation.

Monthly evaporated fraction (f in %) values were estimated

following the $\delta^{18}\text{O}$ - $\delta^2\text{H}$ isotopic ratios throughout the 2015–2017 study period (Gonfiantini, 1986) for each agricultural pool water (Fig. 9).

These estimations have the minimum value at the end of wet season and the maximum value at the end of the dry season. For the Amealco pool the evaporated fraction varies from 1.3% to 30.6% for $\delta^{18}\text{O}$ and from 0.0% to 36.9% for $\delta^2\text{H}$. For the Lucia pool, the monthly evaporation estimations range from 0.0% to 51.0% for $\delta^{18}\text{O}$ and 0.0% from to 52.3% for $\delta^2\text{H}$. Finally, in the Galindo pool, f ranges from 0.0% to 53.5% at the end of dry season for $\delta^{18}\text{O}$ and 0.0% from to 52.4% for $\delta^2\text{H}$.

The obtained maximum $f(\delta^{18}\text{O}-\delta^2\text{H})$ values are comparable to those reported for African and Asian lakes in arid and semi-arid environment (Alazard et al., 2015; Delalande et al., 2008; Liu et al., 2016; Poulin et al., 2019; Wen et al., 2016). The negative $f(\delta^{18}\text{O}-\delta^2\text{H})$ values are related to the input of depleted rainwater in the system (Table EA5) and are always within the error margin of ($f = 0$), showing equilibrium between precipitation and evaporation volumes. Monthly $f(\delta^{18}\text{O}-\delta^2\text{H})$ exhibits a sinusoidal distribution through time (Fig. 8), where the ascending section of the sinusoidal function represents the evolution of the estimated evaporated fraction (f) in the pool's water. The slope represents the intensity variation of the instantaneous evaporation rate (% per unit of time) at a given time. The decreasing section of the sinusoidal function in May/June corresponds to the wet season, where the evaporated fraction (f) will no longer represent the monthly

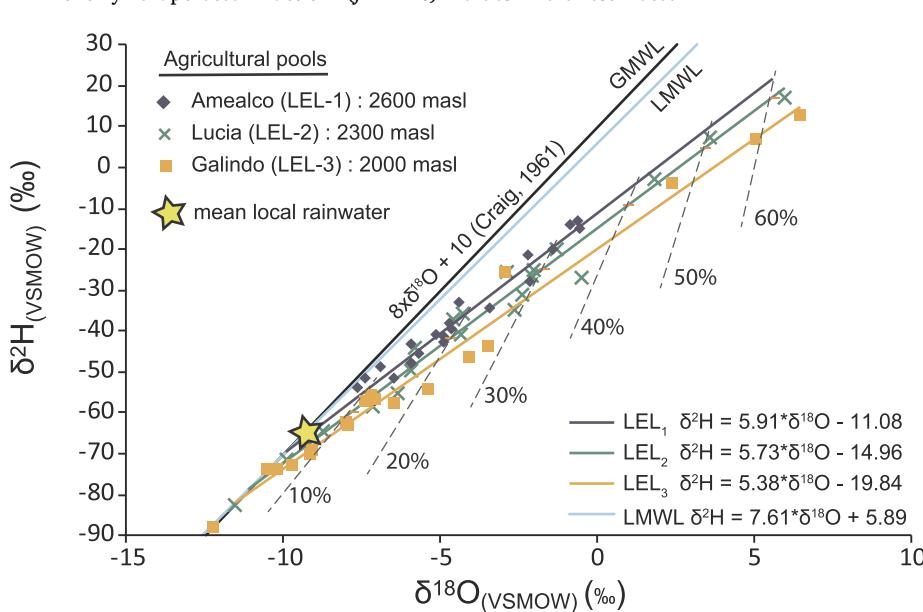


Fig. 8. $\delta^2\text{H}$ and $\delta^{18}\text{O}$ isotopic diagram relationship of Amealco (LEL-1), Lucia (LEL-2) and Galindo (LEL-3) agricultural poolwaters (from May 2015 to June 2017). An evaporation line was determinate for each agricultural poolwaters isotopic evolution. Dotted lines indicate the water evaporated fraction (f) in % for each agricultural pool, calculated by the Craig-Gordon and Gonfiantini method.

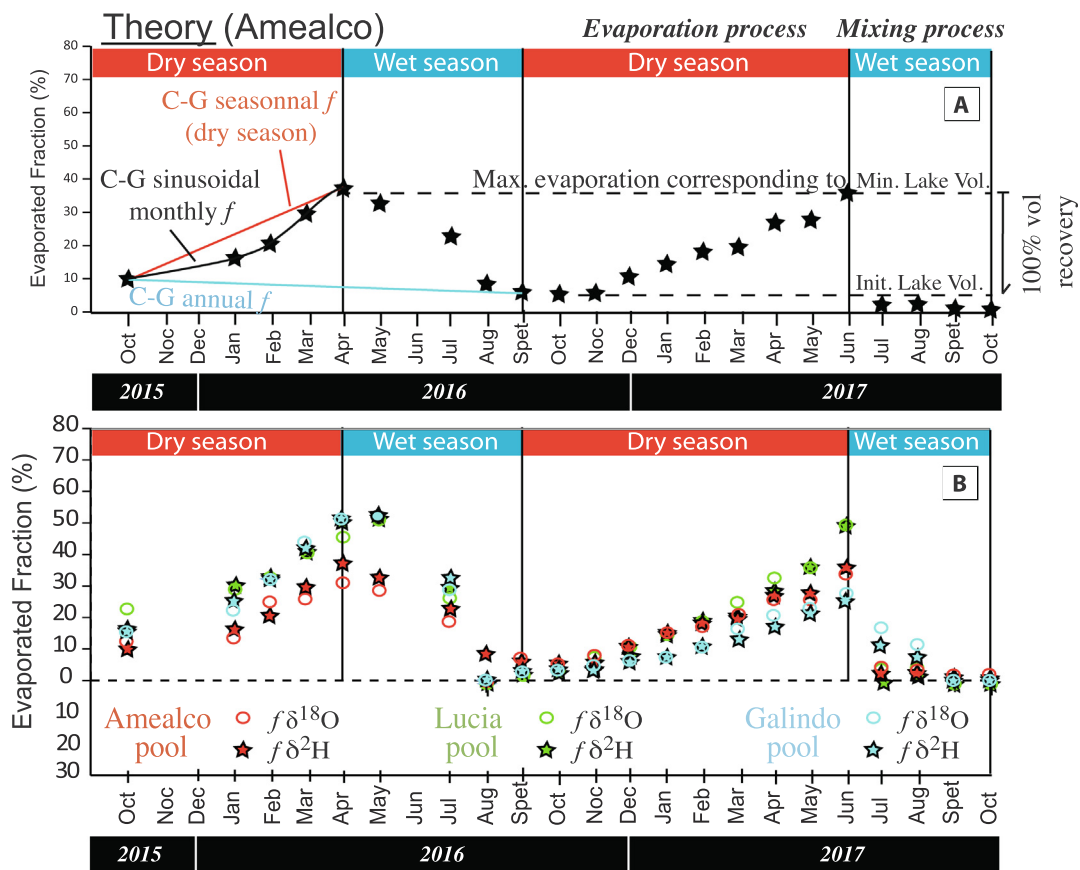


Fig. 9. (A) Theoretical and (B) monthly variation of $\delta^{18}\text{O}$ and $\delta^2\text{H}$ isotopic evaporated fraction (f in %) for Amealco, Lucia and Galindo agricultural poolwater.

evaporation accumulated in a closed system, but an isotopic mass balance process between both the precipitation and evaporation volumes (Fig. 9). Small behavior variations between the three pools illustrate the punctual meteoric and precipitation intensity variations. Such difference is highlighted by comparing the 2016 and 2017 wet seasons in the Lucia and Amealco pools. The precipitation registered in 2017 is lower than in 2016, although the 2017 precipitation events were more intense: in a single event the precipitation runoff volume fills up both pools up to 100% (Fig. 9).

7. Discussion

The C-G model is understood as a linear model that can be applied to a closed isotopic system lake (Figs. 8 and 9A). The C-G model illustrates the equilibrium isotopic in the isotopic composition between two reservoirs, (1) the water moisture in the atmosphere as relative humidity (δ_a) and (2) the pool water in liquid phase (δ_r) at a given time and air temperature. Accordingly, the maximum evaporation rate and mean intensity will depend on the sampling period (Fig. 9). In a semi-arid environment, such as the SJRB and under a monthly controlled monitoring, the evaporation process has a sinusoidal response – rather than the expected lineal behavior (Figs. 8, and 9). The variations of the monthly f show that evaporation volumes throughout the year are not constant and cannot be considered as a single measurement in the annual mass balance water budget. The f evolution during the wet season (Fig. 9A and B) does not represent a simple evaporation process but a competition between evaporation and multi reservoir isotopic mixing (air vapor – rainwater – pool water). As dry and wet season represent different isotopic processes – evaporation and mixing – they are explained by different functions (Fig. 9A). The monthly variation illustrates the relevance of punctual tracing of the isotopic composition in pool water and of the variation in the atmospheric isotopic conditions

through time in order to allow us to determine: (1) the breaking point of the maximum f value at the end of the dry season, (2) the initial f value to estimate the lake volume recuperation %, and finally (3) to illustrate the variation of water loss by evaporation (Fig. 9A and B).

The Craig-Gordon model is controlled by the variation of air temperature, relative humidity, air vapor and the initial isotopic values at the water pool. In arid to semi-arid environments, air temperature and relative humidity show large seasonal variations (0.9 °C to 33.9 °C and 14% to 100% respectively). Different authors have previously mentioned the sensitivity of the Craig-Gordon model to relative humidity (Kumar and Nachiappan, 1999; Wen et al., 2016) and the impact of several variables such as air temperature, relative humidity and water salinity on the water body isotopic fractioning were tested and integrated in the Gonfiantini et al. (2018) evaporation isotopic model. Majidi et al. (2015) shows that the most important factors affecting the evaporation process are solar radiation and wind speed, far ahead from air temperature and relative humidity used in the G-C model (Bowen, 1926; Majidi et al., 2015; Penman, 1948; Priestley and Taylor, 1972; Webb, 1966). Solar radiation is indirectly considered in the C-G model through air temperature and relative humidity; nevertheless, the solar radiation might have a strong effect in isotopic fractioning as the energy states of molecule bonding are a result of the energy in the water molecule as described by the quantum-mechanical harmonic oscillator theory (Chabal, 1988). In an high altitude semi-arid environment, the solar radiation is high (up to 1500 W m^{-2}) in particular the infrared range-and the most energetic input in the air-water boundary layer significantly increases the water molecule vibrational energy states, favoring isotopic fractioning independently of air temperature (Chabal, 1988). Recently it has been noticed that wind speed has a comparable effect on kinetic air-water equilibrium during evaporation at the water surface (Benetti et al., 2014).

The isotopic composition of air vapor (δ_a) is generally the least

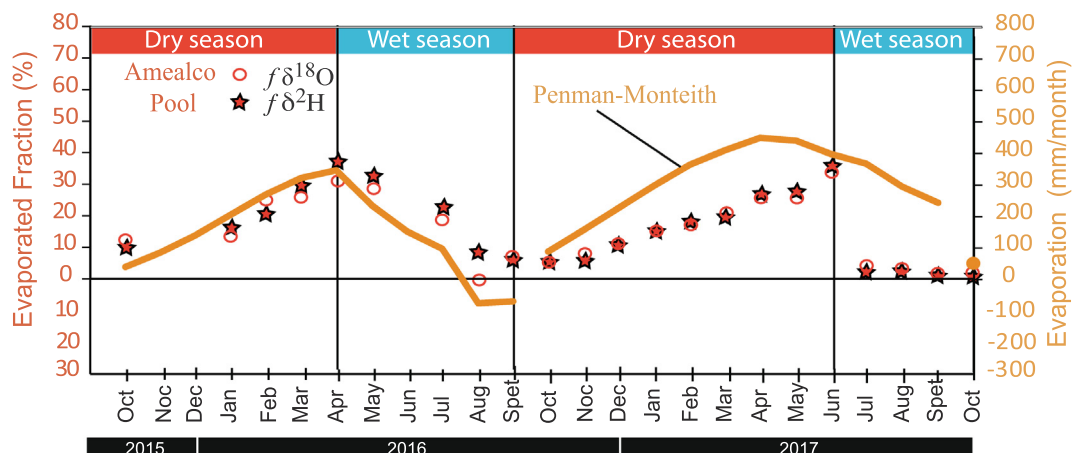


Fig. 10. Comparison diagram of the cumulative curves of Amealco pool, of monthly physical evaporation using the Penman-Monteith equation corrected with monthly precipitation, and the isotopic evaporated fraction ($f \delta^{18}\text{O}$, $\delta^2\text{H}$) obtained by Craig-Gordon evaporation method.

known constrained parameter, introducing the largest uncertainty into the Craig-Gordon model calculations. As δ_a measurements are relatively rare and difficult to obtain, it is commonly accepted to apply regional and/or annual mean δ_a values or to estimate a theoretical δ_a value through an isotopic water vapor/rain equilibrium equation (Gibson, 2002). As previously shown, local monthly δ_a variations show significant annual variation ($\sigma_{\delta_a} = 5.3\text{‰}$) showing that water vapor atmospheric composition can not be represented by a punctual or annual mean δ_a value. The commonly used theoretical δ_a estimation, is validated by the assumption that δ_a is in isotopic equilibrium with the mean isotopic precipitation value. In our case, rain water sampling was limited to less than 60 days per year, mostly during the wet season. These conditions do not allow a reliable statistical representation of the δ_a annual variation. Hence, the δ_a values should be interpreted in terms of regional climatology, as a function of seasonal displacement of air masses, and of the increase of convective activity during summer. The theoretically estimated δ_a during the wet season can not represent the comparable isotopic system and the evaporation conditions occurring during the dry season. The isotopic closed system representation of the air vapor isotopic reservoir, during the wet or dry season, is not realistic in a natural environment. In addition to these synoptic effects, atmospheric vapor may also contain a significant fraction of local recycling humidity from the lake evaporation (Gat et al., 1994). All monitored water pools are considered closed systems because they are located on consolidated ignimbrite flows with low permeability, and more than 200 m above the reported piezometric level. During the dry season, no lateral or upward flows alter the isotopic signature of these water reservoirs. During the dry season when the volume decreases to a minimum level the evaporative loss fraction f should reflect the Rayleigh distillation effect as the result of the isotopic enrichment in a closed pool water system. The monthly variations of the input isotopic data of the liquid or atmospheric phase force us to take into account the physicochemical criteria and define the different periods of the process to carry out a representative sampling over time (Fig. 9). During the rainy season the main isotopic process can be simplified as a multi components isotopic mixing equilibrium equation. The main components are the remaining evaporated pool water, air vapor and rainwater. In an undersaturated or saturated humidity environment, the isotopic composition of air vapor isotopic composition is controlled by isotopic composition of the rainwater reservoir (Poulin et al., 2019). In this way equilibrium equation is resumed at two main components, and f evolution illustrates their mixing process, as rainwater and runoff inflow into each pool and with a progressive restoration of the initial pool water volume and isotopic signature (Figs. 8 and 9).

In a semi-arid environment, the time period is limited by changes between the dry and wet season. Sampling on a monthly basis allows us

to illustrate and interpret a first order of evaporation and the pool refilling variation signal. Probably a weekly sampling will improve the evolution of the evaporation process and will likely show a second order of signal variation during wet season, highlighting the role of the gentle evaporation process during the weeks without rain. As previously shown, the monthly monitoring deeply increases the scope of the C-G model. In this way the C-G model is not just a method to estimate the punctual maximum evaporation, but also a reliable tool to illustrate the lake's hydrodynamics through the years (Fig. 9).

Various authors have tried to relate both isotopic and physical evaporation estimations with more or less significant success (Alazard et al., 2015; Blaney and Criddle, 1950; Bowen, 1926; Gibson et al., 1999, 2016; Gonfiantini, 1986; Hamon, 1960; Makkink, 1957; Penman, 1948, 1956; Skrzypek et al., 2015; Valiantzas, 2006). Both isotopic and physical methodologies show a comparable evaporation process during the dry season, when there is no precipitation or water input into the water body. However, during the rainy season this comparison is no longer representative. To overcome this issue, we included precipitation in the Penman-Monteith estimation (Fig. 4B) in order to transform it to an evaporation – precipitation mass balance, allowing us to compare both methods. The comparison between both physic and isotopic methods is illustrated in Fig. 10. The $\delta^2\text{H}$ and $\delta^{18}\text{O}$ estimated f show a similar sinusoidal distribution with the maximum evaporation accumulation during the final stages of the dry season (April 2016 and June 2017) and a progressive mixing of reservoirs during the wet season. The low initial isotopic ratio suggests a hydraulic recuperation of the pool initial volume, which is not possible to be estimated as isotopic estimations can not be negative. On the contrary, the Penman-Monteith mass balance shows a similar biannual sinusoidal distribution; however, when precipitation exceeds evaporation a negative shift can be observed (August and September 2016) indicating that this water volume is available to recharge the SJRB. In 2017 the physic and isotopic estimations show different patterns, particularly during June and July. The isotopic method presents a rapid drop below the initial values, while the physic method presents a smoother evolution. This behavior difference can be explained by the geographic representation of both methods: the physical method is representative of the punctual meteorological conditions obtained from the weather station, while the Craig-Gordon method is a mass balance between air vapor and remnant liquid phase from the pool water. During the wet season the pool water is not only filled up by local precipitation but also with micro basin runoff, which significantly increases the water input in the mass balance system. Finally, the Craig-Gordon method is an isotopic mass balance in which the estimate of the evaporated fraction (f) is calculated based on the initial and final isotopic composition of water in the reservoir. The variation of this period-daily, monthly or annual-has a

significant impact of the f estimation (Fig. 9A). The evaporation estimates based on the Penman-Monteith method are determined on daily basis and will not be affected by time sampling variation (Fig. 4A).

The Penman-Monteith and the C-G evaporation methods were designed to illustrate an apparently simple process, evaporation. But by their intrinsic nature they really reflect different aspects of the same process. The information obtained by both methods are not redundant and directly comparable, but complementary and are useful to better illustrate the “evaporation process” in a hydrologic basin.

8. Conclusion

This study revisits isotope mass balance concepts that have been developed and applied in various climatic regions over the past five decades; however, few detailed studies have been conducted in semi-arid region environments. The enhanced seasonality of the semiarid continental environment of our study site provided an ideal setting for natural experimental testing of basic field approaches for characterizing C-G isotopic model within a highly variable atmospheric and hydrologic system.

We systematically report water isotopic signatures from rainfall, atmospheric vapor and agricultural pools, providing an integral framework to reliably solve the C-G isotopic model. We establish the first isotopic framework at a basin scale to guide the interpretation and monitoring of isotopic signatures in Mexico. We highlight the usage of monthly isotopic signatures to improve the representing and tracing water in the SJR semiarid basin.

It was found that in an environment with extreme seasonality the evaporation rates vary dramatically, and the evaporation process is not well represented as a linear model. The C-G isotopic model represents the evaporation process only during the dry season when no other water sources such as rain, atmospheric vapor and/or groundwater, perturb the pool isotopic variation. During the wet season, the C-G isotopic model does not longer illustrate the evaporation process but the isotopic water balance in pools. The C-G isotopic model was applied in conjunction with a conventional physical evaporation model to constrain and compare short-term (monthly) water balance variations in pools. Beyond a common objective of representing the evaporation rate and process, the isotopic and physical models cannot be compared. They are complementary approaches which are useful in the understanding of the “evaporation process” meaning in hydrologic basin.

Declaration of Competing Interest

The authors declare that they have no known competing financial interests or personal relationships that could have appeared to influence the work reported in this paper.

Acknowledgments

This research is part of the first author's PhD project in the framework of the Universidad Nacional Autónoma de México (UNAM) Postgraduate Program. The research was funded by CONACYT grant CB-255070 to G. Levresse. We thank Comité Técnico de Aguas Subterráneas SJR, Junta de Agua Potable y Alcantarillado Municipal SJR, and Comisión Estatal de Aguas Querétaro for sharing information and logistical support. We thank Marina Vega and Carolina Muñoz for assistance at the Cortical Fluid Laboratory and Pedro Morales, Francisco Otero, and Edith Cienfuegos for technical assistance with the ^{2}H - ^{18}O analyses at the Laboratorio Universitario de Geoquímica Isotópica. The authors thank Juan Pablo Bernal Uruchurtu, and two anonymous reviewers for constructive and enjoyable discussions and review.

HydroShare is thanked for the hosting and help in managing the supplementary data. Data are available at the following link: <http://www.hydroshare.org/resource/27d407bdfd9e4a479b67c5f385a8e4a1>.

www.hydroshare.org/resource/27d407bdfd9e4a479b67c5f385a8e4a1.

Appendix A. Supplementary data

Supplementary data to this article can be found online at <https://doi.org/10.1016/j.jhydrol.2020.124926>.

References

- Alazard, M., Leduc, C., Travi, Y., Boulet, G., Ben Salem, A., 2015. Estimating evaporation in semi-arid areas facing data scarcity: example of the El Haouareb dam (Merguellil catchment, Central Tunisia). *J. Hydrol.: Reg. Stud.* 3, 265–284. <https://doi.org/10.1016/j.ejrh.2014.11.007>.
- Ali, S., Narayan, G., Ranvir, S., 2008. Evaluating best evaporation estimate model for water surface evaporation in semi-arid region, India. *Hydrol. Process.* 22, 1093–1106. <https://doi.org/10.1002/hyp.6664>.
- Araguás-Araguás, L., Froehlich, K., Rozanski, K., 2000. Deuterium and oxygen-18 isotope composition of precipitation and atmospheric moisture. *Hydrol. Process.* 14, 1341–1355.
- Benetti, M., Reverdin, G., Pierre, C., Merlivat, L., Risi, C., Steen-larsen, H.C., Vimeux, F., 2014. *J. Geophys. Res.* 584–593. <https://doi.org/10.1002/2013JD020535.Received>.
- Blaney, H.F., & Criddle, W.D. (1950). Determining water requirements in irrigated areas from climatological and irrigation data. U.S.D.A., 43.
- Bowen, I.S., 1926. The ratio of heat losses by conduction and by evaporation from any water surface. *Phys. Rev.* 27, 779–787. <https://doi.org/10.5194/hess-20-823-2016>.
- Cai, J., Liu, Y., Lei, T., Pereira, L.S., 2007. Estimating reference evapotranspiration with the FAO Penman-Monteith equation using daily weather forecast messages. *Agric. For. Meteorol.* 145 (1–2), 22–35.
- Calva-Hernández, D., 2011. Caracterización isotópica de la precipitación en el Estado de San Luis Potosí. Universidad Autónoma de San Luis Potosí Universidad Autónoma de San Luis Potosí.
- Carrera-Hernández, J.J., Levresse, G., Lacan, P., Aranda-Gómez, J.J., 2016. A low cost technique for development of ultra-high resolution topography: application to a dry maar's bottom. *Rev. Mexicana de Ciencias Geol.* 33 (1), 122–133.
- Chabal, Y.J., 1988. Surface infrared spectroscopy. *Surf. Sci. Rep.* 8.
- Coplen, T.B., 1988. Normalization of oxygen and hydrogen isotope data. *Chem. Geol.* Isotope Geosci. Sect. 72 (4), 293–297. [https://doi.org/10.1016/0168-9622\(88\)90042-5](https://doi.org/10.1016/0168-9622(88)90042-5).
- Cortés-Silva, A., Farvolden, R.N., 1989. Isotope studies of precipitation and groundwater in the sierra de las Cruces, Mexico. *J. Hydrol.* 107, 147–153.
- Craig, H., & Gordon, L. (1965). Deuterium and oxygen 18 variations in the ocean and the marine atmosphere.
- Delalande, M., Bergonzini, L., Massault, M., 2008. Mbaka lakes isotopic (^{18}O and ^{2}H) and water balances: Discussion on the used atmospheric moisture compositions. *Isot. Environ. Health Stud.* 44 (1), 71–82. <https://doi.org/10.1080/10256010801887414>.
- Van Der Ent, R.J., Savenije, H.H.G., Schaefli, B., Steele-Dunne, S.C., 2010. Origin and fate of atmospheric moisture over continents. *Water Resour. Res.* 46 (9), 1–12. <https://doi.org/10.1029/2010WR009127>.
- Fellman, J.B., Dogramaci, S., Skrzypek, G., Dodson, W., Grierson, P.F., 2011. Hydrologic control of dissolved organic matter biogeochemistry in pools of a subtropical dryland river. *Water Resour. Res.* 47 (6), 1–13. <https://doi.org/10.1029/2010WR010275>.
- Fontes, J.C., Gonfiantini, R., 1967. Comportement Isotopique Au Cours De L'Evaporation. *Earth Planet. Sci. Lett.* 3, 258–266.
- Fritz, P., Fontes, J.C., 1986. Handbook of Environmental Isotope Geochemistry, The Terrestrial Environment, B.
- Gat, J.R., Levy, Y., 1978. Isotope hydrology of inland sabkhas in the Bardawil area Sinai. *Limnol. Oceanogr.* 23 (5), 841–850.
- Gat, J.R. (1981). Lakes. Stable Isotope Hydrology-Deuterium and Oxygen-18 in the Water Cycle In: J.R. Gat, R. Gonfiantini (Eds.). IAEA Technical Report Series No. 210, Vienna, pp. 203–221.
- Gat, J.R., Bowser, C.J., Kendall, C., 1994. The contribution of evaporation from the Great Lakes to the continental atmosphere: estimate based on stable isotope data. *Geophys. Res. Lett.* 21 (7), 557–560. <https://doi.org/10.1029/94GL00069>.
- Gat, J.R., 1996. Oxygen and hydrogen isotopes in the hydrologic cycle. *Annu. Rev. Earth Planet. Sci.* 24, 225–262. <https://doi.org/10.1146/annurev.earth.24.1.225>.
- Gat, J.R., 2002. Oxygen and hydrogen isotopes in the hydrologic cycle. *Annu. Rev. Earth Planet. Sci.* 24, 225–262. <https://doi.org/10.1146/annurev.earth.24.1.225>.
- Gat, J.R., Ben-Mair, R., Yam, R., Yakir, D., & Wernli, H. (2005). The isotope composition of atmospheric waters in Israel's coastal plain, Isotopic composition of precipitation in the Mediterranean Basin in relation to air circulation patterns and climate. International Atomic Energy Agency, Isotope Hydrology Section. Retrieved from http://www.iaea.org/inis/collection/NCLCollectionStore/_Public/36/110/36110957.pdf#page=132.
- Gibson, J.J., Bursey, G.G., 1993. Estimating Evaporation Using Stable Isotopes: Nord Hydrology 79–94.
- Gibson, J.J., Edwards, T.W.D., Prowse, T.D., 1999. Pan-derived isotopic composition of atmospheric water vapour and its variability in northern Canada. *J. Hydrol.* 217 (1–2), 55–74. [https://doi.org/10.1016/S0022-1694\(99\)00015-3](https://doi.org/10.1016/S0022-1694(99)00015-3).
- Gibson, J.J., 2002. Short-term evaporation and water budget comparisons in shallow Arctic lakes using non-steady isotope mass balance. *J. Hydrol.* 264 (1–4), 242–261. [https://doi.org/10.1016/S0022-1694\(02\)00091-4](https://doi.org/10.1016/S0022-1694(02)00091-4).
- Gibson, J.J., Birks, S.J., & Edwards, T.W.D. (2008). Global prediction of δ A and δ 2 H- ^{18}O evaporation slopes for lakes and soil water accounting for seasonality. Global

- Biogeochemical Cycles, 22(2),<https://doi.org/10.1029/2007GB002997>.
- Gibson, J.J., Reid, R., 2010. Stable isotope fingerprint of open-water evaporation losses and effective drainage area fluctuations in a subarctic shield watershed. *J. Hydrol.* 381 (1–2), 142–150. <https://doi.org/10.1016/j.jhydrol.2009.11.036>.
- Gibson, J.J., Birks, S.J., Yi, Y., 2016. Stable isotope mass balance of lakes: a contemporary perspective. *Quat. Sci. Rev.* 131, 316–328. <https://doi.org/10.1016/j.quascirev.2015.04.013>.
- Gonfiantini, R., 1986. Environmental Isotopes in Lake Studies. In: Fritz, J.C., P. and Fontes, (Eds.), *Handbook of Environmental Isotope Geochemistry. The Terrestrial Environment*. Elsevier, Amsterdam, pp. 113–168.
- Gonfiantini, R., Wassenaar, L., Araguás-Araguás, L., Aggarwal, P.K., 2018. A unified Craig-Gordon isotope model of stable hydrogen and oxygen isotope fractionation during fresh or saltwater evaporation. *Geochim. Cosmochim. Acta* 235, 224–236. <https://doi.org/10.1016/j.gca.2018.05.020>.
- Hamon, W.R., 1960. Estimating potential evapotranspiration. Institute of Technology, Massachusetts.
- Harbeck, G.E., 1962. A practical field technique for measuring reservoir evaporation utilizing mass-transfer theory Vol. 272 US Government Printing Office.
- Horita, J., Wesolowski, D.J., 1994. Liquid-vapor fractionation of oxygen and hydrogen isotopes of water from freezing to the critical temperature. Retrieved from. *Geochim. Cosmochim. Acta* 58 (16), 3425–3437. [https://doi.org/10.1016/0016-7037\(94\)90001-1](https://doi.org/10.1016/0016-7037(94)90001-1).
- Issar, A., Quijano, J.L., Gat, J.R., Castro, M., 1984. The isotope hydrology of the groundwaters of central Mexico. *J. Hydrol.* 71 (3–4), 201–224.
- Kumar, B., Nachiappan, R.P., 1999. On the sensitivity of Craig and Gordon model for the estimation of the isotopic composition of lake evaporates. *Water Resour. Res.* 35 (5), 1689–1691. <https://doi.org/10.1029/1999WR900011>.
- Lindau, R. (1995). A New Beaufort Equivalent Scale. Proceedings of the International COADS Wind Workshop, 232–252.
- Liu, X., Yu, J., Wang, P., Zhang, Y., Du, C., 2016. Lake evaporation in a hyper-arid environment, northwest of China-measurement and estimation. *Water* 8 (11), 1–21. <https://doi.org/10.3390/w8110527>.
- Luna-Niño, R., Cavazos, T., 2018. Formation of a coastal barrier jet in the Gulf of Mexico due to the interaction of cold fronts with the Sierra Madre Oriental mountain range. *Q. J. R. Meteorol. Soc.* 144 (710), 115–128. <https://doi.org/10.1002/qj.3188>.
- Majidi, M., Alizadeh, A., Farid, A., Vazifehdoust, M., 2015. Estimating evaporation from lakes and reservoirs under limited data condition in a semi-arid region. *Water Resour. Manage.* 29 (10), 3711–3733. <https://doi.org/10.1007/s11269-015-1025-8>.
- Makkink, G.F., 1957. Ekzameno De La Formulo De Penman. Retrieved from. Neth. J. Agric. Sci. 5, 290–305. https://hydrologie.org/BIB/Curiosa/Makkink_Neth.J.AgricSci1957.pdf.
- Monteith, J.L., 1981. Evaporation and surface temperature. *Quart. J. R. Meteo. Soc.* 1–27.
- Penman, H.L., 1948. Natural evaporation from open water, bare soil and grass. *Proc. R. Soc. A* 193 (1032).
- Penman, H.L. (1956). Estimating evaporation. *Eos, Transactions American Geophysical Union*, 37(1), 43–50. <https://doi.org/10.1029/TR037i001p00043>.
- Pérez-Quezadas, J., Cortés-Silva, A., Inguaaggiato, S., Salas-Ortega, M., Cervantes-Pérez, J., Heilweil, V.M., 2015. Meteoric isotopic gradient on the windward side of the sierra madre oriental area Veracruz - Mexico. *Geofisica Int.* 54 (3), 267–276. <https://doi.org/10.1016/j.gi.2015.04.021>.
- Poulin, C., Hamelin, B., Vallet-Coulomb, C., Amngar, G., Loukman, B., Cretaux, J.F., 2019. Unraveling the hydrological budget of isolated and seasonally contrasted subtropical lakes. *Hydrol. Earth Syst. Sci.* 23 (3), 1705–1724. <https://doi.org/10.5194/hess-23-1705-2019>.
- Priestley, C.H.B., Taylor, R.J., 1972. On the assessment of surface heat flux and evaporation using large-scale parameters. *Weather Rev.* 100 (2), 81–92.
- Rohwer, Carl. (1931). Evaporation from free water surface. Uo S. Department of Agriculture and Colorado Agricultural Experiment Station Technical Bulletin, 27, 1–96.
- Siegenthaler, U., Oeschger, H., 1980. Correlation of ¹⁸O in precipitation with temperature and altitude. *Nature* 285 (5763), 314–317. <https://doi.org/10.1038/285314a0>.
- Skrzypek, G., Mydlowski, A., Dogramaci, S., Hedley, P., Gibson, J.J., Grierson, P.F., 2015. Estimation of evaporative loss based on the stable isotope composition of water using Hydrocalculator. *J. Hydrol.* 523, 781–789. <https://doi.org/10.1016/j.jhydrol.2015.02.010>.
- Tsujimura, M., Abe, Y., Tanaka, T., Shimada, J., Higuchi, S., Yamana, T., Davaa, G., Oyunbaatar, D., 2007. Stable isotopic and geochemical characteristics of groundwater in Kherlen River basin, a semi-arid region in eastern Mongolia. *J. Hydrol.* 333, 47–57. <https://doi.org/10.1016/j.jhydrol.2006.07.026>.
- Valiantzas, J.D., 2006. Simplified versions for the Penman evaporation equation using routine weather data. *J. Hydrol.* 331 (3–4), 690–702. <https://doi.org/10.1016/j.jhydrol.2006.06.012>.
- Verma, M.P., Fernandez, M.E., Quijano, J.L., Johnson, C., 2000. Chemical and isotopic monitoring of rainfall around the los azufres and los humeros geothermal systems: preliminary results. *Proc. World Geotherm. Congr.* 2000 (2), 731–735.
- Webb, E.K., 1966. A pan-lake evaporation relationship. *J. Hydrol.* 4, 1–11.
- Welhan, J.A., Fritz, P., 1977. Evaporation pan isotopic behavior as an index of isotopic evaporation conditions. *Geochim. Cosmochim. Acta* 41 (5), 682–686. [https://doi.org/10.1016/0016-7037\(77\)90306-4](https://doi.org/10.1016/0016-7037(77)90306-4).
- Wen, X., Yang, B., Sun, X., Lee, X., 2016. Evapotranspiration partitioning through in-situ oxygen isotope measurements in an oasis cropland. *Agric. For. Meteorol.* 230–231, 89–96. <https://doi.org/10.1016/j.agrformet.2015.12.003>.
- Werner, R.A., Brand, W.A., 2001. Referencing strategies and techniques in stable isotope ratio analysis. *Rapid Commun. Mass Spectrom.* 15 (7), 501–519. <https://doi.org/10.1002/rcm.258>.
- Zimmerman, U., 1979. Determination by stable isotopes of underground inflow and outflow and evaporation of young artificial groundwater lake. In: *Isotopes in lake studies. In: Isotopes in lake studies. International Atomic Energy Agency, Vienna*, pp. 97–194.

Capítulo III :

**Geochemical and isotopic multi-tracing ($\delta^{18}\text{O}$, $\delta^2\text{H}$, $\delta^{13}\text{C}$, $\Delta^{14}\text{C}$) of
groundwater flow dynamics and mixing patterns in the
volcanoclastic aquifer of the semiarid San Juan del Río Basin in
Central México.**



REPORT



Geochemical and isotopic multi-tracing ($\delta^{18}\text{O}$, $\delta^2\text{H}$, $\delta^{13}\text{C}$, $\Delta^{14}\text{C}$) of groundwater flow dynamics and mixing patterns in the volcanoclastic aquifer of the semiarid San Juan del Río Basin in central Mexico

Eliseo Hernández-Pérez¹ · Gilles Levresse² · Jaime Carrera-Hernandez² · Claudio Inguaggiato³ · Marina Vega-González² · Fernando Corbo-Camargo² · Dora Celia Carreón-Freyre² · Andrea Billarent-Cedillo¹ · Francisco Javier Sancén Contreras⁴ · Cynthia Paola Ramírez Hernández⁴

Received: 30 March 2022 / Accepted: 30 August 2022

© The Author(s), under exclusive licence to International Association of Hydrogeologists 2022

Abstract

Water supply in semiarid areas in Mexico depends on water extraction from compartmentalized aquifers where large drawdown rates can be observed due to increasing demand from urban, industrial and agricultural users. Understanding the behavior of these aquifers is a necessity in order to improve the estimation of water balances. Accordingly, this study assembles both geochemical and isotopic data to identify the source of recharge to the San Juan del Río graben aquifer and to determine its dynamics. The geological model developed with the aforementioned data reveals a complex system composed of a heterogeneous multilayered compartmentalized aquifer. The San Juan del Rio basin is composed of (1) the Amealco perched aquifer, (2) a shallow granular aquifer, and (3) a fractured aquifer. Hydrogeochemical and isotopic data ($\delta^2\text{H}$, $\delta^{18}\text{O}$, $\delta^{13}\text{C}$ and correct carbon activity ($\Delta^{14}\text{C}$)) allow for identification of three end-member sources: (1) local meteoric recharge, (2) old groundwater contained in the siliciclastic shallow aquifer, and (3) regional/local hydrothermal recharge. The contribution of both meteoric and regional hydrogeothermal flow to the different aquifer compartments is determined through a principal component analysis of the hydrogeochemical data. With the aforementioned analysis it was found that the dominant contribution source for all aquifer compartments is meteoric water (up to 60% with a median of 50%), while the regional hydrothermal groundwater contribution represents 15%, even for the shallow aquifer.

Keywords Stable isotopes · Hydrochemistry · Groundwater monitoring · Mexico · Arid regions

Francisco Javier Sancén Contreras is deceased

✉ Gilles Levresse
glevresse@geociencias.unam.mx

¹ Posgrado en Ciencias de la Tierra, Centro de Geociencias, Universidad Nacional Autónoma de México, Blvd. Juriquilla No. 3001, C.P. 76230 Querétaro, México

² Centro de Geociencias, Universidad Nacional Autónoma de México, Blvd. Juriquilla No. 3001, C.P. 76230 Querétaro, México

³ Departamento de Geología, Centro de Investigación Científica y de Educación Superior de Ensenada (CICESE), Carretera Ensenada-Tijuana, 3918 Ensenada, Baja California, México

⁴ Comité Técnico de Aguas Subterráneas del acuífero de San Juan del Rio, Querétaro, México

Introduction

Excessive groundwater extraction in Mexico is a serious problem, as 100 out of the 188 most important aquifers in the country are overexploited (Cruz-Ayala and Megdal 2020), with the water-table drawdown rates reaching 2.5 m in some regions (Carrera-Hernandez 2018). The growth in population, urbanization, agriculture and industrialization are the primary drivers of the increase in water use, resulting in water scarcity and deterioration of water quality. Such unsustainable management is becoming a threat to development in Mexico and will be a survival issue soon. The northern half of the Mexican territory (up to 60%) is comprised of dry, semiarid, arid, and hyperarid environments; paradoxically, these are the regions where the largest irrigation systems and urban areas are found. Accordingly,

natural conditions and groundwater overexploitation have led to a water-stressed state in the country. The largest Mexican cities already suffer recurrent events of water scarcity (Arreguín-Cortés et al. 2020; Gleason and Flores 2021), and climate change models along with population growth for the next 30 years suggest that these regions will be facing severe water scarcity (Arreguín-Cortés et al. 2020).

In addition to both climatic and anthropogenic issues, the northern Mexican aquifers have major geological limitations. Most of the aquifers' geographic extensions are limited by the Basin and Range regional structures. These "graben siliciclastic shallow aquifers" are generally described as multilayered and compartmented aquifers (Arango-Galván et al. 2011; Billarent-Cedillo et al. 2021; Carrera-Hernández et al. 2016; Guerrero-Martínez et al. 2018; Sanchez et al. 2018 among others). Moreover, groundwater overexploitation in volcanic aquifers seems related to local thermal anomalies and increase in natural As, F, Cr, Cs concentrations (Morales et al. 2015; Rodríguez et al. 2016). Despite the fact that groundwater is the main water source available for public use in Mexico, to date there is a lack of knowledge regarding the interaction of meteoric water with groundwater and of the understanding of regional and local groundwater flows, leading to simplistic estimations of aquifer recharge (Cruz-Ayala and Megdal 2020).

In order to improve the understanding of aquifers in the aforementioned regions, this study integrates both available and new geological information, along with hydrogeochemical and isotopic data to develop a robust conceptual model of the San Juan del Rio (SJR) hydrogeological basin. With this information, the proportion of meteoric, regional and hydrothermal water contributions to the SJR aquifer is estimated to obtain a more realistic hydrological water budget, as both regional and hydrothermal water flows are generally overlooked.

Study area

General settings

The San Juan del Rio Basin (SJR) is located at the junction of the Mesa Central (MC), the Trans Mexican Volcanic Belt (TMVB), and the Sierra Madre Oriental (SMOr) geological provinces (Fig. 1a). The boundary between the MC and SMOr is the Taxco-San Miguel de Allende Fault System (TSMFS; Fig. 1b), which is a regional structure that extends across the TMVB with a N–S direction (Alaniz-Álvarez and Nieto-Samaniego 2005). The TMVB is an E–W active continental volcanic arc with a 1,200-km length across central Mexico (Ferrari et al. 2000). The SJR graben is formed at the intersection of the Taxco–San Miguel de Allende fault system (Alaniz-Álvarez et al. 2001) and the Chapala–Tula

fault system (CTFS), which is subparallel to the TMVB (Alaniz-Álvarez and Nieto-Samaniego 2005; Fig. 1b). The SJRB is an intramountain exorheic basin with an extension of 2,800 km² located in the state of Queretaro with elevations that range from 1,900 to 3,200 m above sea level (asl). The drainage network is dendritic, formed by numerous ephemeral streams which flow mainly during the rainy season. The two main water bodies of this basin have been created by two dams, *San Ildefonso* and *Constitución de 1917*, with a total estimated volume of ~75 Mm³ (Fig. 1c). Due to its geographical location, the SJRB receives humid air masses during the rainy season from both the Atlantic and the Pacific Oceans (Van Der Ent et al. 2010; Luna-Niño and Cavazos 2018).

Geological settings

Two regional fault systems converge in the SJRB, thus creating an arrangement of orthogonal faults that define rectangular-shaped blocks with normal differential displacements, resulting in a mosaic of horsts, grabens and half grabens with a depression at the center of the valley (Fig. 1). The general stratigraphic column in the SJRB (Fig. 2) consists of a regional Cretaceous basement covered by a sequence of alternating layers of Paleogene–Neogene volcanic rocks and continental and lacustrine sedimentary material (Martini et al. 2016). The basement does not outcrop in the SJRB but is exposed in the northern part of the nearby Queretaro aquifer—in Juriquilla (Carrera-Hernández et al. 2016)—and is comprised of limestone with interbedded shales and sandstone. The transition between the basement and the Tertiary volcanic series is highlighted by a continental conglomerate, which does not outcrop on the study area, but is equivalent to the Guanajuato Red Conglomerate of the Eocene (Aranda-Gómez and McDowell 1998). The oldest volcanic eruption occurred at ~30 Ma (Aguirre-Díaz and López-Martínez 2001) and is recognized as the last ignimbrite flow of the Sierra Madre Occidental volcanic sequence (ToR; (Aguirre-Díaz and López-Martínez 2001; Ferrari et al. 2018). This is the last unit with regional extension and represents the basement of the Miocene bimodal volcanic calderas and extensional graben development (Aguirre-Díaz 1996; Aguirre-Díaz and López-Martínez 2001, 2009; Alaniz-Álvarez and Nieto-Samaniego 2005; Dávalos-Álvarez et al. 2005). The Miocene volcanism started with local events consisting of mafic-intermediate lava flows known as La Cuesta latite (Tlc), the Vaquerias andesite (Tav) and the pre-caldera andesite (Tmt AB). The pre-caldera andesite group (Tmt AB) exhibits different outcrops of comparable age and chemistry, forming plateaus, shield volcanoes and monogenetic cinder cones with the radiometric ages ranging from 8.8 to 7.5±0.5 Ma. (Aguirre-Díaz and López-Martínez 2001; Dávalos-Álvarez et al. 2005). From late Miocene (~7.3

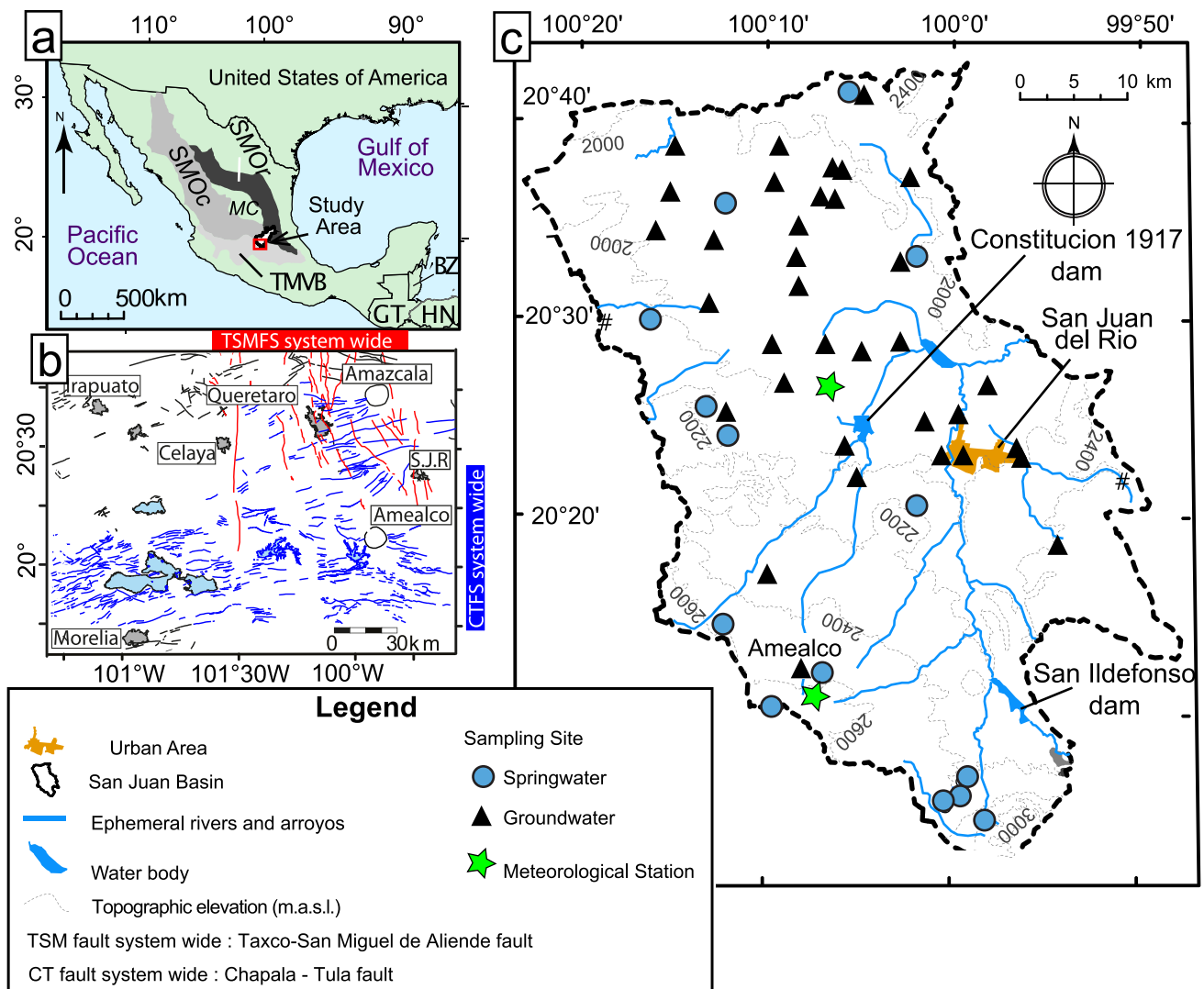


Fig. 1 **a** Location of the study area and its relationship with the Mexican physiographic provinces in Central México. **b** Regional structural map. The Taxco-San Miguel de Allende Fault System is identified in red and the Chapala-Tula Fault System in blue. Black lines are recent structures not associated with these fault systems. **c** Distribution of

ephemeral rivers, main dams, groundwater wells, springs and meteorological stations in the San Juan del Rio Basin. San Juan del Rio city (SJR). Altitude and piezometric levels are given in m above sea level (asl)

Ma) to late Pliocene (~3.4 Ma), the volcanic activity corresponded to the growing and collapse of a succession of volcanic calderas from north to south (Aguirre-Díaz and López-Martínez 2001), topographically closing the SJRB. The Amazcala caldera, located at the northern limit of the SJRB, is the oldest (7.3–6.6 Ma) with a $11 \times 14 \text{ km}^2$ elliptical shape and rhyolitic products. The caldera rim is occupied by several rhyolite lava domes and flows, some of which extend 10 km from the rim. The first calderic volcanic event is the Ezequiel Montes pumice (EMP), which is a widespread pumice fallout emplaced around 7.3 Ma ago, while the last caldera event is an intracaldera rhyolitic dome that occurred about 6.6 Ma—between the aforementioned caldera events, when fissural volcanic flows took place. At the

north of the SJRB, the ash andesite (Tpca, 5.2 ± 0.2 Myr) and the San José basalt (Tbsj) form the northeastern sierras, while the La Loma andesite (Tla, 4.8 Myr) formed the topographical heights on its southwestern side (Aguirre-Díaz and López-Martínez 2001). During the Pliocene, the caldera activity moved towards the southeast, creating the *Huichapan* and *Amealco* calderas. The *Huichapan* caldera complex is comprised of two overlapping events: a first caldera formed at 5.0 ± 0.3 Ma, with the eruption of several andesitic to trachydacitic pyroclastic flows, and at 4.6 ± 0.3 Ma; the rim of this caldera was delimited by small shield volcanoes and cinder cones along with their related basaltic-andesite and andesitic lava flows. The second caldera was formed at 4.2 ± 0.2 Ma and is characterized by the *Huichapan*

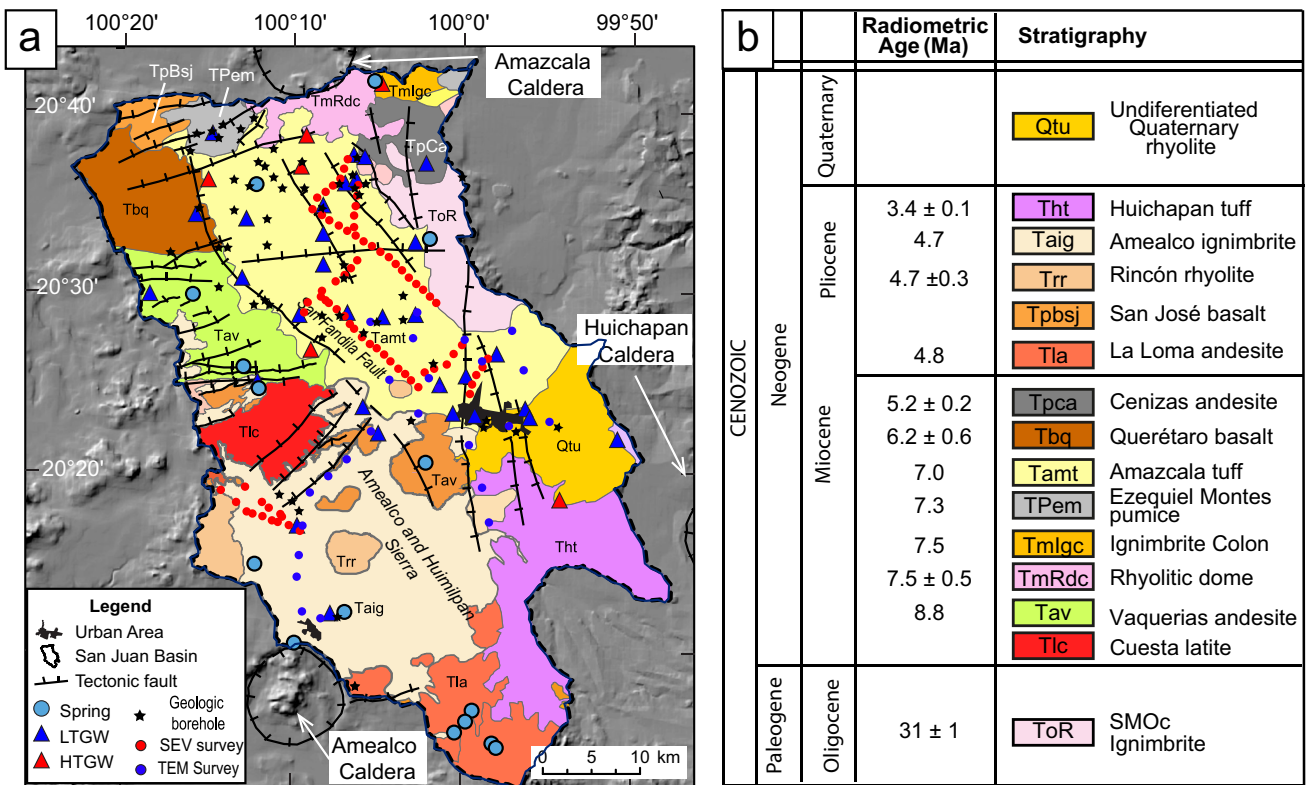


Fig. 2 **a** Simplified geological map of the San Juan del Río Basin. **b** A simplified stratigraphic column and main tectonic structures as reported by local research (Aguirre-Díaz 1996, 1995; Aguirre-Díaz and López-Martínez 2009; Aguirre-Díaz and McDowell 2007; Alaniz-Álvarez et al. 2001; Alaniz-Álvarez and Nieto-Samaniego

2005; Carreón-Freyre et al. 2005; Dávalos-Álvarez et al. 2005). LTGW: low-temperature groundwater; HTGW: high-temperature groundwater; VES: vertical electrical sounding survey; TEM: transient electromagnetic survey; SMOc Ignimbrite: Sierra Madre Occidental Ignimbrite (31.1 Ma)

Tuff; during this period, several trachydacitic lava domes were extruded along the new ring fracture and delimited the second rim of the Huichapan caldera. At the same time that the aforementioned events occurred, the Amealco caldera event took place as well. The major volcanic units related to the Amealco caldera are the Rincón Rhyolite, (4.7 ± 0.3 Ma, Trr), the Amealco Tuff (4.68 ± 0.1 Ma; Tat) and the Amealco Ignimbrite (4.7 Ma; Taig) (Aguirre-Díaz 1995, 1996). Finally, a group of Quaternary undifferentiated rhyolitic domes took place in the southeastern part of the basin (Aguirre-Díaz 1996; Aguirre-Díaz and López-Martínez 2009).

Hydrological settings

In the SJRB, groundwater is extracted through 974 wells, for agriculture, industry and urban purposes, with a yearly allowed extraction volume of approximately 324 Mm^3 . The wells vary in depth (5–600 m). Most of the wells ($n = 491$) reach a depth that varies from 135 to 300 m, corresponding to the graben sedimentary filling (Fig. 3a,b). The remaining wells can be classified as either shallow (50–135 m)

or deep wells (250–600 m) within the Miocene volcanic formations (Fig. 3a–c). In 2017, the water table was found at a depth between 62 and 80 m and parallel to the topography, with a single outlet at the north-eastern edge of the basin. The basin has a rectangular shape (Fig. 3a).

Within the basin, the orthogonal structural arrangement has defined rectangular-shape blocks with variable normal displacement (Dávalos-Álvarez et al. 2005). The fault system seems to have an important role in groundwater flow (Fig. 3a), resulting in the NW–SE faults being a preferential target for the drilling of wells. These faults, notably the San Fandila and Opalo fault systems (Fig. 3a), seem to act as groundwater flow channels. The structural control of groundwater flow is also illustrated by the historic piezometric records (Fig. 3b,d). From block to block, the piezometry evolves differently even within the graben sedimentary filling, which shows the *compartmentalized* nature of groundwater flow in this area (Fig. 3b–d; Billarent-Cedillo et al. 2021; Carucci et al. 2012; Dogramaci and Herczeg 2002; Hernández-Antonio et al. 2015; Morales et al. 2015; Murgulet et al. 2016). Due to the large groundwater extraction from this aquifer, the water

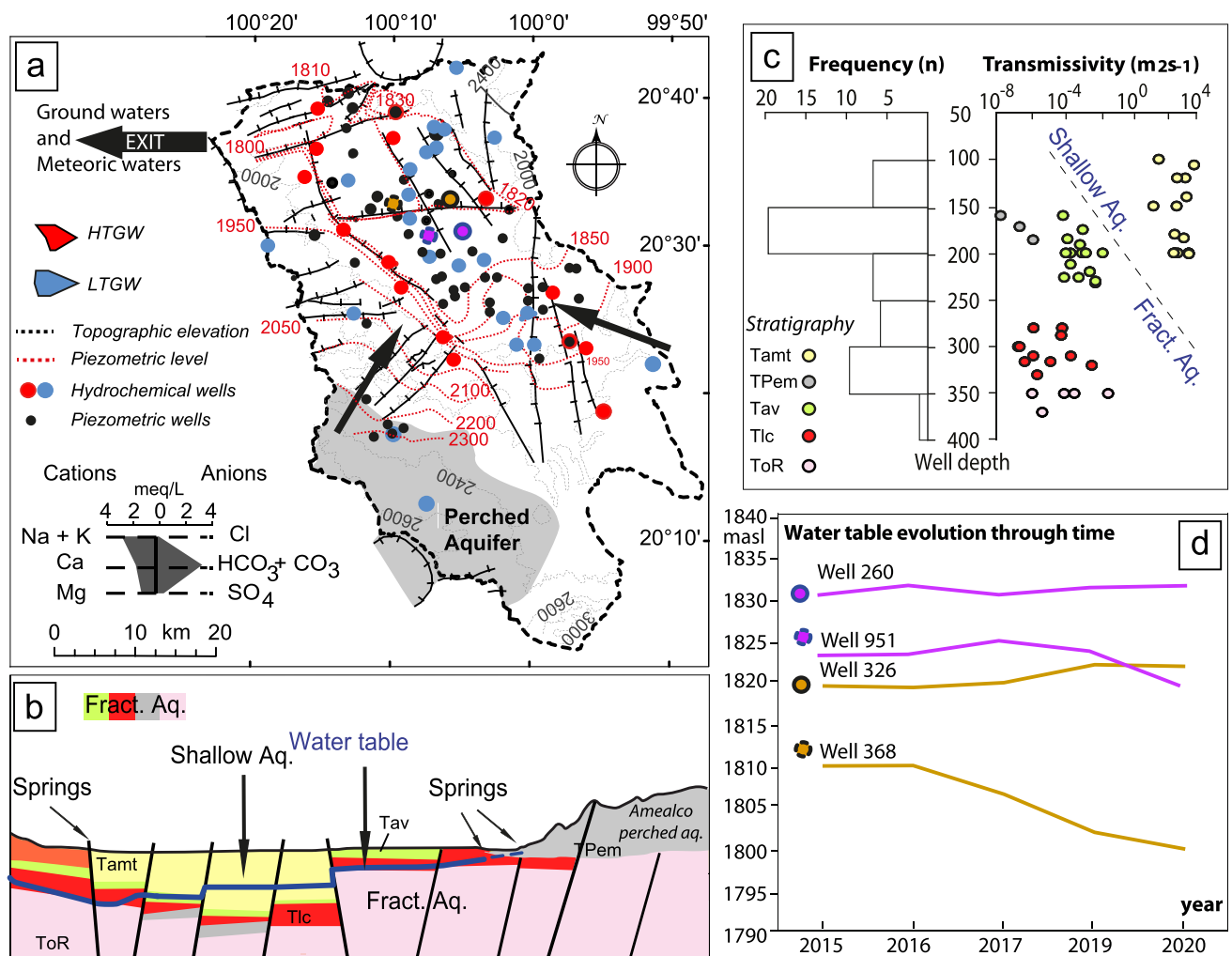


Fig. 3 **a** 2019 piezometric map of the SJR aquifer (red lines). Shaded area represents the Amealco perched aquifer extension. **b** N-S geological cross-section of the San Juan del Rio basin detailing the main lithological units and the water-table position for 2019. **c** Diagram of well depth versus calculated transmissivity and well depth histogram illustrating the existence of two aquifers. **d** Evolution of the water-

table has been descending up to 0.9 m year^{-1} on average since 1985.

Data from some pumping tests performed in the graben sedimentary filling and Miocene volcanic formations were reinterpreted in order to estimate the aquifer's hydraulic parameters (Fig. 3c). Rock transmissivity (T) was re-estimated with data from slug tests through the Cooper and Jacob (1946) method in 73 shallow and deep production wells. Transmissivity shows a variation of four orders of magnitude between the graben sedimentary filling ($10^0\text{--}10^2 \text{ m}^2 \text{ s}^{-1}$) and the Miocene volcanic ($10^{-2}\text{--}10^{-8} \text{ m}^2 \text{ s}^{-1}$) aquifers (Fig. 3c). This variability in transmissivity illustrates the inner geological heterogeneity of the aforementioned units. The graben sedimentary filling is formed by an alternation of clay and sand/conglomerate, while the Miocene

table elevation from 2015 to 2020 for wells 260, 326, 368 and 951, distributed in different structural blocks. LTGW: low-temperature groundwater; HTGW: high-temperature groundwater. Fract. Aq.: fractured aquifer; Shallow Aq.: shallow siliciclastic aquifer. Altitude and piezometric levels are given in masl. Stratigraphic unit abbreviations (m) are the same as for Fig. 2

volcanoclastic unit is a succession of sedimentary and volcanic flows. More importantly, the difference in transmissivity values observed between these two geologic units suggests that the basin is comprised by two main aquifers: (1) a *multicompartmentalized* shallow sedimentary aquifer in the valley with a maximum depth of 250 m, and (2) a Miocene sedimentary-volcanic fractured aquifer below the shallow aquifer (Fig. 3b,c).

Local meteorology

The local meteorology of the study area is detailed in Hernández-Pérez et al. (2020), from which it can be summarized that monthly relative air humidity ranges from 14 to 100%, although it is usually higher than 40% during the

wet season (June–September), while monthly mean temperature ranges from 14 °C in winter (dry period) to 20 °C in summer (wet period) with a mean of 17 °C. The yearly accumulated precipitation (1971–2000; Carrera-Hernández et al. 2016) varies from 400 to 850 mm year⁻¹, while potential evapotranspiration ranges from 500 to 800 mm year⁻¹. The yearly accumulated evaporation at the town of Amealco was recently determined, using both physical and isotopic methods, as 531.0 mm in 2016 and 768.6 mm in 2017 (Hernández-Pérez et al. 2020).

Materials and methods

To accomplish the objectives of this study, the precipitation during the period 2015 to 2017, the mineralogy of the aquifer formations, and the chemical and isotopic compositions of the groundwater and springs were characterized.

Water sampling and hydrochemistry

Fifty-three samples of groundwater were collected from wells ($n = 37$) and springs ($n = 16$) during the 2017 dry season for hydrochemistry and isotopic analysis (Figs. 1, 2 and 3). Twenty of them were selected for $\delta^{13}\text{C}$ and ^{14}C analysis to identify recharge processes and to determine radiocarbon ages. Groundwater samples were collected directly at the outlet of the well. Physical parameters such as electrical conductivity (EC), temperature (T), and pH were measured *in situ* using a Thermo-Orion Five Star Plus multiparameter. Total alkalinity was determined in the field using a HACH digital titrator. Samples for major element analysis were filtered through 0.45-μm cellulose acetate filter and were collected in polyethylene bottles, sealed and stored at 4 °C. Major anions were determined by high performance liquid chromatography (HPLC) using a Dionex chromatograph (LC20 with ASRS ultra 300 suppressor and ED50 detector), while major, minor, and trace metals were analyzed by a Thermo spectrometer ICP-OES (iCAP 6500 Duo) at Laboratorio de Geoquímica Ambiental del Centro de Geociencias, Universidad Nacional Autónoma de México (CGEO-UNAM). The quality of the undertaken chemical analysis was confirmed by calculating the ionic balance error. All samples have a charge balance error (CBE) lower than ±5%, thus indicating reliable data. (Table 1).

Isotopic ratios of $\delta^2\text{H}$ and $\delta^{18}\text{O}$ were analyzed with a Thermo Finnigan Delta Plus XL spectrometer at the LUGIS laboratory of the Instituto de Geología, UNAM. The methodology and normalization of the results were conducted according to Coplen (1988), and the isotopic ratios are expressed in δ-notation, relative to the Vienna Standard Mean Ocean Water (VSMOW) standard.

Carbon dating

The activity of ^{14}C and $\delta^{13}\text{C}_{(\text{TDIC})}$ isotopic ratios (DIC = dissolve inorganic carbon) were analyzed at Beta Analytics Laboratory in Miami, USA. The activity analysis of ^{14}C is determined by accelerator mass spectrometry (AMS) on graphite produced by hydrogen reduction of the CO_2 sample over a cobalt catalyst. The analytical result (“BP” or “pMC”) is obtained by measuring a sample $\text{C}^{14}/\text{C}^{13}$ relative to the $\text{C}^{14}/\text{C}^{13}$ in Oxalic Acid II (NIST-4990C). Using a Pal autosampler in conjunction with a Thermo Fisher GasBench 2.0, the headspace is sampled via a double-holed needle using a He stream to push the $\text{CO}_2 + \text{He}$ into the GasBench where any other gasses were separated out via a gas chromatography column. Detection of CO_2 was via gas chromatography (GC) with ISODAT control. Correction for drift was applied by normalizing the in-house standards to the expected values.

Both apparent and corrected radiocarbon ages are shown in Table 3. In order to have a better understanding of the geochemical processes of DIC evolution and its relationship with the decay of ^{14}C in the SJRB, the groundwater data were evaluated according to the graphical method as detailed by Han et al. (2012) (see electronic supplementary material: ESM1). The residence time of the DIC of the older groundwater end member was calculated from the corrected carbon activity ($\Delta^{14}\text{C}$) according to Han et al. (2012) and express as time before present (tBP):

$$t(\text{BP}) = \frac{t_{1/2}}{\ln 2} \ln \left(\frac{\text{C}^{14}}{\text{C}^{14}_0} \right) \quad (1)$$

Where C^{14} and C^{14}_0 are the measured and initial ^{14}C , $t_{1/2}$ is the half-life of ^{14}C and t is the groundwater age. The carbon correction and age calculation methodology and spreadsheet are given in ESM1 and ESM2. The correction models are based on the dispersion observed in the data.

Hierarchical clustering and principal component analysis (PCA)

All the physico-chemical data, including the regional geothermal springs (Los Geysers, Querétaro; González-Guzmán et al. 2019), were used to perform a hierarchical clustering to group and differentiate the types of the sampled waters. The results derived from the application of JMP® (Version 8.0. SAS Institute Inc.), are presented in Fig. 4a. Six main clusters were identified using a dissimilarity index of 7.0, which were selected based on the major Euclidean distance break in the amalgamation graph (Fig. 4a).

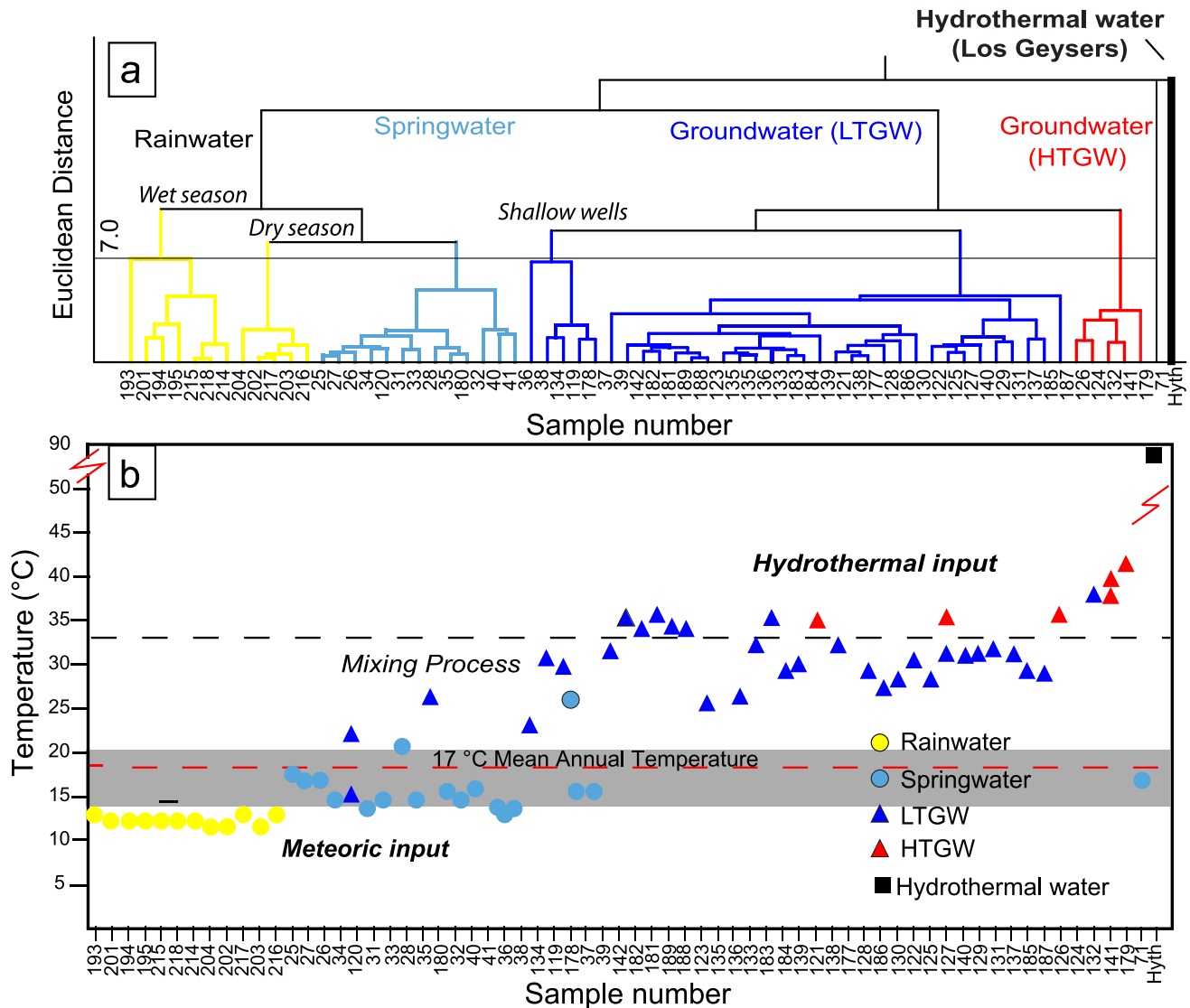
The mixing patterns in groundwater are calculated by a statistical mixing model using principal component

Table 1 Physical parameters of rain, spring and groundwater samples in the San Juan del Río Basin

Sample ID	Water type	Name	Date (dd/mm/yy)	UTM-WGS84-14N X (m) Y(m)	Depth (m, ref to z) Z (masl)	T (°C)	pH	EC (µS/cm)	TDS (mg/L)	ORP (mV)	Reference
193	Rainwater	COTAS, SJR	09/06/17	391242 2258787	1986	-	13.8	5.6	122.3	60.3	-163.5 Hernández-Pérez et al. 2020
201	Rainwater	COTAS, SJR	25/06/17	391242 2258787	1986	-	13.1	5.7	115.4	56.3	-125.7 Hernández-Pérez et al. 2020
204	Rainwater	COTAS, SJR	20/07/17	391242 2258787	1986	-	12.3	6.6	23.6	14.5	-182.7 Hernández-Pérez et al. 2020
215	Rainwater	COTAS, SJR	18/08/17	391242 2258787	1986	-	13.0	5.0	26.8	13.6	31.3 Hernández-Pérez et al. 2020
194	Rainwater	Amealco	18/06/17	378048 2233214	2612	-	13.1	6.4	75.0	34.7	-170.1 Hernández-Pérez et al. 2020
195	Rainwater	Colorado	18/06/17	370034 2274085	1937	-	13.1	7.1	265.2	128.4	-117.6 Hernández-Pérez et al. 2020
202	Rainwater	Amealco	11/07/17	378048 2233214	2612	-	12.3	5.6	25.5	13.2	-136.6 Hernández-Pérez et al. 2020
203	Rainwater	Colorado	20/07/17	370034 2274085	1937	-	12.3	5.2	33.2	16.8	-161.5 Hernández-Pérez et al. 2020
214	Rainwater	Amealco	18/08/17	378048 2233214	2612	-	13.0	6.1	18.1	9.4	55.8 Hernández-Pérez et al. 2020
216	Rainwater	Colorado	24/09/17	370034 2274085	1937	-	13.7	5.5	22.3	11.4	20.7 Hernández-Pérez et al. 2020
217	Rainwater	Amealco	24/09/17	378048 2233214	2612	-	13.7	5.6	17.5	9.1	33.5 Hernández-Pérez et al. 2020
218	Rainwater	Colorado	18/08/17	370034 2274085	1937	-	13.0	5.2	22.0	11.3	23.1 Hernández-Pérez et al. 2020
25	Spring water	El Millan	22/04/16	400060 2222746	2552	-	18.0	6.8	158.2	77.8	488.7 This study
26	Spring water	San Pablo 1	22/04/16	398664 2221199	2606	-	17.0	7.5	167.4	82.4	480.0 This study
27	Spring water	San Pablo 2	22/04/16	398959 2220592	2670	-	17.0	6.9	190.2	93.6	493.1 This study
28	Spring water	Baño Chico	22/04/16	396375 2224512	2385	-	21.0	7.7	299.0	147.1	481.0 This study
31	Spring water	Amealco 8	29/04/16	383218 2234561	2566	-	14.0	6.6	144.4	71.1	483.7 This study
32	Spring water	Amealco 10	29/04/16	378245 2231318	2696	-	16.0	6.4	338.0	166.3	516.4 This study
33	Spring water	El Milagro	29/04/16	374194 2239431	2494	-	15.0	6.4	153.0	75.3	508.0 This study
34	Spring water	La Piedad	30/04/16	395042 2222092	2473	-	15.0	6.8	233.0	114.6	494.0 This study
35	Spring water	Baño Grande	30/04/16	396043 2223496	2398	-	15.0	7.9	255.0	125.5	486.0 This study
36	Spring water	Agua Azul	01/05/16	374646 2278458	1910	-	14.0	7.7	1062.0	522.5	496.0 This study
37	Spring water	Los Cues	01/05/16	368135 2267098	1995	-	16.0	7.6	928.0	456.6	503.3 This study
38	Spring water	Los Sabinos	01/05/16	374806 2258344	2094	-	14.0	8.7	877.0	431.5	489.6 This study
39	Spring water	Escolásticas	01/05/16	373433 2259643	2098	-	16.0	8.5	444.0	218.5	489.9 This study
40	Spring water	El Jazmín	07/05/16	391899 2249920	2128	-	15.0	7.8	598.0	294.2	501.0 This study
41	Spring water	La Fuente	08/05/16	392098 2272817	1990	-	16.0	7.2	439.0	216.0	503.4 This study
71	Spring water	Palmas	14/05/16	386731 2288670	2096	-	24.0	7.4	1625.0	796.9	434.5 This study
122	GW I	La Lira	23/04/17	378711 2264660	1952	140	30.8	7.4	427.2	210.2	432.2 This study
123	GW I	San Fandila	23/04/17	373015 2268572	1953	179	34.1	7.7	344.9	169.4	441.9 This study
125	GW I	El Blanco 2	24/04/17	384692 2278860	1974	200	28.8	7.5	401.2	197.1	453.6 This study
127	GW I	El Tejocote	24/04/17	391855 2279980	2000	200	31.4	7.7	412.3	202.3	428.0 This study
129	GW I	La Fuente	24/04/17	390934 2272480	1978	141	31.6	7.8	382.2	187.8	434.2 This study
130	GW I	La Angola	24/04/17	385500 2280980	1983	200	28.7	7.5	263.9	130.1	449.3 This study

Table 1 (continued)

Sample ID	Water type	Name	Date (dd/mm/yy)	UTM-WGS84-14N X (m)	Y (m)	Z (masl) (m, ref to z)	Depth (°C)	T	pH	EC (µS/cm)	TDS (mg/L)	ORP (mV)	Reference
133	GW I	La Ponderosa	25/04/17	381193	2276180	1939	114	32.3	7.6	389.1	191.2	432.7	This study
134	GW I	San Cirilo	25/04/17	374513	2258297	2095	175	23.3	7.8	586.1	287.9	417.6	This study
135	GW I	El Sauz	25/04/17	383882	2264950	1953	196	26.2	7.8	335.2	164.7	417.6	This study
136	GW I	Chintepet	25/04/17	387411	2264430	1969	185	26.6	7.8	304.5	150.1	419.6	This study
137	GW I	Los Alvarez	25/04/17	381168	2272940	1938	90	31.6	8.1	462.0	226.9	410.4	This study
138	GW I	Quintanares	26/04/17	381177	2270040	1938	92	32.6	8.1	264.0	129.9	416.6	This study
139	GW I	Paraiso	26/04/17	373597	2274660	1910	150	30.4	8.0	399.1	196.1	437.2	This study
140	GW I	Zacatenco	26/04/17	370012	2283650	1902	170	31.4	8.0	475.0	233.2	430.6	This study
142	GW I	El Carmen	26/04/17	368129	2275387	1964	180	31.8	8.1	359.0	176.5	457.5	This study
177	GW I	Bethania 02A	23/05/17	396968	2254340	1945	283	36.1	7.9	319.6	157.1	473.6	This study
180	GW I	Quiotillos	23/05/17	378697	2243320	2296	260	26.2	7.7	262.6	131.3	260.7	This study
181	GW I	Cerrito	23/05/17	386731	2252500	2027	232	33.9	8.1	426.2	213.1	476.3	This study
182	GW I	Galindo/Arcila	23/05/17	385429	2255360	1987	175	35.4	8.2	381.1	190.6	368.2	This study
183	GW I	Arboledas	23/05/17	395971	2258500	1935	250	35.7	8.0	410.1	205.1	433.0	This study
184	GW I	Lourdes	24/05/17	390719	2264900	1977	146	29.4	7.9	444.0	222.0	462.0	This study
185	GW I	El Carrizo	24/05/17	394787	2254570	1994	80	29.7	7.8	654.7	327.4	520.6	This study
187	GW I	Pueblo Quieto	24/05/17	399139	2260880	1902	120	29.4	8.6	669.1	334.6	357.6	This study
189	GW I	Solares Bantii (IVEQRO)	24/05/17	402278	2254300	1988	150	36.0	8.1	362.3	178.1	364.3	This study
120	GW I	Amealco 1	23/04/17	382137	2234320	2562	150	22.1	7.5	157.0	77.5	474.2	This study
119	GW I	Cimatario 1	23/04/17	361360	2266720	2025	250	31.1	7.6	486.8	239.1	453.1	This study
128	GW I	La Esperanza	24/04/17	384508	2281190	1975	250	29.8	8.0	260.1	128.1	450.4	This study
131	GW I	Purisima de Cubos	24/04/17	383637	2278310	1968	146	31.7	7.7	346.5	170.2	436.7	This study
178	GW I	El Sitio	23/05/17	411530	2251960	2223	195	29.9	7.9	579.7	284.6	452.3	This study
186	GW I	Loma Linda	24/05/17	393128	2257690	1990	94	27.8	7.4	355.3	177.7	505.0	This study
188	GW I	Magisterial	24/05/17	401857	2255110	1982	224	34.1	8.2	387.4	193.7	333.8	This study
121	GW II	La D	23/04/17	380114	2261430	1977	174	35.2	7.6	282.7	138.8	432.9	This study
126	GW II	La Peñuela	24/04/17	379580	2283140	1977	242	36.1	7.9	288.1	141.8	449.0	This study
132	GW II	Galeras	25/04/17	379170	2279880	1912	300	37.9	7.7	300.2	147.6	418.1	This study
141	GW II	Coyne	26/04/17	369570	2278780	1899	250	38.1	8.1	395.0	193.9	466.8	This study
179	GW II	Puerta de Palmillas	23/05/17	405328	2245940	2230	350	41.5	9.1	549.7	274.9	398.5	This study
124	GW II	Palmas	24/04/17	386948	2288550	2095	350	32.9	7.8	223.3	110.0	422.2	This study
300	Hydrothermal	LG01						98.1	6.9	1,264	618		González-Guzmán et al. 2019
319	Hydrothermal	LG85						94.3	9.3	1,223	600		González-Guzmán et al. 2019



respective B and C coordinates (Laaksoharju et al. 1999). The estimated mixing proportions are presented in ESM3.

Results

Physicochemical parameters of the hydrological system.

Six physicochemical parameters (temperature, pH, electrical conductivity (EC), total dissolved solids (TDS), oxidation-reduction potential (ORP), as well as the isotope composition of water ($\delta^2\text{H}$ and $\delta^{18}\text{O}$) from rainwater and groundwater (springs and wells) are used to setup the geochemical signature of water throughout the water cycle in the SJRB. All measured parameters from collected samples are presented in Tables 1, 2 and 3 and Figs. 4, 5 and 6.

Figure 4a shows the water hierarchical clustering according to their physico-chemical and isotopic geochemistry. At a Euclidian distance of 7.0, the differentiated six groups are rainwater (wet and dry seasons), spring water, groundwater (low-temperature groundwater (LTGW) and including shallow wells), and hydrothermal water—Los Geysers, high-temperature groundwater (HTGW), Fig. 4b. The temperature shows three distribution trends with breaking points at 17 and ~ 34 °C (Fig. 4b). The low-temperature segment is composed of rainwater and spring water (13–17 °C). The rainwater samples (yellow dots) are monthly accumulation. Their temperature values are estimated from the mean atmospheric temperature during the precipitation period monitored (Fig. 4b). Spring water (blue dots in Fig. 4b) shows a limited variation (from 14 to 24 °C) with respect to the seasonal mean atmospheric temperature range (14–20 °C). Groundwater (LTGW and HTGW; $n = 47$) is the most representative group with temperatures ranging from 22.1–41.5 °C (blue and red triangles in Figs. 2a, 4a, 5, 6b and 7). All measured groundwater temperatures are above the seasonal mean air temperature in the SJRB (14–20 °C). Considering the Euclidian clustering, a group of six groundwater samples (red triangles) is differentiated by temperature (>34 °C) and chemistry. The aforementioned group was identified as high temperature groundwater (HTGW; Fig. 2a,b). Two geothermal wells from Los Geysers area (Querétaro basin) were added to the data set to present comparative geothermal behavior with respect to the local groundwater (Tables 1 and 2). Besides temperature clustering, each group shows particular physico-chemical behavior. In the SJR, rainwater samples have acidic to near neutral pH (5.0–7.1) and electrical conductivity (EC) ranging from 17.5 to 265.2 $\mu\text{S cm}^{-1}$. Springs and LTGW in the study area have a near-neutral pH (6.4–8.7), while HTGW tends to be slightly more alkaline (7.6–9.3). EC values range from 144 to 1625 $\mu\text{S cm}^{-1}$; the spring waters are characterized by low EC, ranging from 144

to 338 $\mu\text{S cm}^{-1}$. Regarding the EC in groundwater samples, the LTGW samples have an average of 397 $\mu\text{S cm}^{-1}$ while HTGW samples show an average of 339 $\mu\text{S cm}^{-1}$. All spring, LTGW and HTGW samples are in oxidizing conditions with positive ORP values ranging from 338 to 520 mV. Rainwater samples are distinguished by negative or low positive ORP values which indicate reductive conditions (−125 to 55 mV; Table 1).

All water samples are plotted on a Piper diagram (Fig. 5) to illustrate chemical differences and evolution patterns in the SJRB. Rainwater is dominated by calcium and bicarbonate with low and variable concentrations of Cl and SO_4^{2-} , while groundwater (springs, LTGW and HTGW) shows a continuous chemical evolution, from Ca–Na– HCO_3^- spring water to Na– HCO_3^- –(SO_4^{2-}) HTGW end-members facies (Fig. 5). The LTGW samples present a transitional chemical composition and connect the meteoric and HTGW end-member facies (Fig. 5). Both LTGW and HTGW show higher nitrate (NO_3^-) and sulfate (SO_4^{2-}) concentrations compared to meteoric water. LTGW and HTGW show nitrate concentrations up to 24.47 and 23.22 mg L^{−1} respectively. Sulphate concentrations in LTGW and HTGW range from 2.86 to 35.40 mg L^{−1} and 6.69 and 32.92 mg L^{−1} respectively. Compared to the SJRB groundwater, the Los Geysers geothermal end-member water is significantly enriched in chloride (<97.8 mg L^{−1}), sodium (<211 mg L^{−1}), sulphate (<45.9 mg L^{−1}) and fluoride (<27.8 mg L^{−1}), while depleted in calcium (<2.28 mg L^{−1}), magnesium (<0.15 mg L^{−1}) and nitrate (below detection limit).

Deuterium and oxygen stable isotopes

Detailed isotopic data of rainwater are reported in Hernández-Pérez et al. (2020). The isotopic composition of rainwater shows a wide range for $\delta^2\text{H}$, as it varies from 12.87 to −108.8‰ with a mean value of −65.6‰ (s.d. = 35.7‰), while $\delta^{18}\text{O}$ varies from 0.88 to −15.13‰ with a mean value of −9.5‰ (s.d. = 4.7‰), as shown in (Fig. 6a). The local meteoric water line (LMWL) equation for the SJRB was defined as $\delta^2\text{H} = 7.61 \times \delta^{18}\text{O} + 5.89$ (Fig. 6a,b; Hernández-Pérez et al. 2020).

The $\delta^2\text{H}$ – $\delta^{18}\text{O}$ results for both spring and groundwater samples are presented in Fig. 6a,b and Table 2. The isotopic composition of spring water is distributed along the LMWL (Fig. 6a). However, the high-altitude spring water from the southern mountains forms a tight group close to the rainwater average isotopic signature ($\delta^2\text{H} = -66.0\text{\textperthousand}$; $\delta^{18}\text{O} = -9.46\text{\textperthousand}$), while spring water samples from the valley and the northern basin present an isotopic depletion trend along the LMWL (Fig. 6a).

The isotopic composition of groundwater (LTGW and HTGW; Fig. 6b) ranges from −81.3 to −67.7‰ with a mean value of −74.4‰ (s.d. = 3.1‰) for $\delta^2\text{H}$ and from −11.26

Table 2 Chemical composition of rain, spring and groundwater samples in the San Juan del Río Basin. Elemental concentrations are given mg L⁻¹, δ²H and δ¹⁸O are given in ‰ relative to VSMOW

Sample ID	Ca ²⁺	Mg ²⁺	Na ⁺	K ⁺	HCO ₃ ⁻	F ⁻	Cl ⁻	NO ₃ ⁻	PO ₄ ³⁻	SO ₄ ²⁻	Ionic Balance (%)	δ ¹⁸ O _{VSMOW} (‰)	δ-excess	Reference	
193	7.9	0.34	0.39	0.62	1	0.16	1.01	5.69	0.00	14.42	1.36	12.87	0.88	5.82	Hernández-Pérez et al. 2020
201	7.2	0.88	1.90	0.98	20	0.00	1.65	0.00	0.00	7.78	-0.04	-45.48	-7.57	15.05	Hernández-Pérez et al. 2020
204	11.3	0.02	0.07	0.06	28	0.03	0.00	1.09	0.00	2.21	4.09	-41.65	-5.66	3.65	Hernández-Pérez et al. 2020
215	2.1	0.13	0.11	0.13	4	0.00	0.25	0.00	0.00	2.78	-3.27	-29.58	-4.84	9.14	Hernández-Pérez et al. 2020
194	6.1	0.29	0.28	0.31	12	0.00	0.54	2.93	0.00	5.28	-2.89	-100.40	-13.71	9.27	Hernández-Pérez et al. 2020
195	28.5	1.30	0.92	0.85	79	0.00	1.16	0.00	0.00	5.59	4.79	-99.62	-13.48	8.19	Hernández-Pérez et al. 2020
202	2.5	0.09	0.10	0.12	2	0.00	1.53	0.00	0.00	3.15	-2.32	-108.84	-15.13	12.23	Hernández-Pérez et al. 2020
203	2.5	0.16	0.15	0.11	6	0.00	0.00	0.00	0.00	2.27	0.49	-66.75	-10.11	14.12	Hernández-Pérez et al. 2020
214	1.0	0.11	0.04	0.03	2	0.00	0.00	0.76	0.00	0.94	-3.89	-62.05	-9.01	10.06	Hernández-Pérez et al. 2020
216	1.7	0.11	0.11	0.06	4	0.00	0.00	0.00	0.00	1.70	-1.34	-85.11	-12.49	14.77	Hernández-Pérez et al. 2020
217	0.8	0.07	0.04	0.03	1	0.00	0.00	0.00	0.00	1.06	-1.58	-96.64	-13.76	13.43	Hernández-Pérez et al. 2020
218	2.0	0.18	0.07	0.05	7	0.00	0.00	0.00	0.00	0.42	-1.89	-64.53	-9.37	10.46	Hernández-Pérez et al. 2020
25	8.72	2.65	6.315	3.35	56	0.05	1.78	0.90	0.00	1.08	0.28	-75.4	-11.4	16.1	This study
26	8.68	3.55	7.536	3.28	62	0.05	1.17	0.73	0.00	0.87	2.49	-75.2	-11.1	13.6	This study
27	10.70	3.91	7.517	3.06	68	0.05	1.41	0.43	0.00	0.97	3.12	-73.5	-10.9	13.7	This study
28	7.35	2.89	11.580	4.44	70	0.00	1.78	0.46	0.00	0.63	0.12	-68.7	-9.9	10.3	This study
31	6.77	1.69	7.742	5.30	56	0.00	2.09	0.99	0.00	3.28	-5.59	-67.0	-9.4	7.9	This study
32	17.57	4.22	15.100	5.54	74	0.00	10.22	26.26	0.00	14.14	-4.63	-63.6	-9.4	11.5	This study
33	5.88	1.84	10.600	2.39	42	0.00	3.62	10.69	0.61	1.05	-1.86	-72.6	-10.3	9.4	This study
34	11.25	5.24	8.516	6.36	78	0.00	1.32	4.19	0.00	1.17	4.02	-70.6	-10.3	11.9	This study
35	12.34	4.63	12.850	6.90	110	0.00	1.15	0.21	0.00	0.32	-3.16	-72.2	-10.7	13.5	This study
36	27.30	6.95	91.620	36.10	228	0.64	40.20	75.30	2.25	65.63	-4.96	-66.5	-9.4	8.6	This study
37	18.87	4.65	12.700	1.52	106	0.18	4.27	0.39	0.00	0.87	0.64	-69.3	-9.7	8.5	This study
38	33.30	16.49	44.310	14.00	275	0.38	7.01	31.06	0.00	9.99	-1.21	-65.9	-9.4	9.5	This study
39	18.93	7.32	32.890	6.62	172	0.14	2.32	1.19	0.00	6.40	1.66	-70.0	-10.4	13.3	This study
40	16.91	6.22	13.470	2.56	38	0.29	5.30	34.82	0.56	25.68	2.70	-74.9	-10.3	7.8	This study
41	14.28	4.51	27.370	14.87	54	0.21	13.63	50.04	0.00	30.15	-1.14	-80.2	-11.1	8.5	This study
71	68.15	17.23	136.90	56.12	168	0.19	136.60	97.00	0.52	243.20	-4.13	-72.1	-9.89	7.0	This study
122	24.36	5.03	44.87	17.36	194	0.36	2.79	8.68	0.00	26.76	0.63	-71.5	-9.5	4.5	This study
123	21.01	6.85	37.30	9.38	172	0.29	3.10	9.21	0.00	14.98	1.35	-73.2	-10	6.8	This study
125	24.97	4.78	44.89	16.46	195	0.72	4.34	19.06	0.00	16.88	-0.03	-73.9	-10.0	6.0	This study
127	25.30	7.31	42.21	15.25	193	0.79	5.27	21.48	0.00	16.75	0.51	-71.1	-9.4	4.1	This study
129	20.26	4.79	49.08	12.92	184	1.55	4.11	12.76	0.00	17.27	1.21	-72.5	-9.9	6.7	This study

Table 2 (continued)

Sample ID	Ca^{2+}	Mg^{2+}	Na^+	K^+	HCO_3^-	F^-	Cl^-	NO_3^-	PO_4^{3-}	SO_4^{2-}	Ionic Balance (%)	$\delta^{2\text{H}}_{\text{VSMOW}}$ (‰)	$\delta^{18\text{O}}_{\text{VSMOW}}$ (‰)	δ -excess	Reference
	(mg/L)	(mg/L)	(mg/L)	(mg/L)	(mg/L)	(mg/L)	(mg/L)	(mg/L)	(mg/L)	(mg/L)	(%)				
130	13.68	3.73	28.47	11.34	102	1.29	3.82	9.43	0.00	21.26	1.54	-77.2	-10.6	7.8	This study
133	25.29	5.38	42.15	11.14	166	0.37	5.68	14.77	0.00	21.98	3.05	-73.9	-10.0	6.2	This study
134	42.62	18.38	43.81	14.69	284	0.35	2.64	24.47	0.00	17.30	3.66	-71.8	-9.6	5.1	This study
135	26.13	6.00	30.50	8.20	166	0.26	3.73	13.01	0.00	8.23	1.73	-71.3	-9.5	4.7	This study
136	21.79	5.60	29.29	9.29	170	0.27	2.31	9.30	0.00	4.73	-0.88	-74.0	-9.9	5.2	This study
137	33.31	7.09	43.94	11.32	212	0.08	7.19	4.80	0.00	23.19	2.35	-73.9	-10.1	6.7	This study
138	16.37	3.32	29.88	8.24	130	0.30	4.81	7.39	0.00	11.88	-0.91	-75.1	-10.2	6.5	This study
139	24.55	4.86	44.50	11.95	136	0.39	26.40	8.53	0.00	28.31	1.88	-73.3	-10	6.7	This study
140	23.71	5.86	62.99	12.73	216	0.62	9.32	16.51	1.00	16.84	2.68	-73.3	-9.8	5.1	This study
142	19.72	5.70	41.77	10.12	156	0.43	8.97	10.78	0.00	21.70	1.01	-73.1	-10.0	6.9	This study
177	15.5	3.42	26.84	6.61	122	0.22	2.84	4.75	0.00	7.25	1.58	-75.3	-10.4	7.9	This study
180	11.0	4.78	19.36	6.46	108	0.28	1.94	0.69	0.00	4.95	-0.29	-71.4	-10.2	10.2	This study
181	15.0	7.02	36.89	10.5	164	0.25	2.29	7.33	0.00	10.93	1.41	-75.5	-10.2	5.8	This study
182	16.4	4.83	32.63	8.82	132	0.21	8.35	5.60	0.00	12.04	1.90	-72.2	-9.8	6.2	This study
183	22.2	4.94	30.79	8.52	146	0.19	6.42	18.02	0.00	9.95	-0.19	-73.8	-10.2	7.5	This study
184	21.7	5.03	35.70	10.4	164	0.26	3.90	15.17	0.00	7.20	1.63	-73.1	-9.8	5.6	This study
185	37.9	9.10	40.37	12.3	172	0.19	22.43	19.95	0.00	35.40	2.06	-71.8	-9.7	5.8	This study
187	15.6	3.59	82.82	10.8	164	0.23	58.16	14.74	0.00	8.67	1.97	-76.2	-10.3	6.4	This study
189	14.1	5.19	34.05	7.49	156	0.33	2.43	6.02	0.00	6.13	-1.24	-76.9	-10.5	7.0	This study
120	11.25	5.09	8.74	4.30	75	0.00	1.80	9.36	0.00	2.86	-0.69	-77.9	-10.5	6.1	This study
119	28.10	16.75	50.67	9.12	282	0.34	2.82	11.64	0.00	15.80	-0.17	-77.94	-10.24	4.01	This study
128	17.58	3.98	25.06	11.54	132	0.64	2.68	11.39	0.00	10.28	-1.54	-80.9	-11.3	9.2	This study
131	20.68	4.69	41.82	9.69	162	0.77	4.03	10.76	0.00	15.89	2.51	-67.7	-8.16	-2.5	This study
178	20.3	17.01	35.45	16.3	218	0.71	5.53	17.44	0.00	7.23	1.93	-81.3	-10.8	5.1	This study
186	18.8	6.87	20.44	9.75	128	0.09	2.90	17.63	0.00	6.20	0.84	-79.8	-10.9	7.4	This study
188	14.9	5.43	38.37	8.84	168	0.40	2.65	6.79	0.00	5.24	0.25	-77.5	-10.4	6.1	This study
121	17.11	4.18	32.25	8.77	150	0.20	2.18	6.77	0.00	6.72	0.81	-74.8	-10.1	6.0	This study
126	12.33	0.16	50.11	0.90	105	3.15	5.93	3.43	0.00	32.49	0.81	-73.0	-10.1	7.8	This study
132	4.15	0.59	59.82	0.91	112	1.74	7.86	6.52	0.00	23.85	2.32	-71.1	-9.8	7.2	This study
141	6.28	1.32	75.15	1.81	136	2.01	15.27	23.22	0.00	32.92	-1.16	-70.7	-9.6	6.1	This study
179	1.7	0.59	97.69	1.15	222	3.25	9.58	0.31	0.00	16.51	-0.23	-73.2	-10.1	7.6	This study
124	13.99	1.57	27.76	5.82	98	2.76	5.08	5.96	0.00	6.69	1.23	-80.4	-11.1	8.0	This study
300	2.28	0.07	211	8.25	274	22.6	91.6	0	0	41.4	3.12	-74.8	-9.7	2.8	González-Guzmán et al. 2019
319	1.81	0.15	176	9.57	103	27.8	97.8	0	0	45.9	3.12	-73.8	-9.4	1.4	González-Guzmán et al. 2019

Table 3 Carbon isotope data and radiocarbon residence time ($\Delta^{14}\text{C}$) for the Mook (1972, 1976), Pearson (1970) and Fontes and Garnier (1979) models. SI_{calcite} saturation index of calcite; $\delta^{13}\text{C}_{\text{VPDB}}$; $\Delta^{14}\text{C}$ $\Delta^{14}\text{C}$ activity (% pMC); $SD(\Delta^{14}\text{C})$ standard deviation of ^{14}C activity (% pMC); D/C dissolved inorganic carbon; $\Delta^{14}\text{C}$ correction models following the equation of Mook et al. 1972 (MOOK); Pearson et al. 1970 (PEARSON) and Fontes and Garnier 1979 (F&G); Residence times are estimated from different equations of apparent radio carbon age (AppR-CAge), Mook et al. 1972 (MOOK); Pearson et al. 1970 (PEARSON) and Fontes and Garnier 1979 (F&G)

Sample ID	Name	Water type	SI_{calcite}	$\delta^{13}\text{C}_{\text{VPDB}}$	$\Delta^{14}\text{C}$	$SD(\Delta^{14}\text{C})$	DIC	$\Delta^{14}\text{C}$ correction models			Residence Times			
								MOOK	PEARSON	F&G	AppRCAGe	MOOK	PEARSON	F&G
122	La Lira	LTGW	-0.19	-9.10	49.0	0.20	0.0133	21.5	39.6	37.1	5,897	-	7,649	8,191
123	San Fandila	LTGW	0.06	-10.10	64.3	0.20	0.0052	31.0	43.2	40.8	3,651	-	6,936	7,410
127	El Tejocote	LTGW	0.13	-10.20	63.6	0.20	0.0058	30.9	43.6	41.3	3,741	-	6,868	7,319
129	La Fuente	LTGW	0.12	-11.00	61.5	0.20	0.0052	37.5	46.4	44.3	4,019	-	6,343	6,736
135	El Sauz	LTGW	0.12	-10.50	80.0	0.30	0.0054	31.6	44.6	42.5	1,845	-	6,667	7,074
136	Chintepet	LTGW	0.06	-12.40	66.8	0.20	0.0060	48.9	51.4	49.5	3,335	-	5,497	5,808
138	Quintanares	LTGW	0.22	-12.80	53.7	0.20	0.0059	52.3	52.9	51.1	5,140	-	5,271	5,553
139	Paraiso	LTGW	0.25	-9.60	72.1	0.30	0.0077	25.5	41.4	39.0	2,704	-	7,285	7,779
140	Zacatenco	LTGW	0.43	-9.90	82.1	0.30	0.0074	28.4	42.5	40.1	1,630	-	7,073	7,549
177	Bethania 02A	LTGW	0.04	-12.40	54.2	0.20	0.0046	49.2	51.4	49.6	5,063	-	5,497	5,799
180	Quiotillos	LTGW	-0.50	-16.90	51.7	0.20	0.0082	89.7	67.5	66.2	5,454	902	-	-
182	Galindo/Arcila	LTGW	0.36	-11.10	82.8	0.30	0.0093	39.1	46.8	44.6	1,560	-	6,279	6,675
185	El Carrizo	LTGW	0.31	-11.00	81.5	0.30	0.0076	37.1	46.4	44.3	1,691	-	6,343	6,731
120	Amealco 1	LTGW	-0.90	-15.70	70.2	0.30	0.0058	81.1	63.2	61.5	2,925	1,730	-	-
178	El Sitio	LTGW	0.25	-8.30	82.5	0.30	0.0046	14.3	36.8	34.2	1,590	-	8,267	8,879
188	Magisterial	LTGW	0.39	-10.80	75.8	0.30	0.0060	36.5	45.7	43.5	2,290	-	6,471	6,886
121	La D	HTGW	-0.15	-11.50	62.3	0.20	0.0067	42.2	48.2	46.1	3,912	-	6,031	6,395
126	La Peñuela	HTGW	-0.14	-11.90	24.9	0.10	0.0095	45.4	49.6	47.7	11,493	-	5,789	6,125
141	Coyme	HTGW	-0.13	-12.90	40.0	0.10	0.0074	52.9	53.2	51.5	7,575	-	5,215	5,481
179	Puerta de Palmillas	HTGW	0.35	-10.50	13.0	0.10	0.0045	35.9	44.6	42.2	16,866	-	6,667	7,137

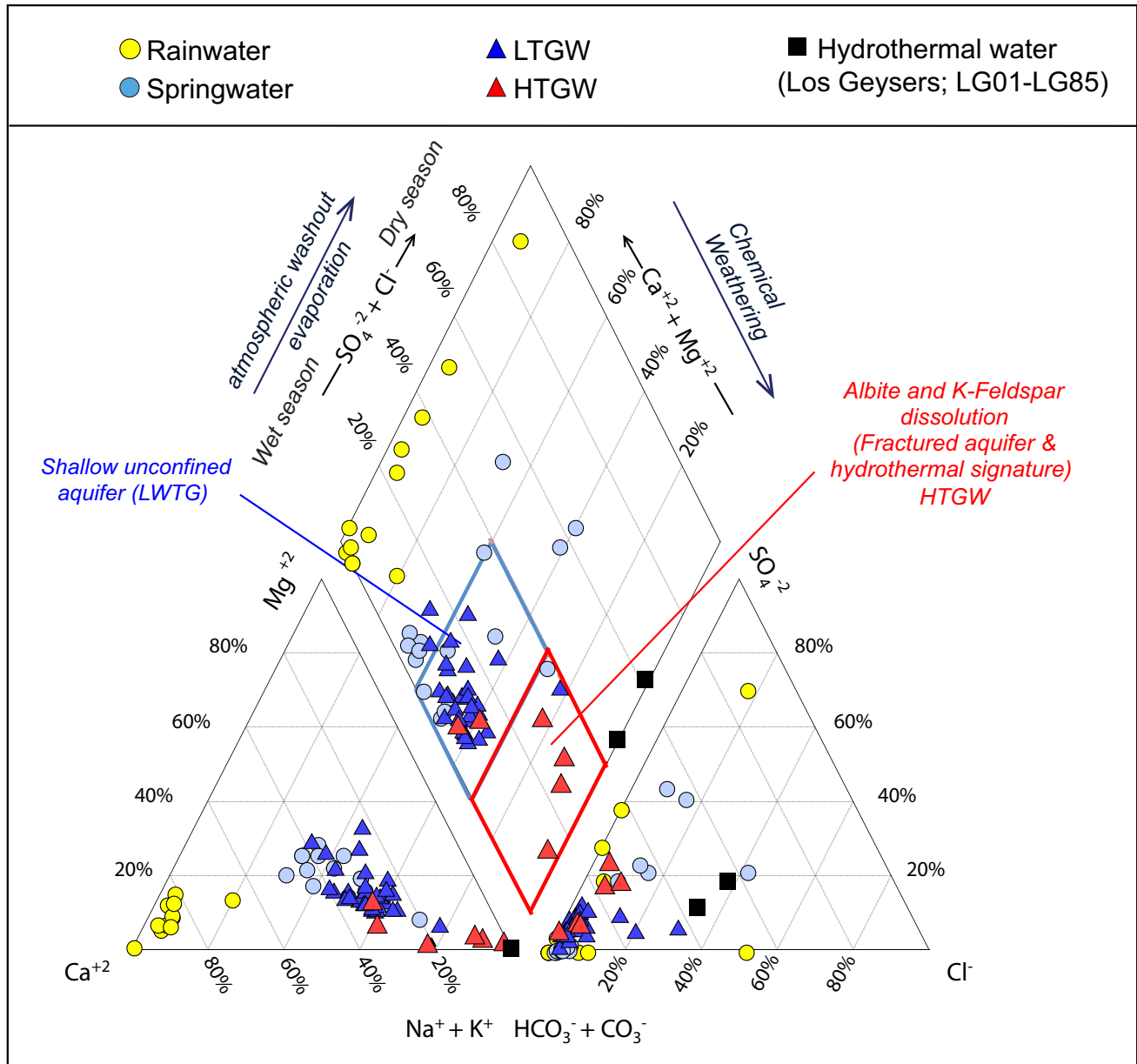


Fig. 5 Piper diagram of the water samples from the San Juan del Río Basin grouped by type. Differentiation of LTGW and HTGW is based on temperature and geochemical composition and hydrothermal mix-

ing with hydrothermal water. For comparison, the chemical data of regional hydrothermal springs and rainwater were added (Los Geysers, González-Guzmán et al. 2019; Hernandez-Perez et al. 2020)

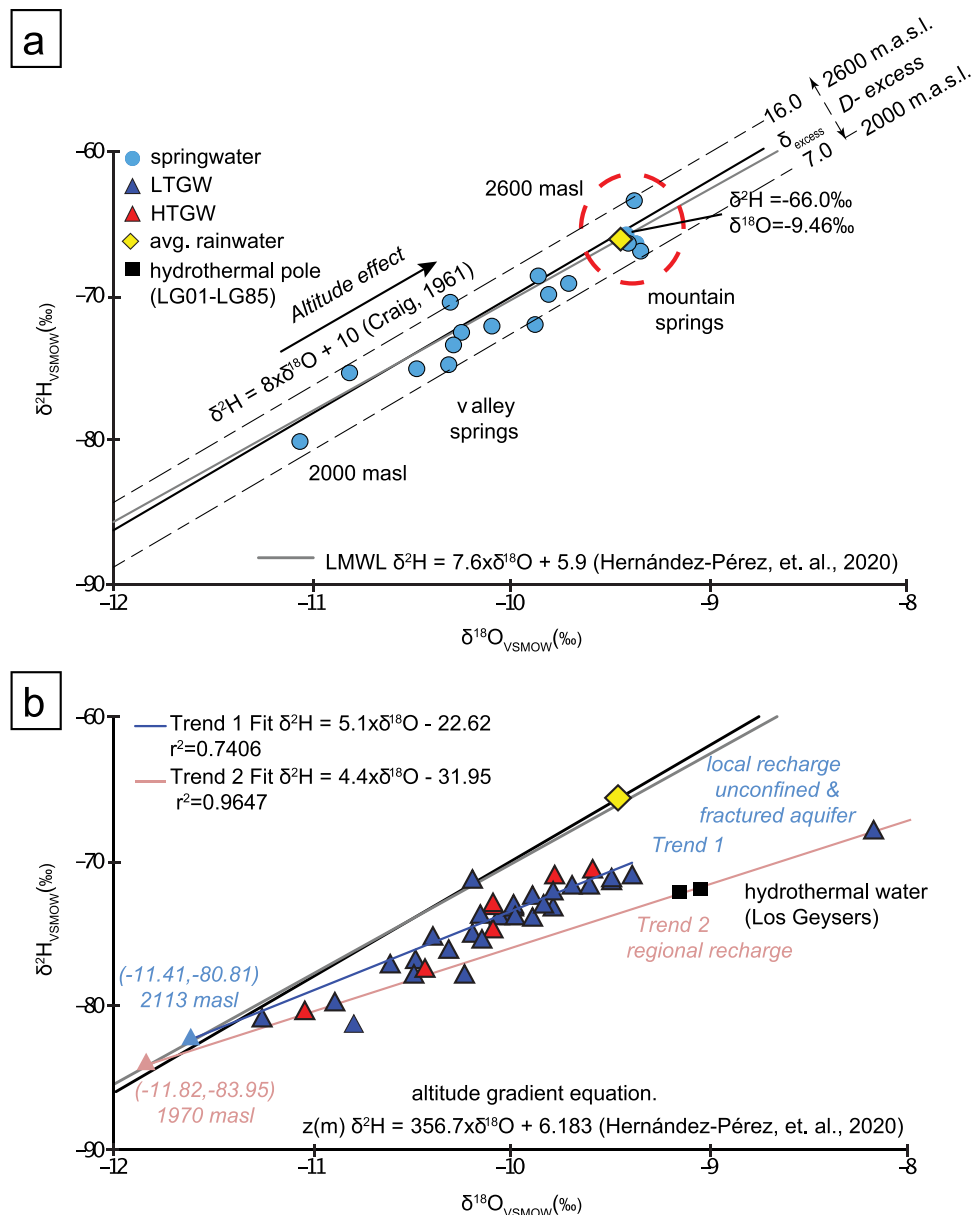
to $-8.16\text{\textperthousand}$ with a mean value of $-10.07\text{\textperthousand}$ ($s.d. = 0.5\text{\textperthousand}$) for $\delta^{18}\text{O}$ and a deuterium excess ranging from -2.4 to 10.2 (Table 2). In the $\delta^2\text{H}$ – $\delta^{18}\text{O}$ diagram, both LTGW and HTGW are dispersed without showing a clear correlation between the hierarchical clustering differentiation and the isotopic trends (Fig. 6b).

$\delta^{13}\text{C}$, ^{14}C and carbon geochemical data and ages

$\delta^{13}\text{C}_{(\text{TDIC})}$ and activity of ^{14}C of groundwater are presented in Table 3 and Fig. 7. $\delta^{13}\text{C}$ values for the LTGW ($n = 16$

range from -16.9 to $-8.3\text{\textperthousand}$, showing a greater dispersion in contrast with HTGW ($n = 4$) ranging from -10.5 to $-12.9\text{\textperthousand}$. Two data outliers (-16.9 and $-15.4\text{\textperthousand}$) within the LTGW group can be observed; these outliers are samples from wells in the Amealco volcanic caldera area, in the south of SJRB (wells 120 and 180 within the perched aquifer; Figs. 3 and 7). Activities of ^{14}C in LTGW range from 49.0 to 82.8 pMC, while HTGW exhibit activities from 13.0 to 62.30 pMC (Table 3). Dissolved inorganic carbon concentrations ranged from 1.23 to 3.56 mmol/L, with lower concentrations in the wells from Amealco volcanic caldera aquifer

Fig. 6 **a** $\delta^2\text{H}$ - $\delta^{18}\text{O}$ isotopic data for spring water samples from San Juan del Río Basin, showing isotopic depletion as an altitude effect. Red circle identifies the spring waters with the highest altitude. **b** $\delta^2\text{H}$ - $\delta^{18}\text{O}$ isotopic data of groundwaters (LTGW and HTGW) samples from the San Juan del Río Basin showing two main isotopic trends with a common meteoric origin but different recharge source. For comparison the isotopic data of regional hydrothermal springs mean local rainwater, and local and world meteoric line were added (Los Geysers, González-Guzmán et al. 2019; Hernandez-Perez et al. 2020; world meteoric line; Craig 1961)



area (1.23 and 1.77 mmol/L) compared to the LTGW (up to 3.57 mmol/kg). All samples have neutral to alkaline pH and are unsaturated or in equilibrium with respect to calcite (Fig. 7a,c; Tables 1 and 2).

According to Fig. 7, groundwater can be classified into three groups: (1) the perched aquifer with the Amealco and Quiotillos wells plotting in the ^{14}C -soil-controlled region, (2) the hydrothermal old waters from Puerta de Palmilla, Coyome and Peñuela deep wells, and (3) the rest of the groundwater samples located within the region controlled by mineral processes, and/or in the rock-interaction controlled area (Fig. 7a–c). In the Amealco and Quiotillos wells, the carbon source is solely from atmospheric and soil-controlled reservoirs. For these two wells, Mook's model provides a reliable carbon residence time (Fig. 8; Han and Plummer

2013). The old water wells and the main sample group chemistry are controlled by water–rock interaction, where the most reliable correction models will be the Pearson and the Fontes and Garnier models (Fig. 8; Han et al. 2012).

The corrected residence times of the SJRB groundwater are shown in Table 3 and are calculated with the Mook correction model for the perched aquifer, yielding ages from 902 to 1,730 years. The corrected residence times for the SJRB valley groundwater (LTGW and HTGW) are calculated with the Pearson and the Fontes and Garnier correction model equations. The estimated ages are comparable within the error margin (± 50 years) and range, from 5,215 to 8,267 years and 5,480–8,878 years, respectively. Residence times obtained from the perched aquifer (902 and 1,730 years) are at least 4,000 years less than those from the valley aquifers.

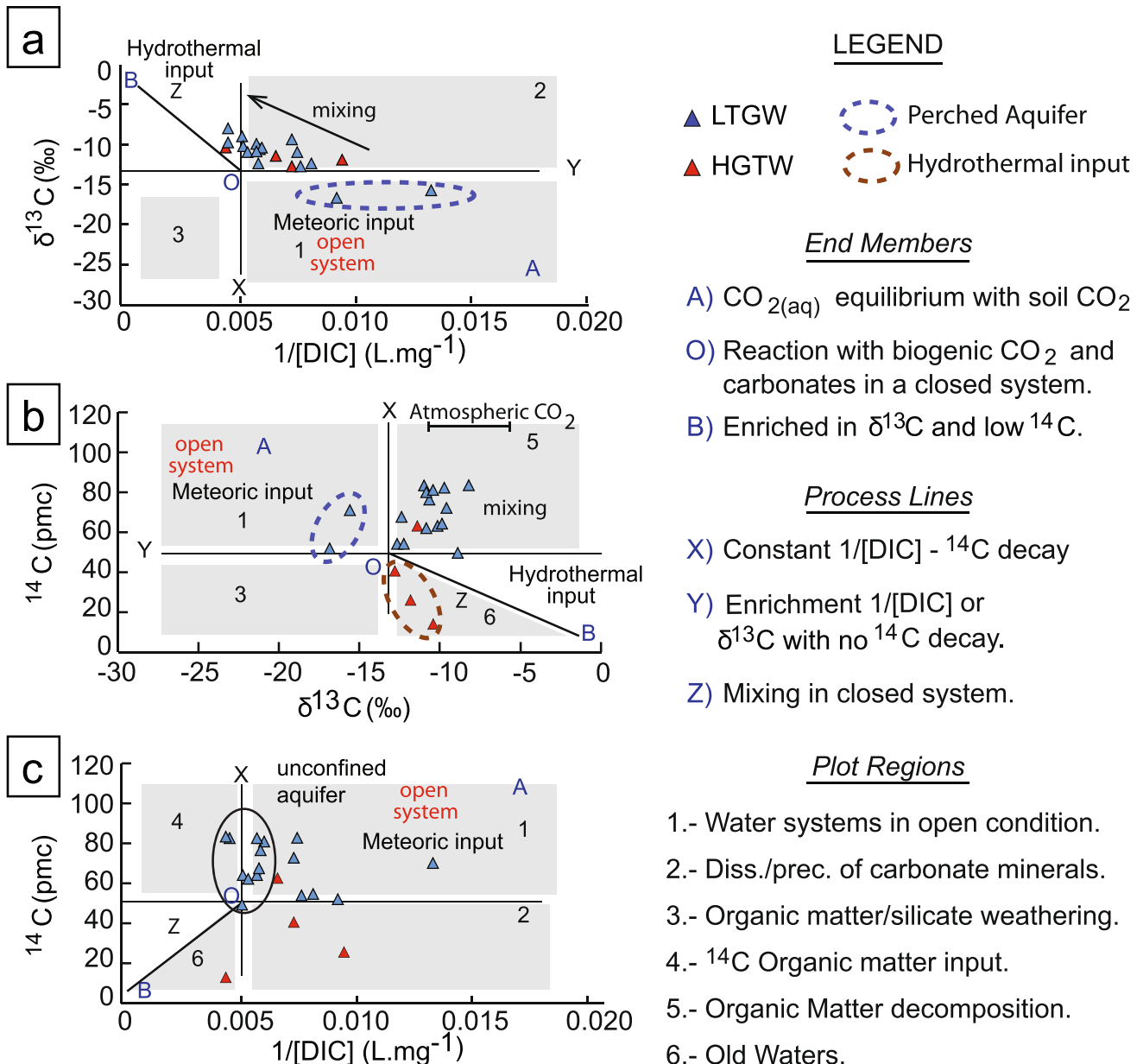


Fig. 7 Graphs for $^{14}\text{C} - \delta^{13}\text{C} - 1/\text{DIC}$ for groundwater data in the SJRB. Groundwater data are arranged by groundwater type. These distributions plot the regions (1–6) and carbon processes associated with the SJR aquifer. **a** Recent recharge is outlined for water systems in an open-condition region, arrow denotes the mixing between the meteoric and the hydrothermal reservoirs; **b** Data arrange in three groups. The influence of meteoric and hydrothermal end-members (EM) can be observed by samples plotting in the “water systems in

open conditions” (area 1) and “old waters” plot regions (area 6); mixing between reservoirs. The presence of a perched aquifer is inferred by the samples plotting region 1. **c** graph of the ^{14}C activity decay versus DIC showing contribution of carbon to groundwater by meteoric input or geochemical weathering. Data arranged inside the black circle correspond to groundwater storage in the shallow aquifer with low meteoric or hydrothermal input. For detailed information refer to ESM1

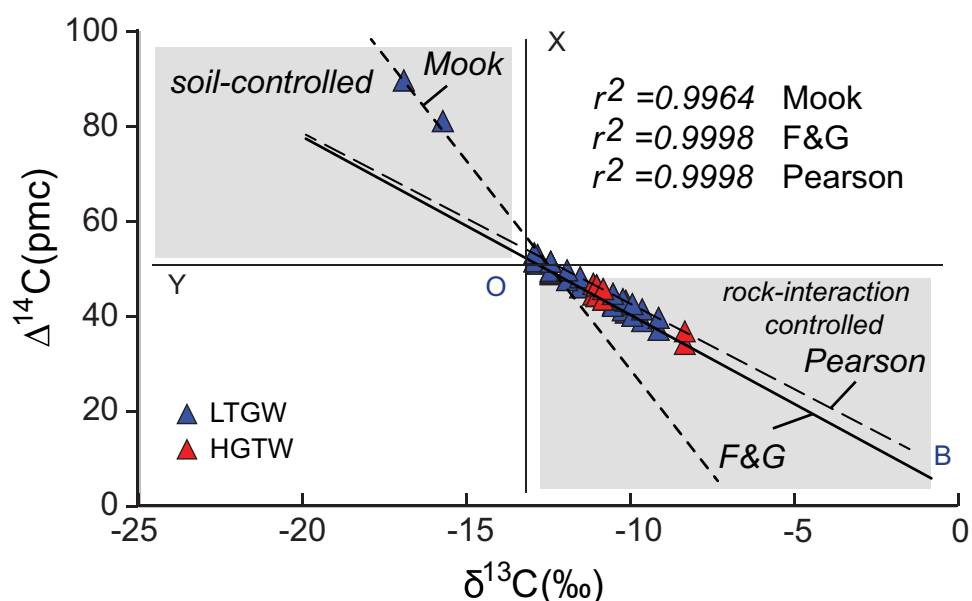
Discussion

Physico-chemical characterization of groundwater

The chemistry in rainwater shows an important variation that allows one to differentiate two subclusters or families in the hierarchical diagram (Fig. 4), which is related to seasonal

atmospheric physicochemical conditions (dry and wet season). The wind deflation process in semiarid environments increases the content of atmospheric aerosol particles during the dry season (Huang et al. 1955) and the first rains occur in an anomalously loaded atmosphere with aerosol (Hegg et al. 2011; Chowdhury et al. 2016; Sow and Lemaitre 2016). The chemical elements detected in the SJRB rainwater are

Fig. 8 $\Delta^{14}\text{C}$ vs. $\delta^{13}\text{C}$ diagram of the radiocarbon correction models. The correction models represented are from Mook (1972, 1976), Pearson (1970) and Fontes and Garnier (1979). For detailed data see ESM1.



chloride, fluoride and sulfates, which are attributed to the washout of atmospheric aerosols and dissolution of atmospheric gases during precipitation (Chowdhury et al. 2016). However, fluoride is not commonly observed in rainwater, and F-rich rocks (particularly local, outcropping ignimbrites) are the only source that can contribute to atmospheric aerosols in the SJRB.

The Piper and Euclidian clustering diagrams illustrate the statistical differentiation and chemical evolution of the groundwater subgroups. This differentiation is related to the temperature, chemistry and geological environment variation of the sampling source (springs versus shallow and deep wells). In field approximation, temperature is the most direct variable to distinguish groups of groundwater. However, in Euclidian clustering diagrams, the most important variables are the major elements of chemistry ($\text{Ca}-\text{Na}-\text{HCO}_3$). Within the spring water cluster, two different subfamilies can be observed. The most represented group has a $\text{Ca}-\text{Na}-\text{HCO}_3$ chemical type, which is comparable to the LTGW, illustrating a common source and water–rock interaction behavior. A group of a few springs located in the valley shows enrichment in $\text{Cl}-\text{NO}_3^--\text{SO}_4^{2-}$ concentration, which can be explained by the fact that they are located near farming areas and thus show fast recharge and contamination by irrigation return flows.

The geographic distribution of groundwater types by well sampling in the SJRB indicates that LTGW are dispersed throughout the basin and that the HTGW are structurally controlled by the N–S fault system (Fig. 3a). The shallow LTGW production wells in the agricultural areas of the valley show the largest concentrations of NO_3 and SO_4 , which are related to agricultural activities and leaching of organic matter and fertilizers (Power and Schepers 1989; Vitória

et al. 2008). Another potential source of NO_3 and SO_4 that cannot be ruled out is runoff and percolation of meteoric water from the Amazcala and Amealco sierras.

The $\text{Ca}^{2+}-\text{Mg}^{2+}/\text{Na}^+-\text{K}^+$ ion exchange observed in the Piper diagram (Fig. 5) illustrates the intensity/temperature ratio of chemical weathering of the rock substrate during the water–rock interaction process within the shallow granular and the volcanic deep aquifers. At the same time, the HTGW shows an enrichment in the Na^+-K^+ proportions, illustrating the mixing processes between both the shallow granular and the fractured aquifers.

The HTGW group is differentiated by temperature range (up to 41 °C), hydrogeochemical facies ($\text{Na}^+-\text{K}^+-\text{HCO}_3^--\text{SO}_4^{2-}$) and fluoride content (Figs. 4 and 5), suggesting the dissolution of albite and K-feldspar minerals in the rhyolites and ignimbrites from both the Oligocene and Miocene. Water–rock interaction and F-origin is in agreement with previously reported work in regional rhyolitic rocks and volcanic ashes emplaced between the Oligocene to Miocene in central and northern Mexico (Carrillo-Rivera et al. 2002; Valenzuela-Vásquez et al. 2006; Sanchez et al. 2018; Armienta and Segovia 2008; Mahlknecht et al. 2008; among others). This preliminary hydrogeochemical evolution of groundwater confirms that three main sources contribute to recharge, as defined by PCA endmembers: (1) local meteoric water, (2) groundwater contained in the granular aquifer reservoir and (3) hydrothermal groundwater flow. Along with the general mixing process, several geochemical interactions can be observed within the SJR aquifer. In the valley area, irrigation return flow from agricultural areas with organic matter and lixiviation of fertilizers takes place in the LTGW shallow aquifer. The data also show water–rock interactions as well as mixing with mountain–front recharge.

Through the N–S fault system, shallow groundwater interacts with deeper thermal water that also interacts with volcanic rocks, which causes increased mineralization and higher temperatures (Figs. 3 and 5).

Isotope hydrology

The isotopic composition of spring water is distributed along the LMWL. The depletion trend along the LMWL and the range of the deuterium excess (7–16) shows a good correlation with an altitude effect, confirming a local meteoric origin without significant evaporation (Fig. 6a; Ambach et al. 2012; Dansgaard 1964). The deuterium excess values also suggest precipitation with a different origin, i.e., from rainstorms coming from the Mexican Gulf and Pacific Ocean regions (Hernández-Pérez et al. 2020). The average rainfall is at the heavy end of the spring water range, confirming that chemical rock weathering during percolation and runoff is not intense enough to affect the initial meteoric isotopic signature.

The LTGW and HTGW show heavier values in $\delta^2\text{H}$ and $\delta^{18}\text{O}$ than rainwater, with values plotting along a local evaporation line (LEL). This variation could be related to time/temporal issues, as there is comparison between present and past atmospheric conditions. If atmospheric conditions were comparable between those of today and the oldest residence time estimated (9,000 years), the main area of aquifer recharge would be at low altitude (below 2,100 masl), which corresponds to the San Juan del Rio valley. LTGW and HTGW isotopic signature variation can be attributed to enrichment by evaporation, water–rock interaction or hydrothermal mixing. Generally, groundwater isotopic data are distributed slightly lower and parallel to the LMWL. In the SJRB, the local meteoric runoff flows from the volcanic sierras towards the valley floor and is stored in regulation dams. The semiarid atmospheric conditions that contribute to the evaporation process associated with the runoff and the storage of water in dams prior to infiltration modify the isotopic composition and rainwater signature that is transmitted to the groundwater during recharge (Hernández-Pérez et al. 2020).

The groundwater isotopic data show two groups of samples with different trends. These trends are distinguished according to the depth of the sampling well (up to 250 m). The first group is composed by most of the LTGW and HTGW groundwater samples. They appear just below the spring water family (Fig. 6b) and adjust to a fitting equation calculated as $\delta^2\text{H} = 5.1 \times \delta^{18}\text{O} - 22.6$ (trend 1), which intersects the LMWL at $\delta^2\text{H} = -80.8\text{\textperthousand}$ and $\delta^{18}\text{O} = -11.4\text{\textperthousand}$, illustrating the initial isotopic composition of rainwater prior to recharge (Fig. 6b).

The second trend line regroups the LTGW and HTGW outliers from wells deeper than 250 m and Los Geysers

hydrothermal waters (Fig. 6b; González-Guzmán et al. 2019). The trend 2 fitting equation is calculated as $\delta^2\text{H} = 4.4 \times \delta^{18}\text{O} - 31.91$ and intersects the LMWL at $\delta^2\text{H} = -83.9$ and $\delta^{18}\text{O} = -11.8\text{\textperthousand}$. Following the altitude isotopic effect equation (Hernández-Pérez et al. 2020), this second trend presents a lower infiltration altitude (1,970 masl) compared to the main trend (2,113 masl); both are related to the local topography. The displacement of $\delta^{18}\text{O}$ in the deep wells, displayed in trend 2, could be related to water–rock isotopic enrichment, or different mixing proportions of geothermal and meteoric waters (Giggenbach and Lyon 1977; Herrera and Custodio 2003).

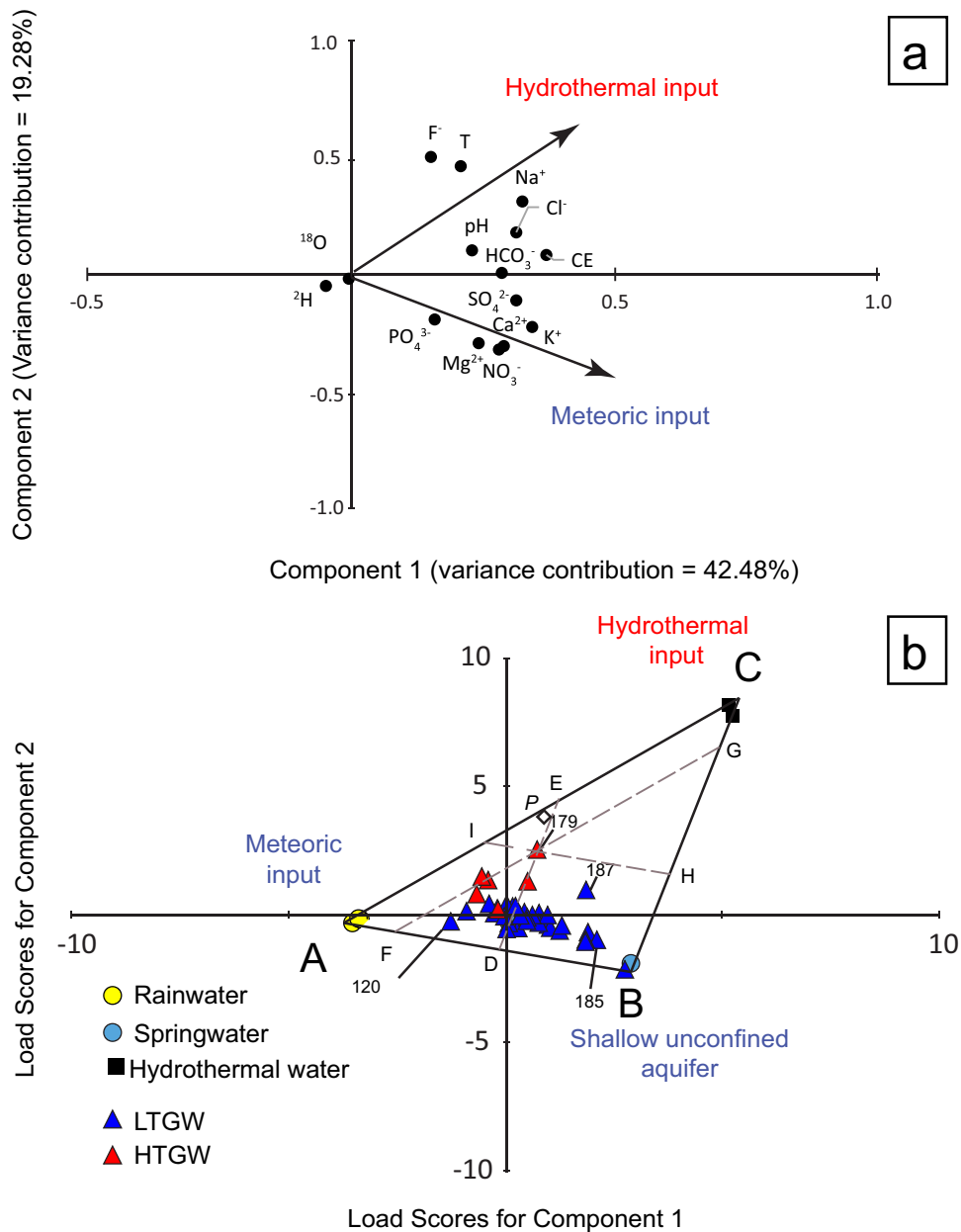
The enrichment in chloride concentrations observed in Los Geysers hydrothermal groundwater when compared to the SJRB groundwater groups suggests the contribution of regional hydrothermal fluids in the SJRB. Furthermore, the observed hydrochemical and isotopic overlapping of the spring water, LTGW and HTGW groups confirms that the shallow- and fractured-aquifer formations are hydraulically connected.

Mixing patterns

The scores of the discriminant functions used for the 30 groundwater samples are shown in Fig. 9a,b, where they are enclosed by a triangle whose vertices a, b, and c reflect the three identified water reservoir end-members in the SJRB—end-member A represents local meteoric recharge; end-member B represents shallow aquifer groundwater, with the highest TDS, and the longest residence time in the aquifer (San Cirilo well and Los Sabinos spring); and end-member C represents the regional hydrothermal groundwater samples (Los Geyser hydrothermal wells). The remaining LTGW and HTGW samples likely represent the mixing between the aforementioned end members.

Rainwater (A component) is the dominant component in all groundwater samples, ranging from 43.3 to 59.9% (median of 54.7%) for LTGW and from 40.3 to 53.5% (median of 48.1%) for HTGW. The rainwater fraction is comparable in all samples and does not show a direct correlation with groundwater temperature, chemistry, residence time or well depth. The B reservoir represents water stored in the aquifer and is the oldest groundwater end member. The estimated fraction for component B ranges from 18.1 to 31.3 % with a median at 26% in the HTGW samples, while the LTGW samples show a higher proportion from 27.2 to 35.7%, with a median at 32.5%. Finally, the fraction of hydrothermal water (C component) is larger in the HTGW than in the LTGW samples, ranging from 15.2 to 41.6% with a median at 26% in HTGW, while the LTGW samples show hydrothermal fractions from 2.4 to 23.3%, with a median at 12.8%.

Fig. 9 **a** Load distribution for component 1 and component 2 of the physico-chemical (major elements) and isotope ($O-^2H$) analysis in the San Juan del Río Basin. **b** PCA model for calculating the groundwater mixing ratio in the San Juan del Río Aquifer. The end members are represented by meteoric input (A), shallow groundwater (B) and hydrothermal water from Los Geysers (C). For analytical detailed, please refer to ESM1



The results of the mixing model validate the initial selection of groundwater groups based on the hierarchical clustering analysis (LTGW and HTGW): the well with the warmest groundwater has the largest fraction of hydrothermal fluids (C component) (well 179: $T = 45^\circ\text{C}$; A (40.3%), B (18.1%), C (41%)). These results suggest that global mixing is controlled by the hydrothermal reservoir (C component). Groundwater samples with an elevated C component are restricted along the NW–SE San Fandila and Opalos fault systems (Figs. 2 and 3a). Also, the largest fraction of the B component in groundwater is observed in both the shallow graben sedimentary filling area of the SJRB aquifer and in the perched aquifer of Amealco (well 120; Fig. 3a,b). The observed variation

of the C component (thermal) within the granular aquifer in the graben area can be explained by the distance from the wells to the N–S faults, confirming the hydraulic connection between these two groundwaters. The average of the external inputs (components A and C) in the SJRB aquifer represents up to 70% of the total mixing, and an estimated 25–50% of this 70% comes from the hydrothermal reservoir—a volume which is actually ignored in the water budget balance and should be integrated into further estimations. This mixing model highlights not only the recharge dynamics but also the groundwater hydrogeochemical processes and the water quality dissimilarities observed in the SJRB aquifer.

Groundwater flow system of San Juan del Rio Basin

The San Juan del Rio hydrologic basin is located at the head of the Lerma-Chapala regional basin. The SJRB is limited and surrounded by Miocene to Pliocene volcanic calderas and active neotectonic N–S structures. Although the regional volcanic context, which estimates the latest volcanic event at ~3.4 Ma (Fig. 10; Aguirre-Díaz and López-Martínez 2001), does not support the existence of a warm shallow magma chamber below the SRJB, as the hydrothermal alteration of the drilled volcanic formation along the N–S fault system suggests the circulation of hydrothermal fluids. In the national heat flow map, the SJRB is positioned at the front of the trans volcanic magmatic arc and does not belong to the heat flow anomaly (Prol-Ledesma et al. 2018). For Los Geysers thermal springs, González-Guzmán et al. (2019) conclude that a favorable tectonic framework allows the rise of mantle fluids by deep discontinuities through the crust at the northern TMVB, specifically the N–S Taxco-San Miguel de Allende fault systems—locally named the San Fandila and Sierra de Opalos fault systems. The productive wells found in the study area, are typically drilled in Amazcala tuff underlaid by Miocene and Oligocene rocks. Locally, groundwater chemistry evolves from a Ca–Na–HCO₃ mixing with Na⁺/K⁺/HCO₃⁻/Cl⁻/SO₄²⁻ water facies, with relatively high contents of SO₄, NO₃⁻, Na⁺ and Cl⁻, thus indicating local anthropogenic pollution. Local groundwater recharge for SJRB originates mainly from rainfall over the Amazcala, Amealco, and Huichapan calderas, with a significant deep regional hydrothermal contribution. Meteoric recharge flows from the volcanic Vaquerias and Huimilpan Sierras towards the valley floor and is channeled to regulation dams that contribute to both evaporation and infiltration (Fig. 10). The

meteoric recharge water is of Na–HCO₃ water type with low temperatures, salinities, Cl–Na concentration, and locally elevated NO₃ concentrations. Such physico-chemical characteristics indicate little mixing of flow paths and recent recharge from soils and return flow from agricultural plots, especially in the valley area. As groundwater flows in a northwestern direction following the regional hydraulic gradient, its chemistry evolves moderately. Thermal groundwater flows through the lower Miocene fractured volcanic aquifer, specifically through the San Fandila and Opalo N–S fault systems. These Na⁺/K⁺–HCO₃⁻–Cl⁻–SO₄²⁻ waters are characterized by warmer temperatures, higher salinity and larger chloride, sodium and bicarbonate concentrations, with low Δ¹⁴C age, and significant concentrations of fluoride, thus suggesting “thermal” influence and/or interaction with Miocene volcanic formations. Stable isotopy indicates that the source of all samples is meteoric with different grades of evaporation or rock interaction processes.

Groundwater ¹⁴C age can be classified into two groups: the valley groundwater (HTGW and LTGW) and the Amealco caldera. Both groups are the result of multicomponent mixing of rainwater, groundwater and thermal water. The presented residence ages are corrected from soil CO₂ gas, rainwater and water–rock interaction contributions following the carbon isotopic signature of each groundwater group. The less corrected residence ages were found in the Amealco caldera perched aquifer (<1,730 years). The age variation observed from apparent (2,925 and 5,454 years) to corrected ages (902 and 1,730 years) represents the soil and meteoric CO₂ contribution during vertical recharge (Fig. 7b). The apparent residence ages of the valley groundwater present a larger variation range (1,560–16,866 years) than the corrected residence ages (5,481–8,879 years). The

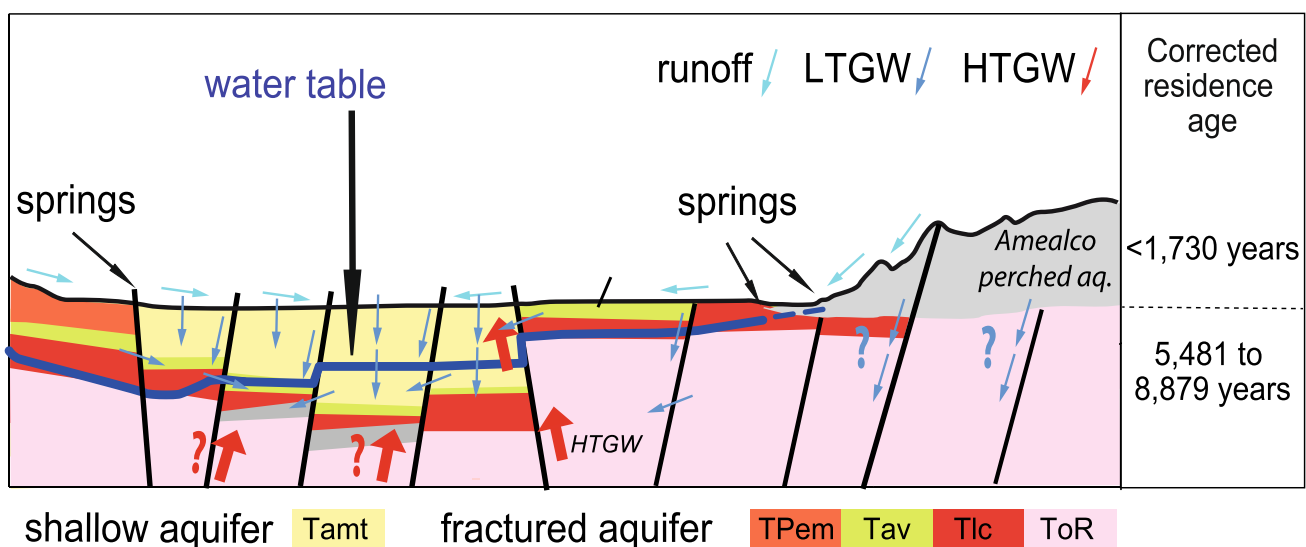


Fig. 10 Conceptual model of the hydrological dynamic of the San Juan del Rio basin

apparently young age group (up to 5,897 years) belongs to the LTGW. Following their isotopic carbon signature, the main factor of correction applied for the LTGW is the meteoric CO₂ contribution. The corrected residence ages are older than the apparent ages and their variation range is more restricted (5,553–8,879 years). The average magnitude of the correction of the meteoric impact represents 50% of the value of the corrected age of residence. This magnitude is comparable with the meteoric contribution estimated for the LTGW with the PCA mixing diagram (A component has a mean of 55%). The isotopic carbon signature of the HTGW suggests that the main factors of apparent age correction will be the water–rock interaction (hydrothermal component) and some meteoric contributions (A component). The HTGW corrected residence ages are comparable in range to those obtained for the LTGW, suggesting that the correction processes for both water types are coherent. Mixing in the HTWG is more complex than in the LTGW, where the C component is negligible. However, taking into account the corrected residence time for valley groundwater and the comparable meteoric proportion (as determined by PCA mixing for HTGW and LTGW, along with their respective ¹⁴C_(pmc)) HTGW represents the oldest mixing component. The differences between the valley and perched aquifer radiocarbon ages (almost 7,000 years) suggest that these aquifers are different hydrological systems, and the discontinuity between both aquifers can be caused by the regional Miocene Sierra de Vaquerias andesite. The Vaquerias andesite underlies the Amealco caldera pyroclastic permeable material, thus favoring the occurrence of springs at the bottom of the Amealco caldera. However, recent regional and local normal fractures affect the entire Amelaco caldera (Fig. 2) and could allow some degree of hydraulic connection between the valley and the caldera hydrologic systems (Fig. 3d).

Residence times along with the physico-chemical behavior of groundwater allows for the three different types of groundwater defined by their recharge sources and processes to be sketched: (1) groundwater in the Amealco caldera perched aquifer that is recharged by recent meteoric infiltration, (2) groundwater in the shallow granular valley aquifer that is recharged by local meteoric runoff, infiltration and regional hydrothermal water, and (3) groundwater in the fractured aquifer that is recharged by a “thermal” regional aquifer whose recharge occurs by meteoric water that infiltrates through the volcanic Sierra.

Conclusion

This work presents the first attempt to decipher groundwater flow dynamics of the San Juan del Rio Basin. This characterization is done through the integration of geochemical methods along with multivariate statistical analysis and a PCA mixing model to determine the mixing patterns of different recharge

sources in the basin, with which the anthropogenic impact in the shallow aquifer was revealed. The Euclidian clustering and PCA classification of rainwater and groundwater clusters has been confirmed and complemented with water chemistry, isotopic techniques, and Δ¹⁴C ages. With the aforementioned analyses, a conceptual groundwater flow model was constructed for the San Juan del Rio aquifer: (1) local flow is associated with rainwater infiltration, which occurs at higher altitudes within the surrounding volcanic Sierra and through run off and regulation dams in the valley floor, (2) thermal waters are related to recharge in the Sierra limiting the study area, as they flow vertically towards the surface along the N–S fault system (locally called San Fandila and Opalo faults), as indicated by their TDS, Cl, Na, F and Li content, (3) there is agricultural return flow in the shallow aquifer (confirmed by the presence of SO₄ and NO₃ in water from shallow wells).

According to the PCA mixing model, meteoric water represents the largest recharge source (up to 60%) in all groundwater samples, while thermal groundwater (2–12%) controls the groundwater physico-chemistry mixing. The contribution of thermal groundwater to the aquifer cannot be overlooked, which is often the case with traditional water balance calculations. These results can help authorities in charge of water management to identify the most sensible areas in an aquifer for extraction such as the perched aquifer, and the recharge areas, in order to locate sources of point-source pollution (agricultural areas). The proportions of rainwater, groundwater, and thermal groundwater extracted from each well provide a better understanding of the consequences of overpumping, such as water-table drawdown and the deterioration of water quality caused by an increased flux of thermal groundwater.

Supplementary Information The online version contains supplementary material available at <https://doi.org/10.1007/s10040-022-02536-y>.

Acknowledgements This research is part of the first author’s PhD project in the framework of the Universidad Nacional Autónoma de México (UNAM) Postgraduate Program. We thank Comité Técnico de Aguas Subterráneas SJR, Junta de Agua Potable y Alcantarillado Municipal SJR, and Comisión Estatal de Aguas Querétaro for sharing information and logistical support. We thank Carolina Muñoz for assistance at the Crustal Fluid Laboratory and Pedro Morales, Francisco Otero, and Edith Cienfuegos for technical assistance with the δ²H–δ¹⁸O analyses at the Laboratorio Universitario de Geoquímica Isotópica, and also Octavio Velázquez at Beta Analytics Laboratory in Miami, USA for the ¹⁴C and δ¹³C analyses and support.

Funding The research was funded by CONACYT grant CB-255070 to G. Levresse.

Declarations

Competing interest The authors declare that they have no known competing financial interests or personal relationships that could have influenced the work reported in this paper.

References

- Aguirre-Díaz GJ (1995) La Toba Amealco Y Su Correlacion Con La Formacion Las Americas a traves del graben de Acambay y Estados de México, Michoacán y Querétaro, Mexico [The Amealco Tuff and its correlation with the Las Americas Formation through the Acambay graben and the states of Mexico, Michoacán and Querétaro, Mexico]. *Rev Mex Cienc Geol* 12:17–21
- Aguirre-Díaz GJ (1996) Volcanic stratigraphy of the Amealco caldera and vicinity, Central Mexican Volcanic Belt. *Rev Mex Cienc Geol* 13:10–51
- Aguirre-Díaz GJ, López-Martínez M (2001) The Amazcala caldera, Queretaro, Mexico: geology and geochronology. *J Volcanol Geotherm Res* 111(1–4):203–218. [https://doi.org/10.1016/S0377-0273\(01\)00227-X](https://doi.org/10.1016/S0377-0273(01)00227-X)
- Aguirre-Díaz GJ, López-Martínez M (2009) Geologic evolution of the Donguinyó-Huichapan caldera complex, central Mexican Volcanic Belt, Mexico. *J Volcanol Geotherm Res* 179:133–148. <https://doi.org/10.1016/j.jvolgeores.2008.10.013>
- Aguirre-Díaz GJ, McDowell FW (2007) Volcanic evolution of the Amealco caldera, central Mexico. In: Cenozoic tectonics volcanism of Mexico. Spec. Pap. 334, pp 179–193. <https://doi.org/10.1130/0-8137-2334-5.179>
- Alaniz-Álvarez SA, Nieto-Samaniego ÁF (2005) El sistema de fallas Taxco-San Miguel de Allende y la Faja Volcánica Transmexicana, dos fronteras tectónicas del centro de México activas durante el Cenozoico [The Taxco-San Miguel de Allende fault system and the Trans-Mexican Volcanic Belt: two tectonic boundaries of the central Mexico active during the Cenozoic]. *Bol Soc Geol Mex* 57:65–82. <https://doi.org/10.18268/bsgm2005v57n1a4>
- Alaniz-Álvarez SA, Nieto-Samaniego ÁF, Reyes-Zaragoza MA, Orozco-Esquível MT, Ojeda-García ÁC, Vassallo LF (2001) Estratigrafía y deformación extensional en la región San Miguel de Allende-Querétaro, México [Stratigraphy and extensional deformation in the San Miguel de Allende-Queretaro region, Mexico]. *Rev Mex Cienc Geol* 18:129–148
- Ambach W, Dansgaard W, Eisner H, Möller J (2012) The altitude effect on the isotopic composition of precipitation and glacier ice in the Alps. *Tellus* 20:595–600. <https://doi.org/10.3402/tellusa.v20i4.10040>
- Aranda-Gómez JJ, McDowell FW (1998) Paleogene extension in the Southern Basin and Range Province of Mexico: syndepositional tilting of Eocene red beds and Oligocene volcanic rocks in the Guanajuato mining district. *Int Geol Rev* 40:116–134. <https://doi.org/10.1080/00206819809465201>
- Arango-Galván C, Prol-Ledesma RM, Flores-Márquez EL, Canet C, Villanueva Estrada RE (2011) Shallow submarine and subaerial, low-enthalpy hydrothermal manifestations in Punta Banda, Baja California, Mexico: geophysical and geochemical characterization. *Geothermics* 40:102–111. <https://doi.org/10.1016/j.geothermics.2011.03.002>
- Armienta MA, Segovia N (2008) Arsenic and fluoride in the groundwater of Mexico. *Environ Geochem Health* 30:345–353. <https://doi.org/10.1007/s10653-008-9167-8>
- Arreguín-Cortés FI, López-Pérez M, Cervantes-Jaimes CE (2020) Water challenges in Mexico. *Tecnol Cie Agua* 11:341–371. <https://doi.org/10.24850/j-tyca-2020-02-10>
- Billarent-Cedillo A, Levresse G, Ferrari L, Inguaggiato C, Hernández-Pérez E, Hernández-Espriú A, Arias-paz A, Corbo-Camargo F, Carrera-Hernández JJ (2021) Geothermics Deciphering origins and pathways of low-enthalpy geothermal waters in the unconventional geothermal system of Juchipila graben (central Mexico):94. <https://doi.org/10.1016/j.geothermics.2021.102076>
- Byers HR, Moses H, Harney PJ (1949) Measurement of rain temperature. *J Meteorol* 6:51–55. [https://doi.org/10.1175/1520-0469\(1949\)006%3c0051:mort%3e2.0.co;2](https://doi.org/10.1175/1520-0469(1949)006%3c0051:mort%3e2.0.co;2)
- Carreón-Freyre D, Cerca M, Luna-González L, Gámez-González FJ (2005) Influencia de la estratigrafía y estructura geológica en el flujo de agua subterránea del Valle de Querétaro [Influence of the stratigraphy and geological structure on the groundwater flow of the Queretaro Valley]. *Rev Mex Cienc Geol* 22:1–18
- Carrera-Hernández JJ, Carreón-Freyre D, Cerca-Martínez M, Levresse G (2016) Groundwater flow in a transboundary fault-dominated aquifer and the importance of regional modeling: the case of the city of Querétaro, Mexico. *Hydrogeol J* 24:373–393. <https://doi.org/10.1007/s10040-015-1363-x>
- Carrera-Hernandez JJ (2018) A tale of Mexico's most exploited—and connected—watersheds: the Basin of Mexico and the Lerma-Chapala Basin. *WIREs Water* 5:1–15. <https://doi.org/10.1002/wat2.1247>
- Carrillo-Rivera JJ, Cardona A, Edmunds WM (2002) Use of abstraction regime and knowledge of hydrogeological conditions to control high-fluoride concentration in abstracted groundwater: San Luis Potosí Basin, Mexico. *J Hydrol* 261:24–47. [https://doi.org/10.1016/S0022-1694\(01\)00566-2](https://doi.org/10.1016/S0022-1694(01)00566-2)
- Carucci V, Petitta M, Aravena R (2012) Interaction between shallow and deep aquifers in the Tivoli Plain (central Italy) enhanced by groundwater extraction: a multi-isotope approach and geochemical modeling. *Appl Geochem* 27:266–280. <https://doi.org/10.1016/j.apgeochem.2011.11.007>
- Chowdhury S, Dey S, Ghosh S, Saud T (2016) Satellite-based estimates of aerosol washout and recovery over India during monsoon. *Aerosol Air Qual Res* 16:1302–1314. <https://doi.org/10.4209/aaqr.2015.01.0018>
- Christophersen N, Hooper RP (1992) Multivariate analysis of stream water chemical data: the use of Principal Components Analysis for the end-member mixing problem. *Water Resour Res* 28:99–107. <https://doi.org/10.1029/91WR02518>
- Cloutier V, Lefebvre R, Therrien R, Savard MM (2008) Multivariate statistical analysis of geochemical data as indicative of the hydrogeochemical evolution of groundwater in a sedimentary rock aquifer system. *J Hydrol* 353:294–313. <https://doi.org/10.1016/j.jhydrol.2008.02.015>
- Cooper HH, Jacob CE (1946) A generalized graphical method for evaluating formation constants and summarizing well-field history. *Eos Trans Am Geophys Union* 27:526–534. <https://doi.org/10.1029/TR027i004p00526>
- Coplen TB (1988) Normalization of oxygen and hydrogen isotope data. *Chem Geol Isot Geosci Sect* 72:293–297. [https://doi.org/10.1016/0168-9622\(88\)90042-5](https://doi.org/10.1016/0168-9622(88)90042-5)
- Craig H (1961) Isotopic variations in meteoric waters. *Environ Sci Geol* 133:1702–1703
- Cruz-Ayala MB, Megdal SB (2020) An overview of managed aquifer recharge in Mexico and its legal framework. *Water (Switzerland)* 12. <https://doi.org/10.3390/w12020474>
- Dansgaard W (1964) Stable isotopes in precipitation. *Tellus* 16:436–468. <https://doi.org/10.3402/tellusa.v16i4.8993>
- Dávalos-Álvarez OG, Nieto-Samaniego ÁF, Alaniz-Álvarez SA, Gómez-González JM (2005) Las fases de deformación cenozoica en la región de Huimilpan, Querétaro, y su relación con la sismicidad local [Cenozoic deformation phases in the Huimilpan region, Queretaro, and their relationship with local seismicity]. *Rev Mex Cienc Geol* 22:129–147
- Dogramaci S, Herczeg AL (2002) Strontium and carbon isotope constraints on carbonate-solution interactions and inter-aquifer mixing in groundwaters of the semi-arid Murray Basin, Australia. *J Hydrol* 262:50–67. [https://doi.org/10.1016/S0022-1694\(02\)00021-5](https://doi.org/10.1016/S0022-1694(02)00021-5)
- Ferrari L, Orozco-Esquível T, Bryan SE, López-Martínez M, Silva-Fragoso A (2018) Cenozoic magmatism and extension in western Mexico: linking the Sierra Madre Occidental silicic large igneous province and the Comondú Group with the Gulf of California Rift. *Earth-Sci Rev* 183:115–152. <https://doi.org/10.1016/j.earscirev.2017.04.006>
- Ferrari L, Conticelli S, Vaggelli G, Petrone CM, Manetti P (2000) Late Miocene volcanism and intra-arc tectonics during the early development of the Trans-Mexican Volcanic Belt. *Tectonophysics* 318:161–185. [https://doi.org/10.1016/S0040-1951\(99\)00310-8](https://doi.org/10.1016/S0040-1951(99)00310-8)

- Fontes J-C, Garnier J-M (1979) Determination of the initial ^{14}C activity of the total dissolved carbon: a review of the existing models and a new approach. *Water Resour Res* 15:399–413. <https://doi.org/10.1029/WR015i002p00399>
- Giggenbach WF, Lyon GL (1977) The chemical and isotopic composition of water and gas discharges from the Ngawha geothermal field, Northland. Unpubl. DSIR Geothermal Circular, CD 30/555/7 WFG
- Gleason JA, Flores CC (2021) Challenges of water sensitive cities in Mexico: the case of the metropolitan area of Guadalajara. *Water (Switzerland)* 13:1–19. <https://doi.org/10.3390/w13050601>
- González-Guzmán R, Inguaggiato C, Peiffer L, Weber B, Kretzschmar T (2019) Fault-controlled geothermal fluids of the northern Trans-Mexican Volcanic Belt: a geochemical and isotopic study of the Los Geysers field (Valley of Queretaro, Mexico). *J Volcanol Geotherm Res* 388. <https://doi.org/10.1016/j.jvolgeores.2019.106681>
- Guerrero-Martínez L, Hernández-Marín M, Burbey TJ (2018) Estimation of natural groundwater recharge in the Aguascalientes semiarid valley, Mexico. *Rev Mex Cienc Geol* 35:268–276. <https://doi.org/10.22201/cgeo.20072902e.2018.2.1022>
- Han LF, Plummer LN (2013) Revision of Fontes & Garnier's model for the initial ^{14}C content of dissolved inorganic carbon used in groundwater dating. *Chem Geol* 351:105–114. <https://doi.org/10.1016/j.chemgeo.2013.05.011>
- Han LF, Plummer LN, Aggarwal P (2012) A graphical method to evaluate predominant geochemical processes occurring in groundwater systems for radiocarbon dating. *Chem Geol* 318–319:88–112. <https://doi.org/10.1016/j.chemgeo.2012.05.004>
- Hegg DA, Clarke AD, Doherty SJ, Ström J (2011) Measurements of black carbon aerosol washout ratio on Svalbard. *Tellus Ser B Chem Phys Meteorol* 63:891–900. <https://doi.org/10.1111/j.1600-0889.2011.00577.x>
- Herrera, Custodio (2003) Hipótesis sobre el origen de la salinidad de las aguas subterráneas en la isla de Fuerteventura, Archipiélago de Canarias. *Boletín geológico y minero* 114(4):433–452
- Hernández-Antonio A, Mahlknecht J, Tamez-Meléndez C, Ramos-Leal J, Ramírez-Orozco A, Parra R, Ornelas-Soto N, Eastoe CJ (2015) Groundwater flow processes and mixing in active volcanic systems: the case of Guadalajara (Mexico). *Hydrol Earth Syst Sci* 19:3937–3950. <https://doi.org/10.5194/hess-19-3937-2015>
- Hernández-Pérez E, Levresse G, Carrera-hernández J, García-martínez R (2020) Short term evaporation estimation in a natural semiarid environment: new perspective of the Craig-Gordon isotopic model. *J Hydrol* 587:124926. <https://doi.org/10.1016/j.jhydrol.2020.124926>
- Huang J, Wang T, Wang W, Li Z, Yan H (1955) Journal of Geophysical Research. *Nature* 175:238
- Laaksoharju M, Skårman C, Skårman E (1999) Multivariate mixing and mass balance (M3) calculations, a new tool for decoding hydrogeochemical information. *Appl Geochem* 14:861–871. [https://doi.org/10.1016/S0883-2927\(99\)00024-4](https://doi.org/10.1016/S0883-2927(99)00024-4)
- Luna-Niño R, Cavazos T (2018) Formation of a coastal barrier jet in the Gulf of Mexico due to the interaction of cold fronts with the Sierra Madre Oriental mountain range. *Q J R Meteorol Soc* 144:115–128. <https://doi.org/10.1002/qj.3188>
- Mahlknecht J, Horst A, Hernández-Limón G, Aravena R (2008) Groundwater geochemistry of the Chihuahua City region in the Rio Conchos Basin (northern Mexico) and implications for water resources management. *Hydrol Process* 22:4736–4751. <https://doi.org/10.1002/hyp>
- Martini M, Solé J, Garduño-Martínez DE, Puig TP, Omaña L (2016) Evidence for two Cretaceous superposed orogenic belts in central Mexico based on paleontologic and K-Ar geochronologic data from the Sierra de los Cuarzos. *Geosphere* 12:1257–1270. <https://doi.org/10.1130/GES01275.1>
- Mook WG (1972) On the reconstruction of the initial ^{14}C content of groundwater from the chemical and isotopic composition. *Proceedings of Eighth International Conference on radiocarbon dating*, vol. 1, Royal Society of New Zealand, Wellington: 342–352
- Mook WG (1976) The dissolution-exchange model for dating groundwater with ^{14}C . *Interpretation of Environmental Isotope and Hydrochemical Data in Groundwater Hydrology*, IAEA, Vienna: 213–225
- Morales I, Villanueva-Estrada RE, Rodríguez R, Armienta MA (2015) Geological, hydrogeological, and geothermal factors associated to the origin of arsenic, fluoride, and groundwater temperature in a volcanic environment “El Bajío Guanajuatense”, Mexico. *Environ Earth Sci* 74:5403–5415. <https://doi.org/10.1007/s12665-015-4554-9>
- Murgulet D, Cook M, Murgulet V (2016) Groundwater mixing between different aquifer types in a complex structural setting discerned by elemental and stable isotope geochemistry. *Hydrol Process* 30:410–423. <https://doi.org/10.1002/hyp.10589>
- Pearson FJ, Hanshaw BB Jr (1970) Sources of dissolved carbonate species in groundwater and their effects on carbon-14 dating. *Isotope Hydrology* 1970, IAEA, Vienna: 271–286
- Popp AL, Scheidegger A, Moeck C, Brennwald MS, Kipfer R (2021) Integrating Bayesian Groundwater Mixing Modeling With On-Site Helium Analysis to Identify Unknown Water Sources, *Water Resources Research* 55(10602–10615):445. <https://doi.org/10.1029/2019WR0256772019>
- Power JF, Schepers JS (1989) Nitrate contamination of groundwater in North America. *Agric Ecosyst Environ* 26:165–187. [https://doi.org/10.1016/0167-8809\(89\)90012-1](https://doi.org/10.1016/0167-8809(89)90012-1)
- Prol-Ledesma RM, Carrillo-de la Cruz JL, Torres-Vera MA, Membrillo-Abad AS, Espinoza-Ojeda OM (2018) Heat flow map and geothermal resources in Mexico. *Terra Digit* 2:1–15. <https://doi.org/10.22201/igg.25940694.2018.2.51>
- Rodríguez R, Morales-Arredondo I, Rodríguez I (2016) Geological differentiation of groundwater threshold concentrations of arsenic, vanadium and fluorine in El Bajío Guanajuatense, Mexico. *Geofis Int* 55:5–15. <https://doi.org/10.22201/igeof.00167169p.2016.55.1.1708>
- Sanchez R, Rodriguez L, Tortajada C (2018) Transboundary aquifers between Chihuahua, Coahuila, Nuevo Leon and Tamaulipas, Mexico, and Texas, USA: identification and categorization. *J Hydrol Reg Stud* 20:74–102. <https://doi.org/10.1016/j.ejrh.2018.04.004>
- Sow M, Lemaitre P (2016) Influence of electric charges on the washout efficiency of atmospheric aerosols by raindrops. *Ann Nucl Energy* 93:107–113. <https://doi.org/10.1016/j.anucene.2015.12.036>
- Valenzuela-Vásquez L, Ramírez-Hernández J, Reyes-López J, Sol Uribe A, Lázaro-Mancilla O (2006) The origin of fluoride in groundwater supply to Hermosillo City, Sonora. *México Environ Geol* 51:17–27. <https://doi.org/10.1007/s00254-006-0300-7>
- Van Der Ent RJ, Savenije HHG, Schaeffli B, Steele-Dunne SC (2010) Origin and fate of atmospheric moisture over continents. *Water Resour Res* 46:1–12. <https://doi.org/10.1029/2010WR009127>
- Vitòria L, Soler A, Canals À, Otero N (2008) Environmental isotopes (N, S, C, O, D) to determine natural attenuation processes in nitrate contaminated waters: example of Osona (NE Spain). *Appl Geochem* 23:3597–3611. <https://doi.org/10.1016/j.apgeochem.2008.07.018>

Publisher's note Springer Nature remains neutral with regard to jurisdictional claims in published maps and institutional affiliations.

Springer Nature or its licensor holds exclusive rights to this article under a publishing agreement with the author(s) or other rightsholder(s); author self-archiving of the accepted manuscript version of this article is solely governed by the terms of such publishing agreement and applicable law.

Capítulo IV :

Mantellic degassing of helium in an extensional active tectonic setting at front of magmatic arc (Central México).

GEOSPHERE

<https://doi.org/10.1130/GES02549.1>

5 figures; 1 table

CORRESPONDENCE:
glevresse@geociencias.unam.mxCITATION: Billarent-Cedillo, A., Hernandez-Pérez, E., Levresse, G., Inguaggiato, C., Ferrari, L., Inguaggiato, S., Lopez-Alvis, J., and Silva-Fragoso, A., 2022, Mantellic degassing of helium in an extensional active tectonic setting at front of a magmatic arc (central Mexico): *Geosphere*, <https://doi.org/10.1130/GES02549.1>.Science Editor: Christopher J. Spencer
Associate Editor: Julie RobergeReceived 10 May 2022
Revision received 5 August 2022
Accepted 6 October 2022

Published online XX Month 2022



This paper is published under the terms of the CC-BY-NC license.

© 2022 The Authors

Mantellic degassing of helium in an extensional active tectonic setting at front of a magmatic arc (central Mexico)

Andrea Billarent-Cedillo¹, Eliseo Hernandez-Pérez¹, Gilles Levresse², Claudio Inguaggiato³, Luca Ferrari², Salvatore Inguaggiato⁴, Jorge López-Alvis², and Argelia Silva-Fragoso²

¹Posgrado en Ciencias de la Tierra, UNAM Campus Juriquilla, Boulevard Juriquilla 3001, Querétaro 76230, México

²Centro de Geociencias, UNAM Campus Juriquilla, Boulevard Juriquilla 3001, Querétaro 76230, México

³Departamento de Geología, Centro de Investigación Científica y de Educación Superior de Ensenada (CICESE), Carretera Ensenada-Tijuana 3918, Ensenada, Baja California, México

⁴Istituto Nazionale di Geofisica e Vulcanologia, Sezione di Palermo, via Ugo La Malfa, 143, 90145 Palermo, Italy

ABSTRACT

The physicochemical and isotopic characteristics of groundwater and dissolved gas of central Mexico provide valuable information about the geologic and tectonic context of the area. Low–high-enthalpy manifestations (up to 98 °C in springs and more than 100 °C in geothermal wells) are distributed within the San Juan del Río, Querétaro, and Celaya hydrologic basins, located at the boundary between the current Mexican magmatic arc and an extensional continental area with intraplate volcanism called Mesa Central Province. Groundwaters in the study area represent a mixture between the cold water end-member with a Ca+Mg+-HCO₃⁻ composition and a hydrothermal end-member enriched in Na⁺, K⁺, SO₄²⁻, and Cl⁻. Cold and hot groundwaters δ⁴H and δ¹⁸O plot along the same evaporation lines and do not exhibit a magmatic input. Dissolved and free gas do not show a typical volcanic composition signature. He and Ne isotope composition provide evidence of an important contribution of non-atmospheric noble gases. Although helium composition mainly has a crustal origin (21–83%), the mantellic contribution (1–39%) is higher than expected for an area lacking recent volcanism. A volatile-rich magma aging at depth was discarded as the source of this mantellic helium signature but points out a recent mantellic contribution. Thus, we propose that mantellic helium comes from the sublithospheric mantle into the shallow crust through the highly permeable tectonic boundaries between the geologic provinces, namely the N–S Taxco–San Miguel de Allende and Chapala–Tula fault systems. Mantellic helium flow rates through these fault systems were estimated to have values ranging from 0.1 m/yr to 2.9 m/yr. This He flux range implies that aside from subduction, mantle volatile degassing enhanced by crustal fault systems is the main degassing process in the region studied.

INTRODUCTION

The origin of volatiles emitted from convergent and passive margins provides fundamental constraints on how plate tectonics redistributes fluids

between terrestrial reservoirs (Hilton et al., 2002; Plank et al., 2013; Bekaert et al., 2021). In continental regions, helium isotopic composition is mainly dominated by its heavy isotope, ⁴He, as a consequence of the radioactive decay of the U-Th-enriched continental crust (O'Nions and Oxburgh, 1988; Tolstikhin and Marty, 1998; Ballentine and Burnard, 2002; Ray et al., 2009). Although this is not quite true in active tectonic regions, an important ³He input from the mantle melts to the crust can be recognized (Ballentine and Burnard, 2002). These regions are basically active continental arcs that function as conduits of mantle or magmatic material to the surface (Hilton et al., 2002), or major tectonic boundaries, such as the San Andreas fault (Kennedy et al., 1997; Kulogloski et al., 2013) and the New Zealand Alpine fault (Giggenbach et al., 1993; Menzies et al., 2016).

Fluid flow is the dominant process associated with the transport of mass and energy in the crust. Mantle volatiles play an important role in lithospheric rheology, as buoyant fluids can reach the shallow crust. Heat and mass are injected into the shallow crust when mantle fluids are able to flow through the ductile lower crust (Kennedy and van Soest, 2007). Even though the lower crust is considered an impermeable boundary due to the inability to maintain open fractures over long time scales (Byerlee, 1993), fluid transit may occur through punctual magma intrusion and degassing or by diffusion (Torgersen, 1993). Both of these methods are not very effective, and volatile fluxes are generally quite limited. However, along crustal boundaries, fault-controlled advective flow of mantle fluids through the ductile crust has been reported (Ballentine et al., 2005; Kulogloski et al., 2005). In such a case, extensive circulation of fluids is generally possible in the upper crust under hydrostatic pressure, driven by thermal or compositional gradients (Yardley and Bodnar, 2014). In magmatic arcs, fluids are intrinsically linked to tectonic processes, which favor the connection between deep and shallow fluid reservoirs and provide key structural pathways for fluids. In these complex environments, shallow waters buffer the deep fluid flow. However, in highly fractured areas with deep structures, the intensity of deep fluid flow increases, which provides a less diluted signature and the opportunity to estimate its inflow (Tardani et al., 2016; Buttitta et al., 2020).

In central Mexico, the active magmatic arc has a geographically well-defined extension called the Trans-Mexican Volcanic Belt. To the north, the

gilles levresse <https://orcid.org/0000-0001-9290-9825>

Trans-Mexican Volcanic Belt faces the Mesa Central Province that is characterized, among other things, by current intraplate volcanism. The contact zone between subduction-related magmatism and intraplate magmatism is fuzzy and marked by numerous unconventional low–medium enthalpy geothermal anomalies. On the surface, both subduction and intraplate volcanism are active but structurally controlled by crustal structures of incompatible directions (Hernández-Pérez et al., 2022). At depth, the extension to the north of the metasomatism of the mantle wedge of subduction is difficult to estimate, as is the participation of the two types of magmatism in the generation of thermal anomalies.

In this study, we analyze the possible sources and pathways for crustal and mantle fluids in a range of high–low-enthalpy hydrothermal springs from the San Juan del Río–Querétaro–Celaya Valley region, which lies at the northern border of the active magmatic arc (the Trans Mexican Volcanic Belt) and its intersection with the major crustal boundary of the San Miguel Allende–Taxco fault system (Figs. 1A and 1B).

■ REGIONAL GEOLOGICAL SETTING

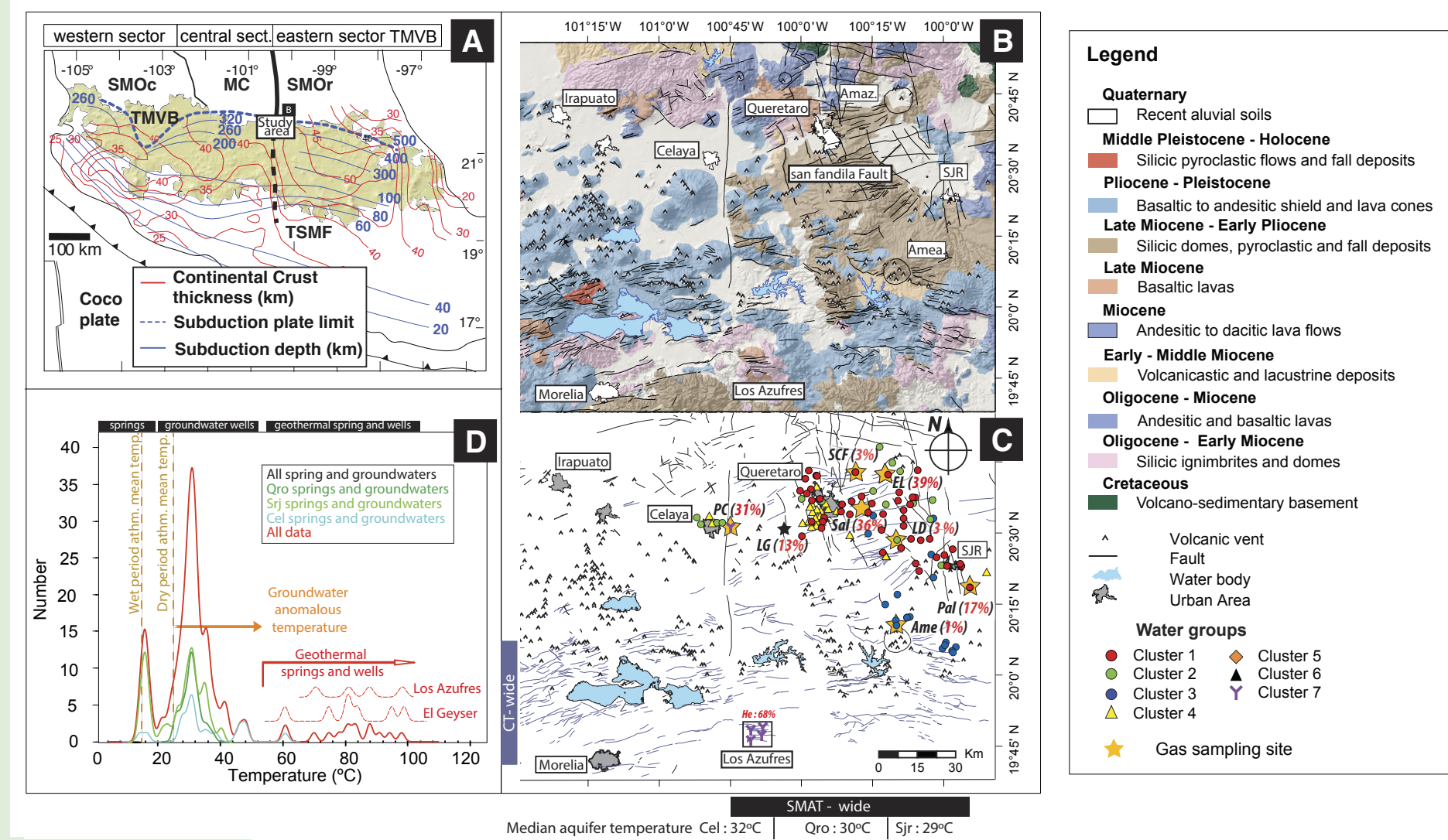
The study area is located at the intersection of three geologic provinces: the Trans-Mexican Volcanic Belt, the Mesa Central, and the Sierra Madre Oriental (Fig. 1A). The Trans-Mexican Volcanic Belt is a large Neogene continental arc that grows over the central Mexican margin of the North American Plate as a result of the subduction of the Rivera and Cocos plates along the Middle America Trench (Ferrari et al., 2012). The Trans-Mexican Volcanic Belt is composed of nearly 8000 igneous structures that extend from the coast of Jalisco to the Gulf of Mexico in Veracruz. The Trans-Mexican Volcanic Belt is divided into three sectors (Gómez-Tuena et al., 2005). The western sector contains the Chapala, Tepic-Zaocoalco, and Colima rifts, which bound the Jalisco block. The central sector includes the San Miguel de Allende–Taxco fault system and the Michoacán-Guanajuato monogenetic Pleistocene volcanic fields and is bounded to the north by the Mesa Central province. The eastern sector extends from the San Miguel Allende–Taxco fault system to the Gulf of Mexico. The seismic contours of the slab show that the Cocos Plate is sub-horizontal at the south of the Trans-Mexican Volcanic Belt. Below the Trans-Mexican Volcanic Belt the slab shows a different dip between the central and eastern sectors; it is steeper eastward (up to ~75°) (Fig. 1A). The slab is also affected by trench orthogonal tears and is truncated at ~500 km (Fig. 1A; Pérez-Campos et al., 2008; Husker and Davis, 2009; Kim et al., 2010). The truncation of the slab seen in the seismic tomography in the central Trans-Mexican Volcanic Belt occurs just below the northern boundary of the Trans-Mexican Volcanic Belt and coincides with the Bajío fault and the Chapala-Tula fault system (Fig. 1A; Botero-Santa et al., 2015). The Mesa Central province is an elevated plateau located 2000 m above sea level in central Mexico, which has undergone several episodes of magmatism and extension from the Paleocene to the Pleistocene (Nieto-Samaniego et al., 1999; Del Pilar-Martínez et al., 2020). The Sierra

Madre Oriental, the highest mountain chain in northeastern Mexico (Fig. 1A), is composed of marine sedimentary rocks of Middle Jurassic to Paleogene age. It is part of the Mexican fold-and-thrust belt that developed between the Late Cretaceous and early Eocene (Fitz-Díaz et al., 2018). Its western part is covered by volcanic and pyroclastic rocks of the Cenozoic Sierra Madre Occidental silicic large igneous province, whereas to the south it is covered by the Trans-Mexican Volcanic Belt.

The San Miguel Allende–Taxco fault system and the Chapala-Tula fault system are major crustal structural boundaries between the Mesa Central and Sierra Madre Oriental provinces and the Trans-Mexican Volcanic Belt (Fig. 1C; Alaniz-Álvarez and Nieto-Samaniego, 2005). The southern extension of the San Miguel Allende–Taxco fault system is the limit between the central and western sectors of the Trans-Mexican Volcanic Belt. The intersection between the Mesa Central, Sierra Madre Oriental, and Trans-Mexican Volcanic Belt geologic provinces is characterized by important variations in crustal thickness. In fact, the crustal thickness decreases from ~40 km to 50 km in the Trans-Mexican Volcanic Belt to ~37 km in the Sierra Madre Oriental Province and ~32 km in the Mesa Central Province (Fig. 1A). A low degree of partial melting has been interpreted from seismic studies just below the Moho in the southern Mesa Central Province and the northern part of the Trans-Mexican Volcanic Belt, which suggests that the addition of molten materials at the base of the crust produced an uplift and heating of the lower and middle part of the crust (Nieto-Samaniego et al., 1999; Ferrari et al., 2012, and references therein).

The San Miguel Allende–Taxco fault system (Alaniz-Álvarez et al., 2002) and the Chapala-Tula fault system (Aguirre-Díaz et al., 2005) intersect orthogonally in the San Juan del Río–Querétaro–Celaya region (Figs. 1B and 1C). The study area lies on the northern part of the Trans-Mexican Volcanic Belt and displays some recent volcanism (>40,000 years) in the Michoacán-Guanajuato volcanic field (Luhr et al., 2006; Gómez-Vasconcelos et al., 2020) and upper crustal historical seismicity at the Sanfandila fault (Aguirre-Díaz and McDowell, 2000; Zúñiga et al., 2003). This region is also geothermally active, with two high-enthalpy fields at Los Azufres and at Celaya, as well as several low–medium enthalpy anomalies distributed within the central Trans-Mexican Volcanic Belt (Fig. 1; González-Guzmán et al., 2019; Jácome-Paz, 2019; Pérez-Martínez et al., 2020, and references therein).

The stratigraphic column comprises rocks from the Jurassic to Quaternary. The oldest rock units are a middle Jurassic volcano-sedimentary succession (ca. 100 Ma; Ochoa-González et al., 2015) and Late Cretaceous limestone (Palacios-García and Martíni, 2014) exposed in the northeastern part of the area (Fig. 1B). This Mesozoic basement succession is sheared and folded and unconformably overlain by Oligocene to Quaternary volcanic rocks (Alaniz-Álvarez et al., 2001; Verma and Carrasco-Núñez, 2003; Arango-Guevara et al., 2007). The transition between the deformed basement and the Cenozoic volcanics is highlighted by a continental conglomerate of Eocene age (Aguirre-Díaz and McDowell, 2000; Aranda-Gómez and McDowell, 1998). The oldest volcanic pulse is Rupelian in age and is part of the major pulse of ignimbrite flare-up of the Sierra Madre Occidental large igneous province (Aguirre-Díaz and



NOTE:
Moved key to right.
Okay?

Figure 1. (A) Tectonic setting of central and southern Mexico is shown. The white box indicates the main focus area of this study. The black contour lines depict the depth of the subducted slab compiled using the results of receiver functions, tomography studies, and hypocentral relocation (from Ferrari et al., 2012). The dashed blue line represents the limit of the subducting plate. The red line illustrates the thickness of the crust beneath and south of the Trans-Mexican Volcanic Belt (in kilometers) (Ferrari et al., 2012, and references therein). The Trans-Mexican Volcanic Belt (TMVB) is delimited by the green area (from Ferrari et al., 2012). SMOc—Sierra Madre Occidental Province; MC—Mesa Central Province; SMOr—Sierra Madre Oriental Province; TSMF—Taxco San Miguel fault. (B) Simplified geological map of the study area. (C) Simplified structural map with sampling sites marked. SCF, PC, LG, Sal, EL, LD, Pal, and Ame are sample names. (D) Temperature distribution of water sampled from rain, springs, and groundwaters (low-temperature groundwater and high-temperature groundwater) of the San Juan del Río (SJR) Basin. The vertical orange dashed lines correspond to the average atmospheric temperature of the dry (21 °C) and wet (17 °C) period. In panel B: SJR—San Juan del Río city; Amea.—Amealco caldera; Huich.—Huichapan caldera; Amaz.—Amazcala caldera. Percentage in red indicates the mantellic helium contribution of each sample.

López-Martínez, 2001; Ferrari et al., 2018). It includes pyroclastic flow deposits, rhyolite domes, and lava flows, which are commonly observed discordantly overlying the deformed Mesozoic rocks. The Rupelian volcanic event is followed by a Miocene volcanic succession concurrent with the development of extensional fault systems, which is locally faulted and affected by hydrothermal alteration. The Miocene volcanism began with the emplacement of andesitic to dacitic polygenetic volcanoes dated at ca. 13–10 Ma (Pérez-Venzor et al., 1996; Valdez-Moreno et al., 1998; Verma and Carrasco-Núñez, 2003) and was followed by mafic lava flows forming an extensive plateau, a few shield volcanoes, and monogenetic cinder cones with ages ranging from 8.8 Ma to 7.5 ± 0.5 Ma. (Aguirre-Díaz and López-Martínez, 2001; Dávalos-Álvarez et al., 2005), which are mostly exposed in the Querétaro and San Juan del Río areas. Shortly after, at ca. 7.3 Ma, the volcanic activity became bimodal with the formation of the Amazcala rhyolitic caldera (Aguirre-Díaz and López-Martínez, 2001) and less voluminous fissural mafic lavas east of Querétaro. During the Pliocene (5–4.2 Ma), volcanism moves toward the southeast, with the development of the Amealco dacitic caldera and a massive rhyolitic dome complex southwest of the San Juan del Río basin (Aguirre-Díaz, 1996; Aguirre-Díaz and López-Martínez, 2009). Additional silicic volcanism occurred at the Los Azufres caldera, in the southern part of the study area, with rhyolitic ignimbrites, domes, and pyroclastic flows from the Pliocene to Holocene (Ferrari et al., 1991; Arce et al., 2021). To the west, basaltic and basaltic andesite monogenetic cones, shield volcanoes, and a few domes were emplaced in the Michoacan-Guanajuato volcanic field (Hasenaka and Carmichael, 1985; Hasenaka, 1994). Fluvial, lacustrine, alluvial deposits, and unconsolidated volcano-sedimentary and pyroclastic rocks fill the Miocene–present tectonic basins (Alaniz-Álvarez et al., 2001).

METHODS

Samples for dissolved and noble gas analysis were selected from the extensively evaluated published and personal database of physicochemical parameters of the groundwaters and spring waters from the Celaya, Querétaro, and San Juan del Río basins (see Results section) to obtain a representative panorama of the varied occurrence of groundwater types and the impact recording of deep-flow fluids within them.

Six water samples (SCF, Sal, EL, LD, Ame, and PAL) were collected from urban wells in the Querétaro and San Juan del Río basins (25–300 m), and one gas sample (PC) was collected from a geothermal well in Celaya. The waters have an abnormally high temperature except for the Ame sample, which has a much lower temperature (20.7 °C), which is close to the average atmospheric temperature. Physicochemical parameters (temperature, pH, electrical conductivity, and oxidation-reduction potential) were measured in situ using a Thermo Scientific® Orion 5-Star Plus multiparameter analyzer that was calibrated before sampling. Water $^{18}\text{O}/^{16}\text{O}$ and $^2\text{H}/\text{H}$ isotope ratios (expressed in δ -notation normalized relative to the Vienna Standard Mean Ocean Water) were analyzed at

the Laboratorio de Isotopía Estable of the Instituto de Geología, UNAM, using the Los Gatos Research DLT-100 V3® isotope ratio laser spectrometer (IRLS). The standard deviation for the $\delta^{18}\text{O}$ was less than $\pm 0.2\text{\textperthousand}$ and less than $\pm 2\text{\textperthousand}$ for the $\delta^2\text{H}\text{\textperthousand}$. All of the hydrochemical data, including the $\delta^{18}\text{O}$ and $\delta^2\text{H}\text{\textperthousand}$, are reported in Supplemental Material Table S1¹.

Water samples were collected in 121 ml glass bottles to analyze the chemical composition of gases and helium isotopes dissolved in water (Capasso and Inguaggiato, 1998; Inguaggiato and Rizzo, 2004). The glass samplers were completely filled with water and sealed underwater with rubber septa to prevent air contamination during the sampling procedure. The method used to analyze dissolved gases is based on the equilibrium partition of gases between the water phase collected and the gas phase (Capasso and Inguaggiato, 1998; Inguaggiato and Rizzo, 2004). The sample bottles were immersed in water to prevent air contamination during storage. A free gas sample was collected at the geothermal well in Celaya city.

Analysis of the chemical composition of gases and the noble gas isotopic composition was conducted at the geochemical laboratory of the Istituto Nazionale di Geofisica e Vulcanologia – Palermo (INGV-Pa) in Italy. The chemical composition of dissolved gases was analyzed by an Agilent 7890 gas chromatograph using Ar as the carrier gas. The gas chromatograph is equipped with two detectors: a thermal conductivity detector (TCD) for the analysis of He, H₂, O₂, and N₂, and a flame ionization detector (FID) for the analysis of CO, CO₂, and CH₄. A detailed description of the methods used for gas extraction and dissolved gas analysis can be found in Capasso and Inguaggiato (1998). The analytical error was less than 5%.

The ^3He , ^4He , and ^{20}Ne isotopic concentrations were measured to calculate the $^3\text{He}/^4\text{He}$ and $^4\text{He}/^{20}\text{Ne}$ ratios. Noble gases were purified from the gas mixture in a stainless steel ultra-high vacuum line and then cryogenically separated and admitted into a split-flight tube noble-gas mass spectrometer (GVIT™ Helix SFT) for He isotopes and into a noble gas multicollector mass spectrometer (Helix MC Plus™ Multicollector) for Ne isotopes. A multicollector mass spectrometer (GVIT™ Helix MC) was used to analyze Ar (Rizzo et al., 2015). The method for gas extraction and isotopic analyses is described in detail in Inguaggiato and Rizzo (2004). The analytical error was less than 3% on a single mass. The concentration of dissolved gases is expressed as cm³/g at 0 °C and 1 atm (STP). The helium isotope ratios are reported as R/Ra, where R is the $^3\text{He}/^4\text{He}$ ratio determined in the sample and Ra is the atmospheric one (1.39×10^{-6}). The R/Ra values were corrected for atmospheric contamination (Rc/Ra) using the air normalized $^4\text{He}/^{20}\text{Ne}$ ratio equation of Hilton (1996).

$$\frac{R_c}{R_a} = \frac{\left(\frac{R}{R_a} * X \right) - 1}{X - 1} \quad (1)$$

¹Supplemental Material. Table S1: Physicochemical parameters and composition of rain, spring and groundwater in the Celaya, Querétaro and San Juan del Río aquifers. Please visit <https://doi.org/10.1130/GEOS.S.21513981> to access the supplemental material, and contact editing@geosociety.org with any questions.

$$\text{where } X = \frac{\left(\frac{He}{Ne}\right)_{\text{sample}}}{\left(\frac{He}{Ne}\right)_{\text{air}}} \frac{\beta_{Ne}}{\beta_{He}} \quad (2)$$

and β_{Ne} and β_{He} are the Bunsen solubility coefficients for Ne and He, respectively, at the temperature and salinity of the water when the atmospheric helium was dissolved. Only in the case of the gas sample PC, which was not dissolved in water, the ratio of β_{Ne} and β_{He} was not used to calculate (Rc/Ra), and X is $(He/Ne)_{\text{sample}}/(He/Ne)_{\text{air}}$. R/Ra values of the LD and Amealco 1 samples were not corrected for air contamination as their $^{4}\text{He}/^{20}\text{Ne}$ value is <25% higher than the $^{4}\text{He}/^{20}\text{Ne}$ value of air, which implies a significant error for the correction.

RESULTS

Regional Hydrological System Re-Evaluation

The study area comprises three connected hydrologic basins: the San Juan del Río, Querétaro, and Celaya basins (Figs. 1B and 1C). The hydraulic basins

of San Juan del Río and Querétaro comprise the hydraulic head of the Lerma and Panuco regional basins. The piezometric gradient continually decreases from the San Juan del Río to the Celaya aquifer. However, the average temperature of the aquifers continually increases from San Juan del Río to Celaya. These aquifers can be defined as compartmentalized and multi-layer, in which granular and fractured layers with contrasting hydraulic properties, as well as several structural discontinuities, influence the groundwater flow dynamics (Carrera-Hernández et al., 2016; López-Alvis et al., 2019; Hernández-Pérez et al., 2020). Groundwater is thermally anomalous (with respect to mean air temperature of 18 °C; Fig. 1D) with localized geothermal spring occurrences along N–S structures (i.e., El Geyser and Celaya geothermal well; González-Guzmán et al., 2019) and hydro-chemically heterogeneous with F-, As-, and Li-punctual anomalies (Shaw and Sturchio, 1992; Nicolli et al., 2012; Alarcón-Herrera et al., 2013; González-Guzmán et al., 2019; Morales-Arredondo et al., 2020; Amézaga-Campos et al., 2022). For comparison, we include physicochemical data from the Los Azufres geothermal field (LA; Fig. 2). All of the physicochemical data, from the study area plus the regional geothermal field (Los Azufres; González-Partida et al., 2005; Pinti et al., 2013), were used to perform a hierarchical cluster and principal component analysis (PCA) to discriminate the different types of the sampling waters. The results derived from the PCA are presented

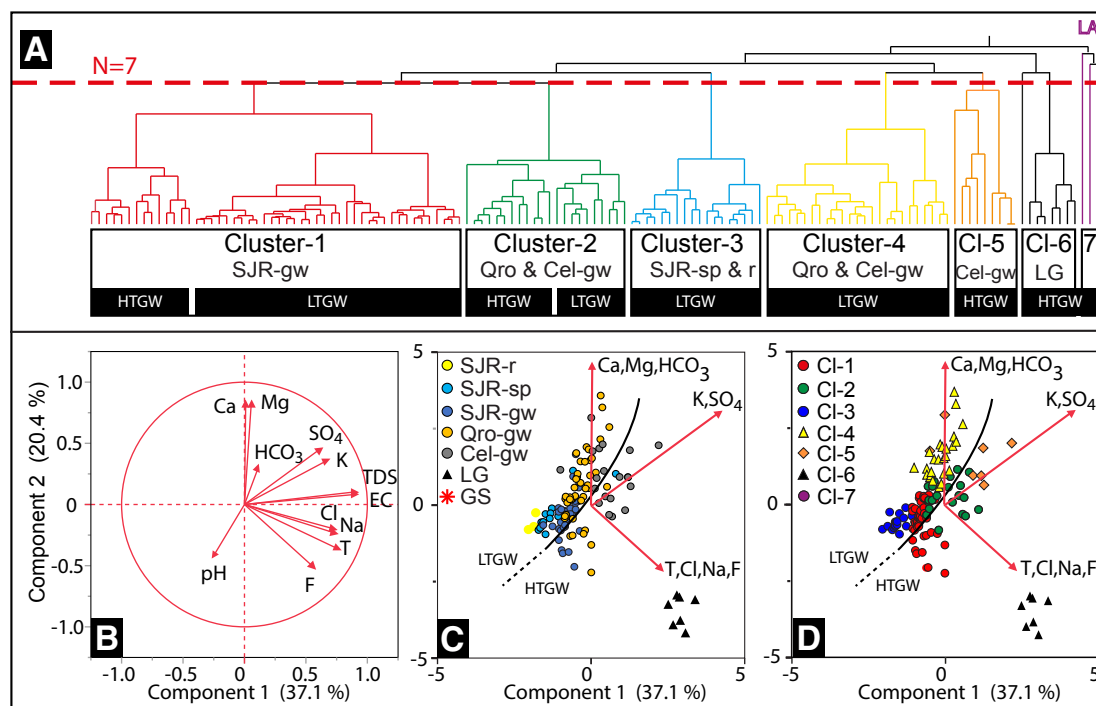


Figure 2. (A) Dendrogram shows Hierarchical Clustering Analysis classification with groups and subgroups of samples of the San Juan del Río, Querétaro, and Celaya aquifers (Hernández-Pérez et al., 2022; González-Guzmán et al., 2021; Amézaga-Campos et al., 2022). For comparison, temperature and chemical data from the Los Azufres geothermal field are presented (González-Partida et al., 2005). (B) Load distribution for Component 1 and Component 2 of the analysis variables in the San Juan del Río Basin. (C) Principal component analysis (PCA) diagram differentiated by aquifer and water type. SJR-r—San Juan del Río aquifer rain; SJR-sp—San Juan del Río aquifer spring; SJR-gw—San Juan del Río aquifer groundwater; Qro-gw—Querétaro aquifer groundwater; Cel-gw—Celaya aquifer groundwater; LG—El Geyser; LTGW—low-temperature groundwater; HTGW—high-temperature groundwater. (D) PCA diagram differentiated by aquifer cluster water type.

in Figure 2. Seven main clusters were identified using a dissimilarity index of 7, selected based on the major Euclidean distance break in the amalgamation graph (Fig. 2A). The PCA illustrates the strong apparent correlation between water type and physical-chemical parameters and confirms that our differentiation is robust. In Figures 2C and 2D, rain and low-temperature groundwater (LTGW; temperature <35 °C) share a geochemical evolution on a continuum. The internal division of LTGW suggests an east–west enrichment (from San Juan del Río to Celaya) in Ca⁺-Mg⁺-HCO₃⁻, which is in good agreement with piezometric gradient and residence time/water-rock interaction processes. To simplify the data presentation and discussion, the rainwaters and LTGW (<35 °C) will be considered, respectively, as a single population (Fig. 2C and 2D). Three other populations are evident in Figure 2D: (1) the geothermal springs from Los Azufres, (2) El Geyser, and (3) the groundwater of anomalous temperature in the San Juan del Río–Querétaro–Celaya aquifers (temp >35 °C, high-temperature groundwater [HTGW], Fig. 2C; and <35 °C, Fig. 2D). It is remarkable that the Los Azufres and El Geyser geothermal springs represent two different end-members. The Geyser springs are characterized by high temperatures and NaCl and Fluor enrichment. HTGW samples seem to represent a mixing pattern from LTGW to the El Geyser end-members. Finally, few samples from Celaya aquifer compose the cluster 5. They are characterized by SO₄²⁻ and K⁺ enrichment probably related to the dissolution of Jurassic evaporites. The special case of high-sulfate water in the PC gas sample is related to the observed precipitation of carbonate in the water deposit from where it was sampled. Cl-SO₄ water

composition and increasing temperatures in all of the basins are correlated with specific geographic features (buried N–S faults), which indicates that the regional geology/lithology may be a determining factor that influences the physicochemical characteristics of water. The δ²H-δ¹⁸O isotopic composition of all rainwater, spring water, and groundwater (LTGW and HTGW; Fig. 3) is close to the Global Meteoric Water Line and Local Meteoric Water Line (LMWL) defined for San Juan del Río by Hernández-Pérez et al. (2020), which indicates a main meteoric contribution. All groundwater clusters (LMWL; Celaya, Querétaro, San Juan del Río aquifers) plot along common regression lines comparable to the Local Evaporation Line (LEL) as defined by Hernández-Pérez et al. (2020; LEL: δ²H = 5.38 δ¹⁸O - 19.84). Even the HTGW samples from San Juan del Río–Celaya Valley (including geothermal fluids from El Geyser) do not show evidence of an andesitic source (González-Guzmán et al., 2019).

Evaluation of the physicochemical and isotopic data set from the San Juan del Río–Querétaro–Celaya groundwater (LTGW and HTGW) and springs, including El Geyser, shows no relationship to the Los Azufres samples or a volcanic water signature.

Gas Chemistry and Helium Isotopes

N₂, CO₂, and O₂ are the predominant dissolved gas species in the groundwater samples (Table 1). Their concentrations range from 8.12 × 10⁻³ to

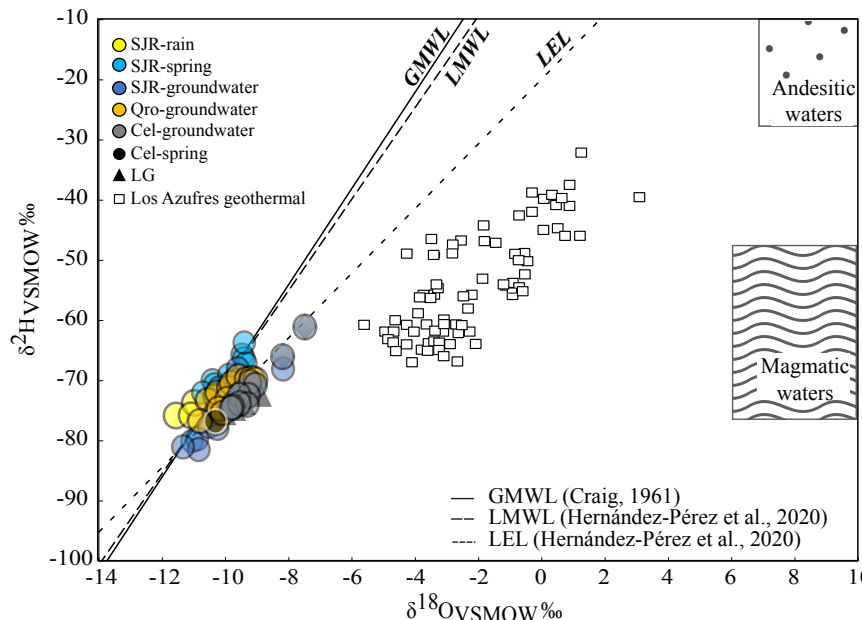


Figure 3. δ²H-δ¹⁸O isotopic data from groundwater samples (spring and wells) from the Celaya (Cel)-Querétaro (Qro)-San Juan del Río (SJR) basins show a main evaporation isotopic trend with a common meteoric origin (Hernández-Pérez et al., 2022; Amézaga-Campos et al., 2022). For comparison, the isotopic data from regional hydrothermal springs and wells were added (El Geyser and los Azufres; Barragan et al., 2005; González-Partida et al., 2005; González-Guzmán et al., 2019; Pinti et al., 2013; Nieva et al., 1987). VSMOW—Vienna Standard Mean Ocean Water. GMWL—Global Meteoric Water Line; LMWL—Local Meteoric Water Line; LEL—Local Evaporation Line. LG is a sample.

TABLE 1. PHYSICAL COMPOSITION AND HE-NE-C ISOTOPIC COMPOSITION OF THE GROUNDWATER DISSOLVED GAS FRACTION OF THE CELAYA, QUERETARO, AND SAN JUAN DEL RÍO AQUIFERS

Sample type	Dissolved gases							Free gas
	Sample name	Santa Cruz Forrajes	El Lobo	Saldarraga	La D	Amealco 1	Palmillas	Pozo Celaya (water flow)
Aquifer	Qro	Qro	Qro	SRJ	SRJ	SRJ	Cel	Cel
Long	363597	375555	365807	380114	382137	405328	317759	317759
Lat	2291117	2290015	2281668	2261430	2234320	2245940	2270992	2270992
T (°C)	42.7	41.4	39.7	34.5	20.7	41.6	87.9	—
pH	8.0	7.5	8.8	8.0	7.5	8.7	9.0	—
EC (µs/cm)	434	466	489	282	152	441	5920	—
TDS (ppm)	213	229	240	139	74	216	2905	—
ORP (Mv)	14	21	3	54	24	213	-193	—
R/Ra (Laboratory)	0.36	2.96	2.67	0.99	0.85	1.30	—	2.31
⁴ He/ ²⁰ Ne (Laboratory)	1.94	2.17	11.99	0.35	0.34	6.06	—	150.36
Rc/Ra	0.25	3.25	2.71	—	—	1.31	—	2.31
³ He/ ⁴ He	3.49E-07	4.50E-06	3.75E-06	1.33E-06	2.73E-07	1.81E-06	—	3.20E-06
cc(STP)/l for dissolved gas								
⁴ He (ppm)	4.19304E-07	4.60456E-07	2.54173E-06	7.41805E-08	7.12523E-08	1.65954E-06	—	121.55
H ₂ (ppm)	—	—	—	—	—	3.40031E-07	—	1406
N ₂ (%)	9.08E-03	8.12E-03	1.10E-02	9.80E-03	1.03E-02	1.11E-02	—	4.74
O ₂ (%)	1.46E-03	8.98E-04	7.24E-04	1.94E-03	1.13E-03	4.69E-04	—	1.21
CO (ppm)	—	—	—	3.68E-08	3.60E-08	1.80E-07	—	—
CH ₄ (ppm)	6.06E-08	2.04E-06	4.03E-07	7.54E-08	6.57E-08	1.40E-06	—	1.9
CO ₂ (%)	9.70E-04	5.50E-03	1.85E-04	1.67E-03	6.20E-03	1.60E-04	—	93.03
²⁰ Ne (ppm)	2.13E-07	2.09E-07	2.10E-07	2.06E-07	2.06E-07	2.71E-07	—	0.81
Ar (ppm)	2.75E-04	4.61E-04	3.01E-04	4.04E-04	2.80E-04	3.18E-04	—	1174.01

Dashes indicate data under detection limit.

$1.1 \times 10^{-2} \text{ cm}^3/\text{g}$ for the N₂, 1.6×10^{-4} to $6.2 \times 10^{-3} \text{ cm}^3/\text{g}$ for the CO₂, and 4.69×10^{-4} to $1.94 \times 10^{-3} \text{ cm}^3/\text{g}$ for the O₂. Groundwater samples have ⁴He concentrations between $7.42 \times 10^{-8} \text{ cm}^3 \text{ STP/g}$ and $1.66 \times 10^{-6} \text{ cm}^3 \text{ STP/g}$ with Rc/Ra values ranging from 0.2 to 3.25 (Table 1). ⁴He/²⁰Ne isotopic ratios dissolved in waters vary from 0.35 to 11.9, all of which are above the air-saturated water (ASW) composition ratio of 0.288.

The free gas sample from the Celaya geothermal well (PC) has a composition dominated by 93% CO₂, 4.7% N₂, and 1.2% O₂, with a ⁴He concentration of 122 ppm. The measured ⁴He/²⁰Ne ratio is 150, with an Rc/Ra value of 2.31 (Table 1).

DISCUSSION

Volatile Composition of Groundwater

The relative proportions of CO₂, N₂, and O₂ of the San Juan del Río-Querétaro-Celaya dissolved and free gas samples and El Geyser bubbling gas samples were plotted in a triangular plot (Fig. 4A) and compared with

the air and ASW values. Most of the dissolved gas samples are characterized by a CO₂ enrichment with respect to the ASW, evincing interaction with non-atmospheric CO₂. There is no clear relationship between this CO₂ enrichment and the R/Ra values (Fig. 4B). Samples Pal and Sal show an enrichment in N₂, which may be due to an interaction with Quaternary organic sediments filling the San Juan del Río graben, as these samples show a slight enrichment in CH₄ and the Pal sample also records CO concentration (Table 1).

The dry-gas chemical composition of the geothermal well in Celaya city (PC) is also characterized by a CO₂ enrichment with respect to the air composition, evincing interaction with non-atmospheric CO₂. Los Geysers bubbling gas samples display a mixing trend between air composition and a CO₂-dominated hydrothermal end-member. These samples have a relatively constant Rc/Ra value (mainly from 1.31 to 1.74; González-Guzmán et al., 2019) with variable proportions of CO₂ (Fig. 4B). This behavior, for such a small sampling area, implies different local mechanisms for the CO₂ enrichment dynamics. The δ¹³C signatures of bubbling gas and groundwater at El Geyser can be explained as part of a mixing process with an organic end-member from the sedimentary rocks in the area (Marín-Camacho et al., 2022). On the other hand, the PC sample has the highest CO₂ concentration

(93.03%), as well as the highest Rc/Ra value for free gas samples (2.31 Ra). Also, considering the helium isotopes in dissolved gases, the highest Rc/Ra value (3.25) was found in the EL sample (41.4. °C) in the San Juan del Río-Querétaro-Celaya area.

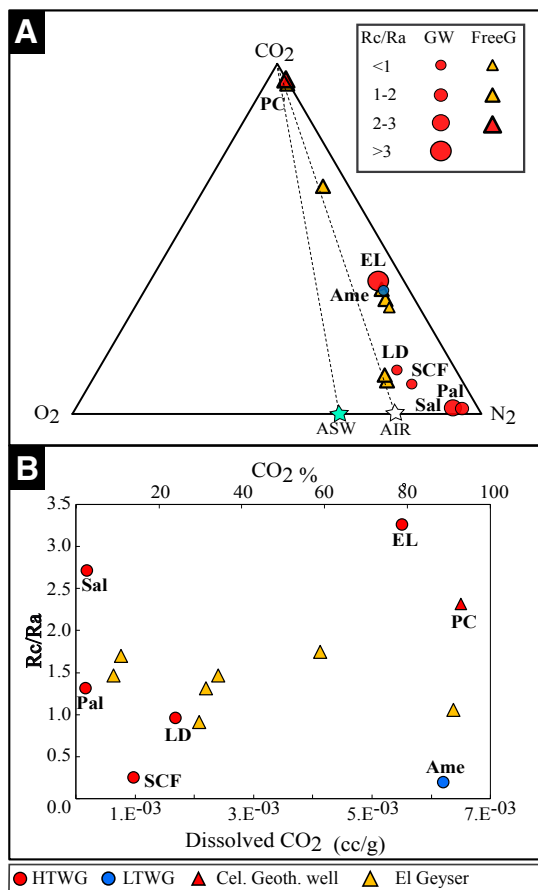


Figure 4. (A) CO₂-O₂-N₂ ternary diagram for the Celaya (Cel)-Querétaro (Qro)-San Juan del Río (SJR) groundwater samples is shown. The typical values of air (AIR) and air-saturated water (ASW) after O'Nions and Oxburgh (1988) and Smith and Kennedy (1983) are also plotted. GW—groundwater; FreeG—free gas. (B) Dissolved CO₂ (for low-temperature groundwater [LTGW] and high-temperature groundwater [HTGW] in cc/g) and free CO₂ (for the Celaya Geothermal Well and El Geyser in %) vs. Rc/Ra diagram for the Cel-Qro-SJR groundwater samples. Data from El Geyser geothermal area were taken from González-Guzmán et al. (2019). SCF, PC, Sal, EL, LD, Pal, and Ame are sample names.

Mantle-Helium Sources and Transport Mechanisms

Helium is an excellent geochemical proxy for distinguishing mantle and crustal contributions. Given the different origins, the ratio between primordial (³He) and radiogenic (⁴He) varies according to the tectonic setting. In the continental crust, radiogenic ⁴He production dominates, exhibiting an average ³He/⁴He crust end-member ratio of 0.02 Ra (Hooker et al., 1985). On the contrary, regions with mantle-derived fluids such as volcanic arcs, and mid-oceanic ridges or regions with active faults and high-seismicity, can reach average mantle end-member ratios of ³He/⁴He (Gautheron and Moreira, 2002; Graham, 2002; Hilton et al., 2002; Kulongoski et al., 2005; Hilton, 2007; Kennedy and Van Soest, 2007; Hilton and Porcelli, 2014).

The R/Ra ratio versus the ⁴He/²⁰Ne ratio for each sample is plotted in Figs. 5A and 5B. The end-members, as well as the Los Azufres geothermal wells, springs, mud volcanoes, and fumaroles samples (Pinti et al., 2013; Wen et al., 2018) were plotted for comparison. The mantle, atmospheric, and crustal helium contribution (Table 1, Figs. 5A and 5B) was calculated following the equation system proposed by Sano and Wakita (1985):

$$\frac{R}{R_a} = A \frac{R}{R_{a,ASW}} + M \frac{R}{R_{a,m}} + C \frac{R}{R_{a,c}} \quad (3)$$

$$\frac{1}{^{20}\text{Ne}} = \frac{A}{^{20}\text{Ne}_{ASW}} + \frac{M}{^{20}\text{Ne}_m} + \frac{C}{^{20}\text{Ne}_c} \quad (4)$$

$$\frac{1}{^{20}\text{Ne}} = \frac{A}{^{20}\text{Ne}_{ASW}} + \frac{M}{^{20}\text{Ne}_m} + \frac{C}{^{20}\text{Ne}_c} \quad (5)$$

where A, M, and C represent the atmospheric, mantle, and crustal He components, respectively. The end-members used for the calculations are ⁴He/²⁰Ne ratios of 0.265 for ASW (Smith and Kennedy, 1983) or 0.318 for air (O'Nions and Oxburgh, 1988), and 1000 for crustal and mantle fluids (Craig et al., 1978; Sano and Wakita, 1985); and the R/Ra ratios of 0.983 Ra for ASW (Benson and Krause, 1980) or 1 Ra for air (Graham, 2002), 0.02 Ra for the crust (Hooker et al., 1985), and 7.3 Ra for the lithospheric mantle beneath Mexico (Straub et al., 2011).

Most of the dissolved gas samples have less than a 50% contribution from ASW (except for Ame and LD). The main He source is a variable mixture of the crustal (48–82%) and mantle end-members (2.7–39%). The mantle contribution is relatively high for groundwater in a typical continental crust without recent magmatism (Mamyrin and Tolstikhin, 1984). The bubbling gas samples from El Geyser have an important atmospheric contribution (3.4–60%), a crustal contribution varying from 36% to 76%, and a mantle proportion of 4–21%. The geothermal well (PC sample) has the least atmospheric contribution (0.2%), and a major crustal proportion (68.4%) but with a high percentage of mantle-derived helium (31.4%). The San Juan del Río-Querétaro-Celaya samples have a distinct proportion of crustal- and mantle-He unlike Los Azufres, which lies

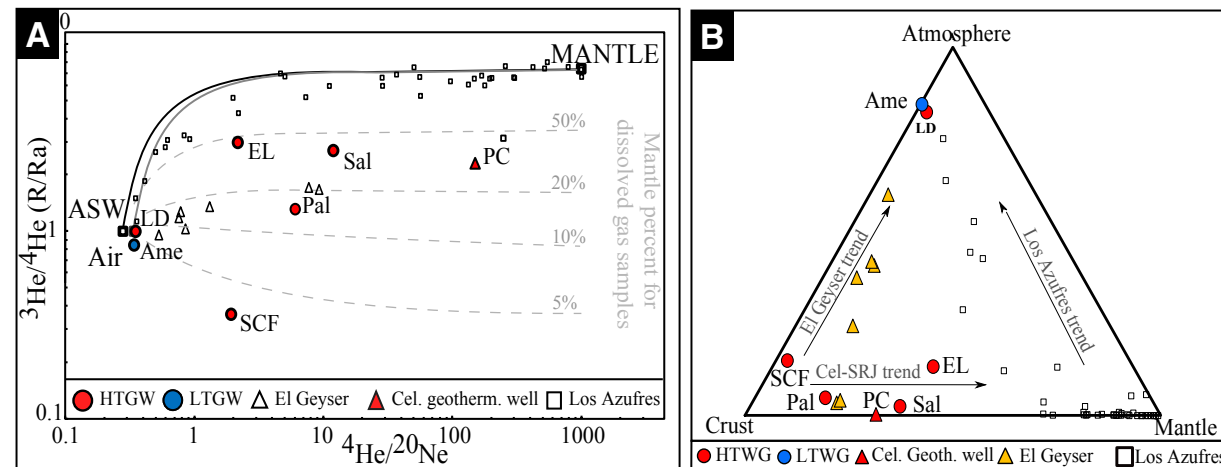


Figure 5. (A) Diagram shows ${}^3\text{He}/{}^4\text{He}$ vs. ${}^4\text{He}/{}^{20}\text{Ne}$ (after Sano and Wakita, 1985) for dissolved and free gas samples from Celaya (Cel)–Querétaro (Qro)–San Juan del Río (SJr) aquifers and Los Azufres geothermal field. Air (air) and ASW (air-saturated water) denote the atmospheric end-members (the first for the free gas and the second for the dissolved gas). The solid lines show the mixture of the atmospheric end-members with mantle end-members. The ${}^4\text{He}/{}^{20}\text{Ne}$ end-member ratios used are 0.265 for Air and ASW (Smith and Kennedy, 1983) and 1000 for crustal and mantellic fluids (Sano and Wakita, 1985). The R/Ra end-member ratios used are 1 Ra for Air, 0.983 Ra for ASW (Benson and Krause, 1980), 0.02 Ra for the crust (Hooker et al., 1985), and 7.3 Ra for the lithospheric mantle in Mexico (Straub et al., 2011). Data from Los Azufres were taken from Pinti et al. (2013) and Wen et al. (2018). Data from El Geyser was taken from González-Guzmán et al. (2019). HTGW—high-temperature groundwater; LTGW—low-temperature groundwater. No error bars are shown because they are similar to or smaller than the symbol size. Solid gray and black lines are the mixing curves between the air and mantle and the ASW and mantle end-members, respectively. (B) Atmosphere–crust–mantle ternary diagram. Santa Cruz Forjas (SCF), Pozo Celaya (PC), Saldarraga (Sal), El Lobo (EL), La D (LD), Palmillas (Pal), Amealco (Ame), and Celaya Geothermal Well (Cel Geoth Well) are sample names.

in a typical volcanic setting in the Trans-Mexican Volcanic Belt (Figs. 1B and 4B). Helium isotopes from Los Azufres springs and geothermal wells (Pinti et al., 2013), which are considered here for comparison, are characterized by an almost binary mixture that is between those of the atmospheric and mantellic end-members. These results imply a different tectonic-structural framework.

The geographical distribution of samples in the San Juan del Río–Querétaro–Celaya region may shed some light on the ${}^3\text{He}$ enrichment mechanism in groundwater. In the Celaya–Querétaro region, the El Geyser bubbling springs lie on the Obrajuelo N–S fault trace, and the PC geothermal well is also inferred to be located above a buried N–S fault (Fig. 1C). In Querétaro–San Juan del Río, sample LD is close to Sanfandila, a town where a seismic swarm took place in 1998 (Zúñiga et al., 2003), the Sal sample also lies close to the inferred Sanfandila fault trace, while EL lies within the intersection of the NW–SE and the NE–SW faults systems, at the rim of the Amazcala caldera (ca. 7.3 Ma; Fig. 1C). There is a clear relationship between the location of the thermally high R/Ra samples and the structural setting of the region, which implies that faults transport ${}^3\text{He}$ toward the surface, although the origin of this ${}^3\text{He}$ is not obvious.

We tested two hypotheses to assess a possible origin for the high R/Ra values within an intra-arc extension environment: (1) ${}^3\text{He}$ enrichment due to

a volatile-rich magma aging at depth (crust building by magma injection), and (2) ascent of volatiles degassed from mantle melts enhanced by crustal permeability in proximity to the regional fault systems coupled with crustal extension (Kennedy and van Soest, 2006).

Remnant Magmatic Fluids/Magma Aging Model

The magma aging model, first proposed by Torgersen and Jenkins (1982) and further developed by Kennedy and van Soest (2006) and Méjean et al. (2020), was used to test the first hypothesis. The magma aging model considers that in the absence of a present degassing magmatic source in the crust, anomalously high ${}^3\text{He}$ contribution sources could derive from the leaching of local magmatic rocks rich in ${}^3\text{He}$ trapped in the rocks (Torgersen and Jenkins, 1982; Méjean et al., 2020). To distinguish if this ${}^3\text{He}$ signature comes from the local magmatic rocks, we calculated the present-day helium composition that might be found according to their ages. In the crust, the time-dependent change in the helium isotopic composition of a reservoir due to the addition of radiogenic ${}^4\text{He}$ is described by the equation (Newell et al., 2015):

$$\left(\frac{^3\text{He}}{^4\text{He}}\right)_{\text{fin}} = \frac{\left(^3\text{He}\right)_{\text{init}}}{\left(^4\text{He}_{\text{init}} + ^4\text{He}_{\text{rad}} \times t\right)} \quad (6)$$

Where *fin* and *init* refer to the final (present-day) and initial concentrations ($\text{cm}^3\text{STP/g}$) or ratios, it is the time since the magmatic event/emplacement (yr), and ${}^4\text{He}_{\text{rad}}$ is the accumulation rate of radiogenic helium in the fluid ($\text{cm}^3\text{STP/g/yr}$) given by:

$${}^4\text{He}_{\text{rad}} = {}^4\text{He}_{\text{prod}} \times \frac{(1-\varphi)}{\varphi} \quad (7)$$

where φ is the porosity, and ${}^4\text{He}_{\text{prod}}$ is the crustal production rate ($\text{cm}^3\text{STP/g/yr}$), which can be calculated following the equation (Torgersen et al., 1995):

$${}^4\text{He}_{\text{prod}} = (0.2355 \times 10^{-12}) \times [U] \times \left(1 + 0.123 \left(\frac{[Th]}{[U]} - 4\right)\right) \quad (8)$$

where $[U]$ and $[Th]$ are the concentrations of *U* and *Th* in the rock in ppm. In absence of local representative data, we used the $[U]$ and $[Th]$ concentrations of an average continental upper crust (2.7 ppm and 10.5 ppm, respectively; Rudnick and Gao, 2003).

In agreement with the regional geology, we considered two possible sources for a rich mantellic helium: the latest volcanism in the San Juan del Río–Querétaro–Celaya area, which corresponds to the Amazcala, Amealco and Huichapan calderas (ca. 7.3–3.0 Ma; Aguirre-Díaz and López-Martínez, 2001), and the monogenetic volcanism of the Michoacán–Guanajuato volcanic field (average 300–400 ka; Gómez-Vasconcelos et al., 2020). We calculated the remaining ${}^3\text{He}/{}^4\text{He}$ ratio of the magmatic fluid without considering mixing processes using the ages of these two volcanic events. According to the helium concentration measured in olivine from the Pleistocene to present Trans-Mexican Volcanic Belt (Straub et al., 2011), we assume a ${}^4\text{He}_{\text{init}}$ value of $2.84 \times 10^{-8} \text{ cm}^3\text{STP/g}$, and a ${}^3\text{He}_{\text{init}}$ value of $2.87 \times 10^{-13} \text{ cm}^3\text{STP/g}$ for the lithospheric mantle in central Mexico. Considering that these magmatic rocks are emplaced or can interact with water within the upper crust, we used a ${}^4\text{He}_{\text{prod}}$ value of $6.27 \times 10^{-13} \text{ cm}^3\text{STP/g/yr}$. For the porosity value, we used 10% as an average in a fractured sedimentary and volcaniclastic upper crust (Carrera-Hernández et al., 2016; Alaniz-Álvarez et al., 2001).

Results using the youngest caldera's event (ca. 3.0 Ma) yield a remaining ${}^3\text{He}/{}^4\text{He}$ ratio of 1.69×10^{-8} (0.01 Ra), while the monogenetic volcanism (300 ka) yields a remaining ${}^3\text{He}/{}^4\text{He}$ ratio of 1.67×10^{-7} (0.12 Ra). The values calculated represent a maximum, as we are not considering mixing or dilution within the aquifers. Calderas (ca. 3 Ma) or monogenetic volcanic (<300 ka) sources in the upper crust for the high mantle He contribution seem unlikely. In both cases, the predicted helium composition in the remaining fluid is several orders of magnitude lower than the range of Rc/Ra ratios measured in the study area. To reach Rc/Ra values as high as 3.25, such those measured in the EL sample, and without considering aquifer dilution, the age of the magma source should be less than 6 ka. But such young magmatism is absent in the study region.

Sublithospheric Mantle He Flow through the Crust

To better asses the origin of the mantellic helium source, we estimated a travel-time range for the helium coming from the sublithospheric mantle to the surface using equations 6, 7, and 8. In this case, ${}^4\text{He}_{\text{prod}} = 2.59 \times 10^{-14} \text{ cm}^3\text{STP/g/yr}$ was calculated using concentrations of U and Th in average mid-oceanic-ridge basalt (0.119 and 0.4, respectively; Gale et al., 2013) as a proxy for the composition of the subcontinental lithospheric mantle beneath Mexico. The $({}^3\text{He}/{}^4\text{He})_{\text{fin}}$ values used were the ratios measured in San Juan del Río–Querétaro–Celaya samples, except for the Ame cold-shallow aquifer sample. The ${}^4\text{He}_{\text{init}}$ and ${}^3\text{He}_{\text{init}}$ values used remained the same (2.84×10^{-8} and $2.87 \times 10^{-13} \text{ cm}^3\text{STP/g}$, respectively; Straub et al., 2011). We consider an average crustal thickness of 40 km (Urrutia-Fucugauchi and Flores-Ruiz, 1996). As for the porosity, we used a value of $\varphi = 1\%$ as an upper limit for the lower crust (Hiett et al., 2021). Using Equation 7, we obtained He residence times of 14–300 k.y. (with an average of 80 k.y.). These residence times can be used to calculate an He flow rate. Considering a 40-km-thick crust, we have flow rates of 0.1–2.9 m/yr. Calculated ${}^3\text{He}$ flow rates are comparable to the flow rates from other active crustal fault zones such as the San Andreas fault (0.004–0.14 m/yr; Kennedy et al., 1997; Kulongsiki et al., 2013), the North Anatolian fault (0.13–0.19 m/yr; de Leeuw et al., 2010), the Karakoram fault (0.012–0.019 m/yr; Klempener et al., 2013), and the Alpine fault (0.42–2.6 m/yr; Menzies et al., 2016). Although these calculations are an approximation (and not an exact value) for the extent and rate of degassing in the San Juan del Río–Querétaro–Celaya area, they are comparable to the estimates for other regions where the mantle degassing is controlled by major crustal fault systems.

Regional Implications

The residence times calculated suggest that the partial melting event in the subcontinental sublithospheric mantle could be part of the event that created the Michoacán–Guanajuato volcanic field. The distribution of this monogenetic volcanism is strongly controlled by pre-existing, ~N–S-trending, and locally still active fault systems (Gómez-Vasconcelos et al., 2020). Although the high ${}^3\text{He}$ points to partial melting in the mantle, according to our re-evaluation of the hydrogeologic system and the dissolved gas data, there is no evidence of magmatic activity in the same range of time (< 300 k.y.).

In our study area, the distribution of the mantellic helium in the San Juan del Río–Querétaro–Celaya aquifers is strongly controlled by the permeability associated with the N–S systems of the fault. The extent of ${}^3\text{He}$ degassing seems to be different in the aquifers; for example, ${}^3\text{He}$ flow rates are higher for the dissolved gas samples in the San Juan del Río–Querétaro aquifers than for those in the Celaya aquifer (El Geyser and PC). For instance, the EL and Sal samples (from 200–300-m-deep wells, with temperatures of ~40 °C) have higher mantle helium flux than the PC sample from a 2500-m-deep geothermal production well. In general, toward the west of the San Miguel Allende–Taxco fault system, we find high-enthalpy waters (Celaya) but with a moderate mantle

helium contribution, while to the east of the San Miguel Allende–Taxco fault system, we find the thermal anomalies associated with a high input of mantle helium. The eastern portion of the San Juan del Río–Querétaro–Celaya area seems to be more permeable, which could also be related to the seismic activity in the region (Zúñiga et al., 2003; Aguirre-Díaz et al., 2005).

CONCLUSIONS

The hydrochemical and helium isotopic compositions in the study area provide insights into the dynamics of volatile degassing in the northern part of the central Trans-Mexican Volcanic Belt. The San Juan del Río–Querétaro–Celaya area, located within the intersection of two regional fault systems, contains thermal waters with a high input of ${}^3\text{He}$. The water has a meteoric origin and is not influenced by volcanic water or gas, as in other geothermal areas of the Trans-Mexican Volcanic Belt, such as Los Azufres, which is located ~70 km to the south. The high contribution of ${}^3\text{He}$ is related to the partial melting of the sublithospheric mantle, and the ascent of this mantle helium from the base of the crust to the surface is controlled by the San Miguel Allende–Taxco and Chapala–Tula regional fault systems.

Our results emphasize the importance of regional crustal fault systems as important pathways for volatile degassing in the Trans-Mexican Volcanic Belt in addition to the large volcanic centers. Additional geophysical data on the structure of the upper mantle to the north of the central Trans-Mexican Volcanic Belt, coupled with a better knowledge of the stress regime in the crust, will help to confirm the mechanism that leads to the active volatile degassing without magmatic activity observed in central Mexico.

ACKNOWLEDGMENTS

This research is part of A. Billarent-Cedillo's Master of Science project in the framework of the Universidad Nacional Autónoma de México (UNAM) postgraduate program. The research was funded by CONACYT grant CB-255070 to G. Levresse, and by the UNAM-DGAPA PAPIIT grant IV100117 (Centro de Geociencias y Facultad de Ingeniería, Hydrogeology Group, UNAM). We thank Comité Técnico de Aguas Subterráneas de San Juan del Río, and Comisión Estatal de Aguas Querétaro for sharing information and logistical support. The manuscript benefited greatly from the reviews of Daniele L. Pinti and an anonymous reviewer.

REFERENCES CITED

- Aguirre-Díaz, G.J., 1996, Volcanic stratigraphy of the Amealco caldera and vicinity, Central Mexican Volcanic Belt: *Revista Mexicana de Ciencias Geológicas*, v. 13, p. 10–51.
- Aguirre-Díaz, G.J., and López-Martínez, M., 2001, The Amazcala caldera, Querétaro, Mexico. Geology and geochronology: *Journal of Volcanology and Geothermal Research*, v. 111, p. 203–218, [https://doi.org/10.1016/S0377-0273\(01\)00227-X](https://doi.org/10.1016/S0377-0273(01)00227-X).
- Aguirre-Díaz, G.J., and López-Martínez, M., 2009, Geologic evolution of the Donguinyó–Huichapan caldera complex, central Mexican Volcanic Belt, Mexico: *Journal of Volcanology and Geothermal Research*, v. 179, p. 133–148, <https://doi.org/10.1016/j.jvolgeores.2008.10.013>.
- Aguirre-Díaz, G.J., and McDowell, F.W., 2000, Volcanic evolution of the Amealco caldera, central Mexico, in Delgado-Granados, H., Aguirre-Díaz, G.J., and Stock, J.M., eds., *Cenozoic Tectonics and Volcanism of Mexico: Geological Society of America Special Paper 334*, p. 179–193, <https://doi.org/10.1130/0-8137-2334-5.179>.
- Aguirre-Díaz, G.J., Nieto-Obregón, J., and Zúñiga, F.R., 2005, Seismogenic basin and range and intra-arc normal faulting in the central Mexican Volcanic Belt, Querétaro, México: *Geological Journal*, v. 40, p. 215–243, <https://doi.org/10.1002/gj.1004>.
- Alaniz-Álvarez, S.A., and Nieto-Samaniego, Á.F., 2005, El sistema de fallas Taxco–San Miguel de Allende y la Faja Volcánica Transmexicana, dos fronteras tectónicas del centro de México activas durante el Cenozoico: *Boletín de la Sociedad Geológica Mexicana*, v. 57, p. 65–82, <https://doi.org/10.18268/BSGM2005v57n1a4>.
- Alaniz-Álvarez, S.A., Nieto-Samaniego, Á.F., Reyes-Zaragoza, M.A., Orozco-Esquível, M.T., Ojeda-García, Á.C., and Vassallo, L.F., 2001, Estratigrafía y deformación extensional en la región San Miguel de Allende–Querétaro, México: *Revista Mexicana de Ciencias Geológicas*, v. 18, p. 129–148.
- Alaniz-Álvarez, S.A., Nieto-Samaniego, Á.F., Orozco-Esquível, M.T., Vassallo, L.F., and Xu, S., 2002, El sistema de fallas Taxco–San Miguel de Allende: Implicaciones en la deformación post-eocénica del centro de México: *Boletín de la Sociedad Geológica Mexicana*, v. 55, p. 12–29, <https://doi.org/10.18268/BSGM2002v55n1a2>.
- Alarcón-Herrera, M.T., Bundschuh, J., Nath, B., Nicoll, H.B., Gutierrez, M., Reyes-Gomez, V.M., Núñez, D., Martín-Dominguez, I.R., and Sracek, O., 2013, Co-occurrence of arsenic and fluoride in groundwater of semi-arid regions in Latin America: Genesis, mobility and remediation: *Journal of Hazardous Materials*, v. 262, p. 960–969, <https://doi.org/10.1016/j.jhazmat.2012.08.005>.
- Amézaga-Campos, B.S., Villanueva-Estrada, R., Carrillo-Chavez, A., Morales-Arredondo, J.I., and Morán-Ramírez, J., 2022, Hydrogeochemistry characterization of an overexploited municipal, agricultural, and industrial aquifer, central Mexico: *Applied Geochemistry*, v. 142, <https://doi.org/10.1016/j.apgeochem.2022.105310>.
- Aranda-Gómez, J.J., and McDowell, F.W., 1998, Paleogene extension in the southern basin and range province of Mexico: Syndepositional tilting of Eocene red beds and Oligocene volcanic rocks in the Guanajuato mining district: *International Geology Review*, v. 40, p. 116–134, <https://doi.org/10.1080/00206819809465201>.
- Arango-Guevara, A.F., Mitre-Salazar, L.M., and Martínez-Reyes, J., 2007, Actualización del conocimiento geológico en la Cuenca del Río Chichimequillas, Estado de Querétaro, México ANDRÉS: Trabajos de Geología 27, Universidad de Oviedo, p. 29–39.
- Arce, J.L., Rangel, E., Valdez-Moreno, G., Saucedo, R., Castro-Govea, R., and Macías, J.L., 2021, Caracterización geoquímica, petrográfica y evolución magmática del Campo Volcánico de Los Azufres, Michoacán, durante el Pleistoceno: *Revista Mexicana de Ciencias Geológicas*, v. 38, p. 122–140, <https://doi.org/10.22201/cgeo.20072902e.2021.2.1646>.
- Ballentine, C.J., and Burnard, P.G., 2002, Production, release and transport of noble gases in the continental crust: *Reviews in Mineralogy and Geochemistry*, v. 47, p. 481–538, <https://doi.org/10.2138/rmg.2002.47.12>.
- Ballentine, C.J., Marty, B., Lollar, B.S., and Cassidy, M., 2005, Neon isotopes constrain convection and volatile origin in the Earth's mantle: *Nature*, v. 433, p. 33–38, <https://doi.org/10.1038/nature03182>.
- Barragán, R.M., Arellano, V.M., Portugal, E., and Sandoval, F., 2005, Isotopic ($\delta^{18}\text{O}$, δD) patterns in Los Azufres (México) geothermal fluids related to reservoir exploitation: *Geothermics*, v. 34, p. 527–547.
- Bekaert, D.V., Turner, S.J., Broadley, M.W., Barnes, J.D., Halldoacutersson, S.A., Labidi, J., Wade, J., Walowski, K.J., and Barry, P.H., 2021, Subduction-driven volatile recycling: A global mass balance: *Annual Review of Earth and Planetary Sciences*, v. 49, p. 37–70, <https://doi.org/10.1146/annurev-earth-071620-055024>.
- Benson, B.B., and Krause, D., 1980, Isotopic fractionation of helium during solution: A probe for the liquid state: *Journal of Solution Chemistry*, v. 9, p. 895–909, <https://doi.org/10.1007/BF00646402>.
- Botero-Santa, P.A., Alaniz-Álvarez, S.A., Nieto-Samaniego, Á.F., López-Martínez, M., Levresse, G., Xu, S., and Ortega-Obregón, C., 2015, Origen y desarrollo de la cuenca El Bajío en el sector central de la faja Volcánica Transmexicana: *Revista Mexicana de Ciencias Geológicas*, v. 32, p. 84–98.
- Buttitta, D., Caracausi, A., Chiaramuce, L., Favara, R., Gasparo Morticelli, M., and Sulli, A., 2020, Continental degassing of helium in an active tectonic setting (northern Italy): The role of seismicity: *Scientific Reports*, v. 10, p. 1–13, <https://doi.org/10.1038/s41598-019-55678-7>.
- Byerlee, J., 1993, Model for episodic flow of high-pressure water in fault zones before earthquakes: *Geology*, v. 21, p. 303–306, [https://doi.org/10.1130/0091-7613\(1993\)021<0303:MFEFOH>2.3.CO;2](https://doi.org/10.1130/0091-7613(1993)021<0303:MFEFOH>2.3.CO;2).
- Capasso, G., and Inguaggiato, S., 1998, A simple method for the determination of dissolved gases in natural waters. An application to thermal waters from Vulcano Island: *Applied Geochemistry*, v. 13, p. 631–642, [https://doi.org/10.1016/S0883-2927\(97\)00109-1](https://doi.org/10.1016/S0883-2927(97)00109-1).
- Carrera-Hernández, J.J., Carreón-Freyre, D., Cerca-Martínez, M., and Levresse, G., 2016, Groundwater flow in a transboundary fault-dominated aquifer and the importance of regional modeling:

- The case of the city of Querétaro, Mexico: *Hydrogeology Journal*, v. 24, p. 373–393, <https://doi.org/10.1007/s10040-015-1363-x>.
- Craig, H., Lupton, J.E., Welhan, J.A., and Poreda, R., 1978, Helium isotope ratios in Yellowstone and Lassen Park volcanic gases: *Geophysical Research Letters*, v. 5, p. 897–900, <https://doi.org/10.1029/GL005i011p00897>.
- Dávalos-Alvarez, O.G., Nieto-Samaniego, A.F., Alaniz-Alvarez, S.A., and Gómez-González, J.M., 2005, Las fases de deformación cenozoica en la región de Huimilpan, Querétaro, y su relación con la sismicidad local: *Revista Mexicana de Ciencias Geológicas*, v. 22, p. 129–147.
- de Leeuw, G.A.M., Hilton, D.R., Güleç, N., and Mutlu, H., 2010, Regional and temporal variations in CO_2/He , $^3\text{He}/^4\text{He}$ and $\delta^{13}\text{C}$ along the North Anatolian Fault Zone, Turkey: *Applied Geochemistry*, v. 25, p. 524–539, <https://doi.org/10.1016/j.apgeochem.2010.01.010>.
- Del Pilar-Martínez, A., Nieto-Samaniego, A.F., Alaniz-Alvarez, S.A., and Angeles-Moreno, E., 2020, Geology of the southern Mesa Central of Mexico: Recording the beginning of a polymodal fault system: *Journal of Maps*, v. 16, p. 199–211, <https://doi.org/10.1080/17445647.2020.1719911>.
- Ferrari, L., Garduño, V.H., Pasquaré, G., and Tibaldi, A., 1991, Geology of Los Azufres caldera, Mexico, and its relationships with regional tectonics: *Journal of Volcanology and Geothermal Research*, v. 47, p. 129–148, [https://doi.org/10.1016/0377-0273\(91\)90105-9](https://doi.org/10.1016/0377-0273(91)90105-9).
- Ferrari, L., Orozco-Esquível, T., Manea, V., and Manea, M., 2012, The dynamic history of the Trans-Mexican Volcanic Belt and the Mexico subduction zone: *Tectonophysics*, v. 522–523, p. 122–149, <https://doi.org/10.1016/j.tecto.2011.09.018>.
- Ferrari, L., Orozco-Esquível, T., Bryan, S.E., López-Martínez, M., and Silva-Fragoso, A., 2018, Cenozoic magmatism and extension in western Mexico: Linking the Sierra Madre Occidental silicic large igneous province and the Comondú Group with the Gulf of California rift: *Earth-Science Reviews*, v. 183, p. 115–152, <https://doi.org/10.1016/j.earscirev.2017.04.006>.
- Fitz-Díaz, E., Lawton, T.F., Juárez-Arriaga, E., and Chávez-Cabello, G., 2018, The Cretaceous-Paleogene Mexican orogen: Structure, basin development, magmatism and tectonics: *Earth-Science Reviews*, v. 183, p. 56–84, <https://doi.org/10.1016/j.earscirev.2017.03.002>.
- Gale, A., Dalton, C.A., Langmuir, C.H., Su, Y., and Schilling, J.G., 2013, The mean composition of ocean ridge basalts: *Geochemistry, Geophysics, Geosystems*, v. 14, p. 489–518, <https://doi.org/10.1029/2012GC004334>.
- Gautheron, C., and Moreira, M., 2002, Helium signature of the subcontinental lithospheric mantle: *Earth and Planetary Science Letters*, v. 199, p. 39–47, [https://doi.org/10.1016/S0012-821X\(02\)00563-0](https://doi.org/10.1016/S0012-821X(02)00563-0).
- Giggenbach, W.F., Sano, Y., and Wakita, H., 1993, Isotopic composition of helium, and CO_2 and CH_4 contents in gases produced along the New Zealand part of a convergent plate boundary: *Geochimica et Cosmochimica Acta*, v. 57, p. 3427–3455, [https://doi.org/10.1016/0016-7037\(93\)90549-C](https://doi.org/10.1016/0016-7037(93)90549-C).
- Gómez-Tuena, A., Orozco-Esquível, M.T., and Ferrari, L., 2005, Petrogénésis ígnea de la Faja Volcánica Transmexicana: Boletín de la Sociedad Geológica Mexicana, v. 3, p. 227–283, [http://www.scielo.org.mx/pdf/bsgm/v57n3/1405-3322-bsgm-57-03-227-s1.pdf%OAhttp://www.geociencias.unam.mx/~alaniz/SGM/Centenario/57-3/\(2\)Gomez.pdf](http://www.scielo.org.mx/pdf/bsgm/v57n3/1405-3322-bsgm-57-03-227-s1.pdf%OAhttp://www.geociencias.unam.mx/~alaniz/SGM/Centenario/57-3/(2)Gomez.pdf).
- Gómez-Vasconcelos, M.G., Macías, J.L., Ramón Avellán, D.R., Sosa-Ceballos, G., Garduño-Monroy, V.H., Cisneros-Máximo, G., Layer, P.W., Benowitz, J., López-Loera, H., Mendiola López, F.M., and Perton, M., 2020, The control of preexisting faults on the distribution, morphology, and volume of monogenetic volcanism in the Michoacán-Guanajuato Volcanic Field: *Geological Society of America Bulletin*, v. 132, p. 2455–2474, <https://doi.org/10.1130/B35397.1>.
- González-Guzmán, R., Inguaggiato, C., Peiffer, L., Weber, B., and Kretzschmar, T., 2019, Fault-controlled geothermal fluids of the northern Trans-Mexican Volcanic Belt: A geochemical and isotopic study of the Los Geysers field (Valley of Querétaro, Mexico): *Journal of Volcanology and Geothermal Research*, v. 388, <https://doi.org/10.1016/j.jvolgeores.2019.106681>.
- González-Partida, E., Carrillo-Chávez, A., Levresse, G., Tello-Hinojosa, E., Venegas-Salgado, S., Ramírez-Silva, G., Pal-Verma, M., Tritlla, J., and Camprubi, A., 2005, Hydro-geochemical and isotopic fluid evolution of the Los Azufres geothermal field, Central Mexico: *Applied Geochemistry*, v. 20, p. 23–39, <https://doi.org/10.1016/j.apgeochem.2004.07.006>.
- Graham, D.W., 2002, Noble gas isotope geochemistry of mid-ocean ridge and ocean island basalts: Characterization of mantle source reservoirs: *Reviews in Mineralogy and Geochemistry*, v. 47, p. 247–317, <https://doi.org/10.2138/rmg.2002.478>.
- Hasenaka, T., 1994, Size, distribution, and magma output rate for shield volcanoes of the Michoacán-Guanajuato volcanic field, Central Mexico: *Journal of Volcanology and Geothermal Research*, v. 63, p. 13–31, [https://doi.org/10.1016/0377-0273\(94\)90016-7](https://doi.org/10.1016/0377-0273(94)90016-7).
- Hasenaka, T., and Carmichael, I.S.E., 1985, The cinder cones of Michoacán-Guanajuato, central Mexico: Their age, volume and distribution, and magma discharge rate: *Journal of Volcanology and Geothermal Research*, v. 25, p. 105–124, [https://doi.org/10.1016/0377-0273\(85\)90007-1](https://doi.org/10.1016/0377-0273(85)90007-1).
- Hernández-Pérez, E., Levresse, G., Carrera-Hernández, J., and García-Martínez, R., 2020, Short term evaporation estimation in a natural semiarid environment: New perspective of the Craig–Gordon isotopic model: *Journal of Hydrology*, v. 587, <https://doi.org/10.1016/j.jhydrol.2020.124926>.
- Hernández-Pérez, E., Levresse, G., Carrera-Hernández, J., Inguaggiato, C., Vega-González, M., Corbo-Camargo, F., Carreón-Freyre, D.C., Billarent-Cedillo, A., Contreras, F.J.S., and Hernández, C.P.R., 2022, Geochemical and isotopic multi-tracing ($\delta^{18}\text{O}$, $\delta^2\text{H}$, $\delta^{13}\text{C}$, $\Delta^{14}\text{C}$) of groundwater flow dynamics and mixing patterns in the volcanoclastic aquifer of the semiarid San Juan del Río Basin in central Mexico: *Hydrogeology Journal*, v. 30, p. 2073–2095.
- Hiett, C.D., Newell, D.L., and Jessup, M.J., 2021, ^3He evidence for fluid transfer and continental hydration above a flat slab: *Earth and Planetary Science Letters*, v. 556, <https://doi.org/10.1016/j.epsl.2020.116722>.
- Hilton, D.R., 1996, The helium and carbon isotope systematics of a continental geothermal system: Results from monitoring studies at Long Valley caldera (California, U.S.A.): *Chemical Geology*, v. 127, p. 269–295, [https://doi.org/10.1016/0009-2541\(95\)00134-4](https://doi.org/10.1016/0009-2541(95)00134-4).
- Hilton, D.R., 2007, Geochemistry: The leaking mantle: *Science*, v. 318, p. 1389–1390, <https://doi.org/10.1126/science.1151983>.
- Hilton, D.R., and Porcelli, D., 2014, 3.7—Noble gases as mantle tracers, in Holland, H.D., and Turekian, K.K., eds., *Treatise on Geochemistry* (2nd edition), Volume 3: Elsevier, p. 293–325, <https://doi.org/10.1016/B978-0-08-095975-7.00217-5>.
- Hilton, D.R., Fischer, T.P., and Marry, B., 2002, Noble gases and volatile recycling at subduction zones: *Reviews in Mineralogy and Geochemistry*, v. 47, p. 319–370, <https://doi.org/10.2138/rmg.2002.479>.
- Hooker, P.J., Bertrami, R., Lombardi, S., O’Nions, R.K., and Oxburgh, E.R., 1985, Helium-3 anomalies and crust-mantle interaction in Italy: *Geochimica et Cosmochimica Acta*, v. 49, p. 2505–2513, [https://doi.org/10.1016/0016-7037\(85\)90118-8](https://doi.org/10.1016/0016-7037(85)90118-8).
- Husker, A., and Davis, P.M., 2009, Tomography and thermal state of the Cocos Plate subduction beneath Mexico City: *Journal of Geophysical Research: Solid Earth*, v. 114, <https://doi.org/10.1029/2008JB006039>.
- Inguaggiato, S., and Rizzo, A., 2004, Dissolved helium isotope ratios in ground-waters: A new technique based on gas-water re-equilibration and its application to Stromboli volcanic system: *Applied Geochemistry*, v. 19, p. 665–673, <https://doi.org/10.1016/j.apgeochem.2003.10.009>.
- Jácome-Paz, M.P., 2019, Two new geothermal prospects in the Mexican Volcanic Belt: La Escalera and Agua Caliente-Tzitzio geothermal springs, Michoacán, México: *Geothermics*, v. 80, p. 44–55, <https://doi.org/10.1016/j.geothermics.2019.02.004>.
- Kennedy, B.M., and van Soest, M.C., 2006, A helium isotope perspective on the Dixie Valley, Nevada, hydrothermal system: *Geothermics*, v. 35, p. 26–43, <https://doi.org/10.1016/j.geothermics.2005.09.004>.
- Kennedy, B.M., and van Soest, M.C., 2007, Flow of mantle fluids through the ductile lower crust: Helium isotope trends: *Science*, v. 318, p. 1433–1436, <https://doi.org/10.1126/science.1147537>.
- Kennedy, B.M., Kharaka, Y.K., Evans, W.C., Ellwood, A., DePaolo, D.J., Thordesen, J., Ambats, G., and Mariner, R.H., 1997, Mantle fluids in the San Andreas Fault system, California: *Science*, v. 278, p. 1278–1281, <https://doi.org/10.1126/science.278.5341.1278>.
- Kim, Y., Clayton, R.W., and Jackson, J.M., 2010, Geometry and seismic properties of the subducting Cocos Plate in central Mexico: *Journal of Geophysical Research: Solid Earth*, v. 115, B06310, <https://doi.org/10.1029/2009JB006942>.
- Klemperer, S.L., Kennedy, B.M., Sastry, S.R., Makovsky, Y., Harinayana, T., and Leech, M.L., 2013, Mantle fluids in the Karakoram Fault: Helium isotope evidence: *Earth and Planetary Science Letters*, v. 366, p. 59–70, <https://doi.org/10.1016/j.epsl.2013.01.013>.
- Kulongoski, J.T., Hilton, D.R., and Izicki, J.A., 2005, Source and movement of helium in the eastern Morongo groundwater basin: The influence of regional tectonics on crustal and mantle helium fluxes: *Geochimica et Cosmochimica Acta*, v. 69, p. 3857–3872, <https://doi.org/10.1016/j.gca.2005.03.001>.
- Kulongoski, J.T., Hilton, D.R., Barry, P.H., Esser, B.K., Hillebrand, D., and Belitz, K., 2013, Volatile fluxes through the Big Bend section of the San Andreas Fault, California: Helium and carbon-dioxide systematics: *Chemical Geology*, v. 339, p. 92–102, <https://doi.org/10.1016/j.chemgeo.2012.09.007>.
- López-Alvís, J., Carrera-Hernández, J.J., Levresse, G., and Nieto-Samaniego, A.F., 2019, Assessment of groundwater depletion caused by excessive extraction through groundwater flow modeling: The Celaya aquifer in central Mexico: *Environmental Earth Sciences*, v. 78, p. 1–22, <https://doi.org/10.1007/s12665-019-8497-4>.
- Luhr, J.F., Kimberly, P., Siebert, L., Jorge Aranda-Gómez, J., Housh, T.B., and Mattiotti, G.K., 2006, México’s Quaternary volcanic rocks: Insights from the MEXPET petrological and geochemical

- database, in Siebe, C., MarciasGerardo, J.L., and Aguirre-Díaz, J., eds., Neogene–Quaternary Continental Margin Volcanism: A Perspective from México: Geological Society of America Special Paper 402, p. 1–44, [https://doi.org/10.1130/2006.2402\(01\)](https://doi.org/10.1130/2006.2402(01)).
- Mamyrin, B.A., and Tolstikhin, I.N., eds., 1984, Helium Isotopes in Nature: Developments in Geochemistry: Elsevier, v. 3, 273 p., <https://doi.org/10.1016/B978-0-444-42180-7.50003-X>.
- Marín-Camacho, P., Velasco-Tapia, F., Bernard-Romero, R., Weber, B., and González-Guzmán, R., 2022, New geochemical evidence constraining the water-rock-gas interaction on geothermal fluids of the Querétaro Graben, northern Trans-Mexican Volcanic Belt: Journal of South American Earth Sciences, v. 114, <https://doi.org/10.1016/j.jsames.2021.103702>.
- Méjean, P., Pinti, D.L., Kagoshima, T., Roulleau, E., Demarets, L., Poirier, A., Takahata, N., Sano, Y., and Larocque, M., 2020, Mantle helium in Southern Quebec groundwater: A possible fossil record of the New England hotspot: Earth and Planetary Science Letters, v. 545, <https://doi.org/10.1016/j.epsl.2020.116352>.
- Menzies, C.D., Teagle, D.A.H., Niedermann, S., Cox, S.C., Craw, D., Zimmer, M., Cooper, M.J., and Erzinger, J., 2016, The fluid budget of a continental plate boundary fault: Quantification from the Alpine Fault, New Zealand: Earth and Planetary Science Letters, v. 445, p. 125–135, <https://doi.org/10.1016/j.epsl.2016.03.046>.
- Morales-Arredondo, J.I., Armienta Hernández, M.A., Ortega-Gutiérrez, J.E., Flores-Ocampo, I.Z., and Flores-Vargas, R., 2020, Evaluation of the carbon dioxide behavior in a thermal aquifer located at Central Mexico and its relation to silicate weathering: International Journal of Environmental Science and Technology, v. 17, p. 3411–3430, <https://doi.org/10.1007/s13762-020-02683-3>.
- Newell, D.L., Jessup, M.J., Hilton, D.R., Shaw, C.A., and Hughes, C.A., 2015, Mantle-derived helium in hot springs of the Cordillera Blanca, Peru: Implications for mantle-to-crust fluid transfer in a flat-slab subduction setting: Chemical Geology, v. 417, p. 200–209, <https://doi.org/10.1016/j.chemgeo.2015.10.003>.
- Nicolli, H.B., Bundschuh, J., Blanco, M. del C., Tujchneider, O.C., Panarello, H.O., Dapeña, C., and Rusansky, J.E., 2012, Arsenic and associated trace-elements in groundwater from the Chaco-Pampean plain, Argentina: Results from 100 years of research: The Science of the Total Environment, v. 429, p. 36–56, <https://doi.org/10.1016/j.scitotenv.2012.04.048>.
- Nieto-Samaniego, Á.F., Ferrari, L., Alaniz-Alvarez, S.A., Labarthe-Hernández, G., and Rosas-Elguera, J., 1999, Variation of Cenozoic extension and volcanism across the southern Sierra Madre Occidental volcanic province, Mexico: Bulletin of the Geological Society of America, v. 111, p. 347–363, [https://doi.org/10.1130/0016-7606\(1999\)111<0347:VOCEAV>2.3.CO;2](https://doi.org/10.1130/0016-7606(1999)111<0347:VOCEAV>2.3.CO;2).
- Nieva, D., Verma, M., Santoyo, E., Barragán, R.M., Portugal, E., Ortiz, J., and Quijano, L., 1987, Chemical and isotopic evidence of steam upflow and partial condensation in Los Azufres Reservoir: Proceedings of 12th Workshop on Geothermal Reservoir Engineering Stanford University, Stanford, CA, 20–22 January 1987, p. 253–259.
- Ochoa-González, G.H., Carreón-Freyre, D., Cerca, M., and López-Martínez, M., 2015, Assessment of groundwater flow in volcanic faulted areas. A study case in Querétaro, Mexico: Geofísica Internacional, v. 54, p. 199–220, <https://doi.org/10.1016/j.gi.2015.04.016>.
- O’Nions, R.K., and Oxburgh, E.R., 1988, Helium, volatile fluxes and the development of continental crust: Earth and Planetary Science Letters, v. 90, p. 331–347, [https://doi.org/10.1016/0012-821X\(88\)90134-3](https://doi.org/10.1016/0012-821X(88)90134-3).
- Palacios-García, N.B., and Martini, M., 2014, From back-arc rifting to arc accretion: The Late Jurassic-Early Cretaceous evolution of the Guerrero terrane recorded by a major provenance change in sandstones from the Sierra de los Cuarzos area, central Mexico: International Geology Review, v. 56, p. 1377–1394, <https://doi.org/10.1080/00206814.2014.938367>.
- Pérez-Campos, X., Kim, Y., Husker, A., Davis, P.M., Clayton, R.W., Iglesias, A., Pacheco, J.F., Singh, S.K., Manea, V.C., and Gurnis, M., 2008, Horizontal subduction and truncation of the Cocos Plate beneath central Mexico: Geophysical Research Letters, v. 35, L18303, <https://doi.org/10.1029/2008GL035127>.
- Pérez-Martínez, I., Villanueva-Estrada, R.E., Cardona-Benavides, A., Rodríguez-Díaz, A.A., Rodríguez-Salazar, M.T., and Guadalupe, J., 2020, Hydrogeochemical reconnaissance of the Atotonilco el Alto–Santa Rita geothermal system in the northeastern Chapala graben in Mexico: Geothermics, v. 83, <https://doi.org/10.1016/j.geothermics.2019.101733>.
- Pérez-Venzor, J.A., Aranda-Gómez, J.J., McDowell, F., and Solorio-Munguía, J.G., 1996, Geología del volcán Palo Huérano, Guanajuato, México: Revista Mexicana de Ciencias Geológicas, v. 13, p. 174–183.
- Pinti, D.L., Castro, M.C., Shouakar-Stash, O., Tremblay, A., Garduño, V.H., Hall, C.M., Hélie, J.F., and Ghaleb, B., 2013, Evolution of the geothermal fluids at Los Azufres, Mexico, as traced by noble gas isotopes, $\delta^{18}\text{O}$, δD , $\delta^{13}\text{C}$ and $^{87}\text{Sr}/^{86}\text{Sr}$: Journal of Volcanology and Geothermal Research, v. 249, p. 1–11, <https://doi.org/10.1016/j.jvolgeores.2012.09.006>.
- Plank, T., Kelley, K.A., Zimmer, M.M., Hauri, E.H., and Wallace, P.J., 2013, Why do mafic arc magmas contain ~4 wt% water on average?: Earth and Planetary Science Letters, v. 364, p. 168–179, <https://doi.org/10.1016/j.epsl.2012.11.044>.
- Ray, M.C., Hilton, D.R., Muñoz, J., Fischer, T.P., and Shaw, A.M., 2009, The effects of volatile recycling, degassing and crustal contamination on the helium and carbon geochemistry of hydrothermal fluids from the Southern Volcanic Zone of Chile: Chemical Geology, v. 266, p. 38–49, <https://doi.org/10.1016/j.chemgeo.2008.12.026>.
- Rizzo, A.L., Barberi, F., Carapezza, M.L., Di Piazza, A., Francalanci, L., Sortino, F., and D’Alessandro, W., 2015, New mafic magma refilling a quiescent volcano: Evidence from He-Ne-Ar isotopes during the 2011–2012 unrest at Santorini, Greece: Geochemistry, Geophysics, Geosystems, v. 16, p. 798–814, <https://doi.org/10.1002/2014GC005653>.
- Rudnick, R.L., and Gao, S., 2003, The composition of the continental crust, in Holland, H.D., and Turekian, K.K., eds., Treatise on Geochemistry, Vol. 3, The Crust: Oxford, UK, Elsevier-Pergamon, p. 1–64, <http://doi.org/10.1016/b0-08-043751-6/03016-4>.
- Sano, Y., and Wakita, H., 1985, Geographical distribution of $^{3}\text{He}/^{4}\text{He}$ ratios in Japan: implications for arc tectonics and incipient magmatism: Journal of Geophysical Research: Solid Earth, v. 90, p. 8729–8741, <https://doi.org/10.1029/JB090iB10p08729>.
- Shaw, D.M., and Sturchio, N.C., 1992, Boron-lithium relationships in rhyolites and associated thermal waters of young silicic calderas, with comments on incompatible element behaviour: Geochimica et Cosmochimica Acta, v. 56, p. 3723–3731, [https://doi.org/10.1016/0016-7037\(92\)90165-F](https://doi.org/10.1016/0016-7037(92)90165-F).
- Smith, S.P., and Kennedy, B.M., 1983, The solubility of noble gases in water and in NaCl brine: Geochimica et Cosmochimica Acta, v. 47, p. 503–515, [https://doi.org/10.1016/0016-7037\(83\)90273-9](https://doi.org/10.1016/0016-7037(83)90273-9).
- Straub, S.M., Gomez-Tuena, A., Stuart, J., Zellmer, G.F., Espinasa-Perena, R., Cai, Y., and Izuka, Y., 2011, Formation of hybrid arc andesites beneath thick continental crust: Earth and Planetary Science Letters, v. 303, p. 337–347, <https://doi.org/10.1016/j.epsl.2011.01.013>.
- Tardani, D., et al., 2016, Exploring the structural controls on helium, nitrogen and carbon isotope signatures in hydrothermal fluids along an intra-arc fault system: Geochimica et Cosmochimica Acta, v. 184, p. 193–211, <https://doi.org/10.1016/j.gca.2016.04.031>.
- Tolstikhin, I.N., and Marty, B., 1998, The evolution of terrestrial volatiles: A view from helium, neon, argon and nitrogen isotope modelling: Chemical Geology, v. 147, p. 27–52, [https://doi.org/10.1016/S0009-2541\(97\)00170-8](https://doi.org/10.1016/S0009-2541(97)00170-8).
- Torgersen, T., 1993, Defining the role of magmatism in extensional tectonics: Helium 3 fluxes in extensional basins: Journal of Geophysical Research: Solid Earth, v. 98, p. 16,257–16,269, <https://doi.org/10.1029/93JB00891>.
- Torgersen, T., and Jenkins, W.J., 1982, Helium isotopes in geothermal systems: Iceland, The Geysers, Raft River and Steamboat Springs: Geochimica et Cosmochimica Acta, v. 46, p. 739–748, [https://doi.org/10.1016/0016-7037\(82\)90025-4](https://doi.org/10.1016/0016-7037(82)90025-4).
- Torgersen, T., Drenkard, S., State, M., Schlosser, P., and Shapiro, A., 1995, Mantle helium in ground waters of eastern North America: Time and space constraints on sources: Geology, v. 23, p. 675–678, [https://doi.org/10.1130/0091-7613\(1995\)023<0675:MHIGWO>2.3.CO;2](https://doi.org/10.1130/0091-7613(1995)023<0675:MHIGWO>2.3.CO;2).
- Urrutia-Fucugauchi, J., and Flores-Ruiz, J.H., 1996, Bouguer gravity anomalies and regional crustal structure in central Mexico: International Geology Review, v. 38, p. 176–194, <https://doi.org/10.1080/00206819709465330>.
- Valdez-Moreno, G., Aguirre-Díaz, G.J., and López-Martínez, M., 1998, El volcán La Joya, Estados de Querétaro y Guanajuato—Un Estratovolcán miocénico del Cinturón Volcánico Mexicano: Revista Mexicana de Ciencias Geológicas, v. 15, p. 181–197.
- Verma, S.P., and Carrasco-Núñez, G., 2003, Reappraisal of the geology and geochemistry of Volcán Zamorano, central Mexico: Implications for discriminating the Sierra Madre Occidental and Mexican Volcanic belt provinces: International Geology Review, v. 45, p. 724–752, <https://doi.org/10.2747/0020-6814.45.8.724>.
- Wen, T., Pinti, D.L., Castro, M.C., López-Hernández, A., Hall, C.M., Shouakar-Stash, O., and Sandoval-Medina, F., 2018, A noble gas and $^{87}\text{Sr}/^{86}\text{Sr}$ study in fluids of the Los Azufres geothermal field, Mexico—Assessing impact of exploitation and constraining heat sources: Chemical Geology, v. 483, p. 426–441, <https://doi.org/10.1016/j.chemgeo.2018.03.010>.
- Yardley, B.W.D., and Bodnar, R.J., 2014, Fluids in the Continental Crust: Geochemical Perspectives, v. 3, p. 1–125, <https://doi.org/10.7185/geochempersp.3.1>.
- Zúñiga, F.R., Pacheco, J.F., Guzmán-Speziale, M., Aguirre-Díaz, G.J., Espíndola, V.H., and Nava, E., 2003, The Sanfandila earthquake sequence of 1998, Querétaro, México: Activation of an undocumented fault in the northern edge of central Trans-Mexican Volcanic Belt: Tectonophysics, v. 361, p. 229–238, [https://doi.org/10.1016/S0040-1951\(02\)00606-6](https://doi.org/10.1016/S0040-1951(02)00606-6).

Capítulo V :

Conclusiones

Este trabajo presenta el desarrollo de un modelo hidrogeológico integral y multidisciplinario que permite entender las condiciones y procesos atmosféricas, hidrogeológicos, hidráulicos de la cuenca de San Juan del Río. Por lograr esta meta identificamos los diferentes reservorios involucrados y sus interacciones y cuantificamos las aportaciones y áreas de recarga hacia el acuífero del Valle de San Juan del Río.

La integración de los datos geológico y geofísico en un modelo conceptual permite comprender las características y geometría del medio confinante (acuífero) e identificar las áreas y vías de recargas principales (falla). Por otra parte, la integración de los modelos hidrogeoquímico e isotópico mediante la estadística permiten conocer la dinámica y procesos del medio confinado (agua subterránea). Esta visión integral y multidisciplinaria de un sistema hidrológico constituye un nuevo acercamiento a los sistemas hídricos-hidrogeológicos en acuíferos complejos en el Centro de México.

5.1. Modelo isotópico de la Cuenca del Río San Juan.

La caracterización sistemática de las firmas isotópicas del agua en el ciclo hidrológico proporciona un marco integral para resolver de manera confiable el modelo isotópico Craig y Gordon. Se establece el primer marco isotópico a escala de cuenca como guía para la interpretación y el monitoreo de las firmas isotópicas de aguas superficiales en México. Los resultados arrojan tasas de evaporación con

una extrema variación estacional y en la cual el proceso de evaporación no se encuentra correctamente representado como un modelo matemático de comportamiento lineal. Los resultados de evaporación del modelo isotópico Craig y Gordon es representativo únicamente cuando no hay aportes de otras fuentes de agua. Ya que la lluvia, cambios en el vapor atmosférico y/o el agua subterránea perturban las variaciones isotópicas en el sistema hidrológico. La comparativa entre los modelos isotópicos y físicos no son comparables ya que su fundamento teórico no es análogo. Sin embargo, los enfoques son complementarios y útiles en la comprensión del significado del "proceso de evaporación" en una cuenca hidrológica.

5.2. Modelo Hidrogeológico del AVSJR.

Este trabajo presenta el primer intento de descifrar la dinámica del flujo de agua subterránea de la cuenca de San Juan del Río. Esta caracterización se realiza a través de la integración de métodos geofísicos, geoquímicos e isotópicos que en conjunto con análisis estadísticos multivariados y un modelo de mezcla (PCA) se utiliza para determinar los patrones de mezcla de diferentes fuentes de recarga en la cuenca. La integración de estas metodologías revela la dinámica del flujo subterráneo en la cuenca del AVSJR. El agrupamiento y clasificación eucladiana en conjunto con la isotopía de $\delta^2\text{H}$, $\delta^{18}\text{O}$ y $\delta^{13}\text{C}$ confirma la identificación de los Miembros Terminales en las fuentes de recarga. Los fechamientos por $\Delta^{14}\text{C}$ permite estimar las edades de residencia en el acuífero granular somero. Se construyó un modelo hidrogeológico conceptual de flujo de agua subterránea para el acuífero de San Juan del Río. La recarga local reciente se encuentra asociada a procesos de percolación del agua meteórica y se identifica como el componente A. La recarga por el componente A ocurre en altitudes de $\approx 2,113$ msnm en las Sierras circundantes y a través de escorrentías y presas de regulación en el valle. La recarga por aguas hidrotermales se identifica como el componente C y se encuentra asociada a procesos de flujo vertical ascendente a lo largo del sistema

de fallas N-S (TSMA) representadas localmente por las fallas San Fandila y Ópalo. Los parámetros de SDT, Cl⁻, Na⁺, F⁻ y Li⁺ son los principales indicadores hidrogeoquímico para la recarga del componente C. El agua de pozos poco profundos enriquecidos con SO₄²⁻ y NO₃⁻ se asocia con el componente A y representa la recarga por retorno de riego agrícola. De acuerdo con el modelo de mezcla PCA, la proporción del componente A (agua meteórica) domina la composición del agua subterránea (hasta un 60%), por otra parte, el componente C (agua hidrotermal) presenta composiciones de entre 2% a 12%. El componente C controla la variación global de la mezcla y las características fisicoquímicas en el agua subterránea. La identificación del componente C es esencial que actualmente no se considera en los balances hídricos clásicos. El modelo de mezcla PCA es una herramienta poderosa para evaluar las proporciones de mezcla de las aguas de referencia seleccionadas presentes en los acuíferos e ilustrar su dinámica interna.

Estos resultados son importantes para establecer una política pública de preservación de las áreas de recargas en la Sierras de Vaquerías Huimilpan y Ópalos, y control/monitorio de la extracción de las reservas en las áreas más sensibles del acuífero, como el acuífero colgado, y las zonas agrícolas. El balance de mezcla en los porcentajes de Componentes (meteórica/acuífero/ hidrotermal) en cada sitio de extracción contribuye a tener una mejor visión sobre las consecuencias de la sobreexplotación y/o sequía. Los descensos de los niveles piezométricos tendrán un impacto directo sobre la baja de calidad del agua y el incremento de las anomalías térmicas por el incremento en la proporción del componente hidrotermal en la recarga de agua subterránea.

5.3. Fuente de hidrotermalismo en la cuenca de SJR

La cuenca de SJR y sus áreas circundantes (SJR-Qro-Cel) se ubican dentro de la intersección entre dos sistemas de fallas tectónicas regionales, los sistemas de fallas Taxco-San Miguel de Allende y Chapala-Tula. El agua subterránea del acuífero de SJR presenta una recarga por fluidos hidrotermales que puede ser significativa (hasta 12%). Estos fluidos tienen un origen meteórico y no está influenciada por agua connata o aportes magmáticos, tal como sucede en otras áreas geotérmicas de la TMVB, en específico en el campo geotérmico de Los Azufres, ubicada ~ 70 km al sur. Las concentraciones de gases disueltos, así como las relaciones isotópicas de helio indican que la fuente principal del helio disuelto en los acuíferos de SJR se encuentra relacionada con el derretimiento parcial del manto sublitosférico. El ascenso de helio proveniente de este manto desde la base de la corteza hasta la superficie está controlado por los sistemas de fallas regionales Taxco-San Miguel de Allende.

REFERENCIAS

- A.L., R., Barberi, M. L., Carapezza, A., Di Piazza, A., Francalanci, L., Sortino, F., & W., D. (2015). New mafic magma refilling a quiescent volcano: Evidence from He-Ne-Ar isotopes during the 2011–2012 unrest at Santorini, Greece. *Geochemistry Geophysics Geosystems*, 16(3), 798–814. <https://doi.org/10.1002/2014GC005653>
- Aguirre-Díaz, G. J. (1995). La Toba Amealco Y Su Correlación Con La Formación Las Américas a través del graben de Acambay y Estados de México, Michoacán y Querétaro, México. *Revista Mexicana de Ciencias Geológicas*, 12(1), 17–21.
- Aguirre-Díaz, G. J. (1996b). Volcanic Stratigraphy of the Amealco Caldera and Vicinity, Central Mexican Volcanic Belt. *Revista Mexicana de Ciencias Geológicas*, 13(1), 10–51.
- Aguirre-Díaz, G. J., & López-Martínez, M. (2001). The Amazcala caldera, Querétaro, México. Geology and geochronology. *Journal of Volcanology and Geothermal Research*, 111(1–4), 203–218. [https://doi.org/10.1016/S0377-0273\(01\)00227-X](https://doi.org/10.1016/S0377-0273(01)00227-X)
- Aguirre-Díaz, G. J., & López-Martínez, M. (2009). Geologic evolution of the Donguinyó-Huichapan caldera complex, central Mexican Volcanic Belt, México. *Journal of Volcanology and Geothermal Research*, 179(1–2), 133–148. <https://doi.org/10.1016/j.jvolgeores.2008.10.013>
- Aguirre-Díaz, G. J., & McDowell, F. W. (2007). Volcanic evolution of the Amealco caldera, central México. Special Paper 334: Cenozoic Tectonics and Volcanism of México, 179–193. <https://doi.org/10.1130/0-8137-2334-5.179>
- Aguirre-Díaz, G. J., Nieto-Obregón, J., & Zúñiga, F. R. (2005). Seismogenic basin and range and intra-arc normal faulting in the central Mexican Volcanic Belt, Querétaro, México. *Geological Journal*, 40(2), 215–243. <https://doi.org/10.1002/gj.1004>
- Alaniz-Álvarez, S. A., & Nieto-Samaniego, Á. F. (2005). El sistema de fallas Taxco-San Miguel de Allende y la Faja Volcánica Transmexicana, dos fronteras tectónicas del centro de México activas durante el Cenozoico. *Boletín de La Sociedad Geológica Mexicana*, 57(1), 65–82. <https://doi.org/10.18268/bsgm2005v57n1a4>
- Alaniz-Álvarez, S. A., Nieto-Samaniego, Á. F., Reyes-Zaragoza, M. A., Orozco-Esquivel, M. T., Ojeda-García, Á. C., & Vassallo, L. F. (2001). Estratigrafía y deformación extensional en la región San Miguel de Allende-Querétaro, México. *Revista Mexicana de Ciencias Geológicas*, 18(2), 129–148.
- Alarcón-Herrera, M. T., Bundschuh, J., Nath, B., Nicolli, H. B., Gutiérrez, M., Reyes-Gómez, V. M., Nuñez, D., Martín-Domínguez, I. R., & Sracek, O. (2013). Co-occurrence of arsenic and fluoride in groundwater of semi-arid regions in Latin

- America: Genesis, mobility and remediation. *Journal of Hazardous Materials*, 262, 960–969. <https://doi.org/10.1016/J.JHAZMAT.2012.08.005>
- Alazard, M., Leduc, C., Travi, Y., Boulet, G., & Ben Salem, A. (2015). Estimating evaporation in semi-arid areas facing data scarcity: Example of the El Haouareb dam (Merguellil catchment, Central Tunisia). *Journal of Hydrology: Regional Studies*, 3, 265–284. <https://doi.org/10.1016/j.ejrh.2014.11.007>
- Ali, S., Narayan, G., & Ranvir, S. (2008). Evaluating best evaporation estimate model for water surface evaporation in semi-arid region, India. *Hydrological Processes*, 22(August 2007), 1093–1106. <https://doi.org/10.1002/hyp.6664>
- Ambach, W., Dansgaard, W., Eisner, H., & Møller, J. (2012). The altitude effect on the isotopic composition of precipitation and glacier ice in the Alps. *Tellus*, 20(4), 595–600. <https://doi.org/10.3402/tellusa.v20i4.10040>
- Ángeles-Moreno, E., Nieto-Samaniego, A. F., Ruiz-González, F. J., Levresse, G., Alaniz-Álvarez, S. A., Olmos Moya, M. de J. P., Xu, S., & Miranda-Avilés, R. (2017). The transition between shortening and extensional regimes in central México recorded in the tourmaline veins of the Comanja Granite. *Journal of South American Earth Sciences*, 73, 65–77. <https://doi.org/10.1016/J.JSAMES.2016.12.004>
- Araguás-Araguás, L., Froehlich, K., & Rozanski, K. (2000). Deuterium and oxygen-18 isotope composition of precipitation and atmospheric moisture. *Hydrological Processes*, 14(2000), 1341–1355.
- Aranda-Gómez, J. J., & McDowell, F. W. (1998). Paleogene extension in the southern basin and range province of México: Syndepositional tilting of Eocene red beds and Oligocene volcanic rocks in the Guanajuato mining district. *International Geology Review*, 40(2), 116–134. <https://doi.org/10.1080/00206819809465201>
- Arango-Galván, C., Prol-Ledesma, R. M., Flores-Márquez, E. L., Canet, C., & Villanueva Estrada, R. E. (2011). Shallow submarine and subaerial, low-enthalpy hydrothermal manifestations in Punta Banda, Baja California, México: Geophysical and geochemical characterization. *Geothermics*, 40(2), 102–111. <https://doi.org/10.1016/j.geothermics.2011.03.002>
- Arango Guevara, A. F., Mitre Salazar, L. M., & Martínez Reyes, J. (2011). Actualización del conocimiento geológico en la Cuenca del Río Chichimequillas, Estado de Querétaro, México. *Trabajos De Geología*, 27(27). <https://reunido.uniovi.es/index.php/TDG/article/view/360>
- Arce, J. L., Rangel, E., Moreno, G. V., Girón, R. S., Govea, R. C., & Macías, J. L. (2021). Caracterización geoquímica, petrográfica y evolución magmática del Campo Volcánico de Los Azufres, Michoacán, durante el Pleistoceno. *Revista mexicana de ciencias geológicas*, 38(2), 122-140.

- Armienta, M. A., & Segovia, N. (2008). Arsenic and fluoride in the groundwater of México. *Environmental Geochemistry and Health*, 30(4), 345–353. <https://doi.org/10.1007/s10653-008-9167-8>
- Arreguín-Cortés, F. I., López-Pérez, M., & Cervantes-Jaimes, C. E. (2020). Water challenges in México. *Tecnología y Ciencias Del Agua*, 11(2), 341–371. <https://doi.org/10.24850/j-tyca-2020-02-10>
- Avellán, D. R., Cisneros-Máximo, G., Macías, J. L., Gómez-Vasconcelos, M. G., Layer, P. W., Sosa-Ceballos, G., & Robles-Camacho, J. (2020). Eruptive chronology of monogenetic volcanoes northwestern of Morelia – Insights into volcano-tectonic interactions in the central-eastern Michoacán-Guanajuato Volcanic Field, México. *Journal of South American Earth Sciences*, 100, 102554. <https://doi.org/10.1016/J.JSAMES.2020.102554>
- Ballentine, C. J., & Burnard, P. G. (2002). Production, Release and Transport of Noble Gases in the Continental Crust. *Reviews in Mineralogy and Geochemistry*, 47(1), 481–538. <https://doi.org/10.2138/RMG.2002.47.12>
- Ballentine, C., Marty, B., Sherwood Lollar, B., Cassidy, M. (2005). Neon isotopes constrain convection and volatile origin in the Earth's mantle. *Nature* 433, 33–38. <https://doi.org/10.1038/nature03182>
- Benetti, M., Reverdin, G., Pierre, C., Merlivat, L., Risi, C., Steen-larsen, H. C., & Vimeux, F. (2014). Journal of Geophysical Research: Atmospheres during evaporation, 584–593. <https://doi.org/10.1002/2013JD020535>. Received
- Barragán, R. M., Arellano, V. M., Portugal, E. y Sandoval, F., 2005. Isotopic ($\delta^{18}\text{O}$, δD) patterns in Los Azufres (México) geothermal fluids related to reservoir exploitation. *Geothermics*, 34, 527-547.
- Bekaert, D. v., Turner, S. J., Broadley, M. W., Barnes, J. D., Halldoacutessson, S. A., Labidi, J., Wade, J., Walowski, K. J., & Barry, P. H. (2021). Subduction-Driven Volatile Recycling: A Global Mass Balance. [Https://Doi.Org/10.1146/Annurev-Earth-071620-055024](https://doi.org/10.1146/annurev-earth-071620-055024), 49, 37–70. <https://doi.org/10.1146/ANNUREV-EARTH-071620-055024>
- Besser, H., Mokadem, N., Redhaounia, B., Hadji, R., Hamad, A., & Hamed, Y. (2018). Groundwater mixing and geochemical assessment of low-enthalpy resources in the geothermal field of southwestern Tunisia. *Euro-Mediterranean Journal for Environmental Integration*, 3(1), 1–15. <https://doi.org/10.1007/s41207-018-0055-z>
- Benson, B. B., & Krause, D. (1980). Isotopic fractionation of helium during solution: A probe for the liquid state. *Journal of Solution Chemistry* 1980 9:12, 9(12), 895–909. <https://doi.org/10.1007/BF00646402>
- Billarent-Cedillo, A., Levresse, G., Ferrari, L., Inguaggiato, C., Hernández-Pérez, E., Hernández-Espriú, A., Arias-paz, A., Corbo-Camargo, F., & Carrera-Hernández, J. J. (2021). Geothermics Deciphering origins and pathways of low-enthalpy

- geothermal waters in the unconventional geothermal system of Juchipila graben (Central México). 94. <https://doi.org/10.1016/j.geothermics.2021.102076>
- Blaney, H. F., & Criddle, W. D. (1950). Determining water requirements in irrigated areas from climatological and irrigation data. U.S.D.A., 43.
- Botero-Santa, P.A., Alaniz-Álvarez, S.A., Nieto-Samaniego, A.F., López-Martínez, M., Levresse, G., Xu, S., Ortega-Obregón, C., 2015, Origen y desarrollo de la cuenca El Bajío en el sector central de la Faja Volcánica Transmexicana: Revista Mexicana de Ciencias Geológicas, v. 32, núm. 1, p. 84-98.
- Bowen, I. S. (1926). The ratio of Heat Losses by Conduction and by Evaporation from any Water Surface. *Physical Review*, 27, 779–787. <https://doi.org/10.5194/hess-20-823-2016>
- Buttitta, D., Caracausi, A., Chiaraluce, L., Favara, R., Gasparo Morticelli, M., & Sulli, A. (2020). Continental degassing of helium in an active tectonic setting (northern Italy): the role of seismicity. *Scientific Reports* 2020 10:1, 10(1), 1–13. <https://doi.org/10.1038/s41598-019-55678-7>
- Byers, H. R., Moses, H., & Harney, P. J. (1949). Measurement of rain temperature. *Journal of Meteorology*, 6(1), 51–55.
- Byerlee J. (1993). Model for episodic flow of high-pressure water in fault zones before earthquakes. *Geology*, 21(4), 303–306.
- Calva-Hernández, D. (2011). Caracterización isotópica de la precipitación en el Estado de San Luis Potosí. Universidad Autónoma de San Luis Potosí Universidad Autónoma de San Luis Potosí.
- Capasso, G., & Inguaggiato, S. (1998). A simple method for the determination of dissolved gases in natural waters. An application to thermal waters from Vulcano Island. *Applied Geochemistry*, 13(5), 631–642. [https://doi.org/10.1016/S0883-2927\(97\)00109-1](https://doi.org/10.1016/S0883-2927(97)00109-1)
- Carreón-Freyre, D., Cerca, M., Luna-González, L., & Gámez-González, F. J. (2005). Influencia de la estratigrafía y estructura geológica en el flujo de agua subterránea del Valle de Querétaro. *Revista Mexicana de Ciencias Geológicas*, 22(1), 1–18.
- Carrera-Hernández, J. J., Carreón-Freyre, D., Cerca-Martínez, M., & Levresse, G. (2016). Groundwater flow in a transboundary fault-dominated aquifer and the importance of regional modeling: the case of the city of Querétaro, México. *Hydrogeology Journal*, 24(2), 373–393. <https://doi.org/10.1007/s10040-015-1363-x>
- Carrera-Hernandez, J. J. (2018). A tale of México's most exploited—and connected—watersheds: the Basin of México and the Lerma-Chapala Basin. *WIREs Water*, 5(1), 1–15. <https://doi.org/10.1002/wat2.1247>

- Carrillo-Rivera, J. J., Cardona, A., & Edmunds, W. M. (2002). Use of abstraction regime and knowledge of hydrogeological conditions to control high-fluoride concentration in abstracted groundwater: San Luis Potosí Basin, México. *Journal of Hydrology*, 261(1–4), 24–47. [https://doi.org/10.1016/S0022-1694\(01\)00566-2](https://doi.org/10.1016/S0022-1694(01)00566-2)
- Carucci, V., Petitta, M., & Aravena, R. (2012). Interaction between shallow and deep aquifers in the Tivoli Plain (Central Italy) enhanced by groundwater extraction: A multi-isotope approach and geochemical modeling. *Applied Geochemistry*, 27(1), 266–280. <https://doi.org/10.1016/j.apgeochem.2011.11.007>
- Chabal, Y. J. (1988). Surface infrared spectroscopy. *Surface Science Reports* (Vol. 8).
- Chowdhury, S., Dey, S., Ghosh, S., & Saud, T. (2016). Satellite-based estimates of aerosol washout and recovery over India during monsoon. *Aerosol and Air Quality Research*, 16(5), 1302–1314. <https://doi.org/10.4209/aaqr.2015.01.0018>
- Clark, I., & Fritz, P. (1997). Environmental isotopes in hydrogeology. In *Environmental Geology*.
- Cooper, H. H., & Jacob, C. E. (1946). A generalized graphical method for evaluating formation constants and summarizing well-field history. *Eos, Transactions American Geophysical Union*, 27(4), 526–534. <https://doi.org/10.1029/TR027i004p00526>
- Coplen, T. B. (1988). Normalization of oxygen and hydrogen isotope data. *Chemical Geology: Isotope Geoscience Section*, 72(4), 293–297. [https://doi.org/10.1016/0168-9622\(88\)90042-5](https://doi.org/10.1016/0168-9622(88)90042-5)
- Cortés-Silva, A., & Farvolden, R. N. (1989). Isotope Studies of Precipitation and Groundwater in The Sierra de las Cruces, México. *Journal of Hydrology*, 107, 147–153.
- Craig, H., & Gordon, L. (1965). Deuterium and oxygen 18 variations in the ocean and the marine atmosphere.
- Craig, H., Lupton, J. E., Welhan, J. A., & Poreda, R. (1978). Helium isotope ratios in Yellowstone and Lassen Park volcanic gases. *Geophysical Research Letters*, 5(11), 897–900. <https://doi.org/10.1029/GL005I011P00897>
- Cruz-Ayala, M. B., & Megdal, S. B. (2020). An overview of managed aquifer recharge in México and its legal framework. *Water (Switzerland)*, 12(2). <https://doi.org/10.3390/w12020474>
- Dansgaard, W. (1964). Stable isotopes in precipitation. *Tellus*, 16(4), 436–468. <https://doi.org/10.3402/tellusa.v16i4.8993>
- Dávalos-Álvarez, O. G., Nieto-Samaniego, Á. F., Alaniz-Álvarez, S. A., & Gómez-González, J. M. (2005). Las fases de deformación cenozoica en la región de

Huimilpan, Querétaro, y su relación con la sismicidad local. Revista Mexicana de Ciencias Geológicas, 22(2), 129–147.

de Leeuw, G. A. M., Hilton, D. R., Güleç, N., & Mutlu, H. (2010). Regional and temporal variations in CO₂/3He, 3He/4He and δ¹³C along the North Anatolian Fault Zone, Turkey. *Applied Geochemistry*, 25(4), 524–539. <https://doi.org/10.1016/j.apgeochem.2010.01.010>

Delalande, M., Bergonzini, L., & Massault, M. (2008). Mbaka lakes isotopic (¹⁸O and ²H) and water balances: Discussion on the used atmospheric moisture compositions. *Isotopes in Environmental and Health Studies*, 44(1), 71–82. <https://doi.org/10.1080/10256010801887414>

Del Pilar-Martínez, A., Nieto-Samaniego, A. F., Alaniz-Alvarez, S. A., & Angeles-Moreno, E. (2020). Geology of the southern Mesa Central of México: recording the beginning of a polymodal fault system. *Journal of Maps*, 16(2), 199–211. <https://doi.org/10.1080/17445647.2020.1719911>

Dogramaci, S., & Herczeg, A. L. (2002). Strontium and carbon isotope constraints on carbonate-solution interactions and inter-aquifer mixing in groundwaters of the semi-arid Murray Basin, Australia. *Journal of Hydrology*, 262(1–4), 50–67. [https://doi.org/10.1016/S0022-1694\(02\)00021-5](https://doi.org/10.1016/S0022-1694(02)00021-5)

Durand, V., Deffontaines, B., Leonardi, V., Guerin, R., Wyns, R., de Marsily, G., & Bonjour, J. L. (2006). A multidisciplinary approach to determine the structural geometry of hard-rock aquifers. Application to the Plancoet migmatitic aquifer (NE Brittany, W France). *Bulletin de La Societe Geologique de France*, 177(5), 227–236. <https://doi.org/10.2113/gssgbull.177.5.227>

Fellman, J. B., Dogramaci, S., Skrzypek, G., Dodson, W., & Grierson, P. F. (2011). Hydrologic control of dissolved organic matter biogeochemistry in pools of a subtropical dryland river. *Water Resources Research*, 47(6), 1–13. <https://doi.org/10.1029/2010WR010275>

Ferrari, L., Conticelli, S., Vaggelli, G., Petrone, C. M., & Manetti, P. (2000). Late Miocene volcanism and intra-arc tectonics during the early development of the Trans-Mexican Volcanic Belt. *Tectonophysics*, 318(1–4), 161–185. [https://doi.org/10.1016/S0040-1951\(99\)00310-8](https://doi.org/10.1016/S0040-1951(99)00310-8)

Ferrari, L., Garduño, V. H., Pasquare, G., & Tibaldi, A. (1991). Geology of Los Azufres Caldera, México, and its relationships with regional tectonics. *Journal of Volcanology and Geothermal Research*, 47(1–2), 129–148. [https://doi.org/10.1016/0377-0273\(91\)90105-9](https://doi.org/10.1016/0377-0273(91)90105-9)

Ferrari, L., Tagami, T., Eguchi, M., Orozco-Esquivel, M. T., Petrone, C. M., Jacobo-Albarrán, J., & López-Martínez, M. (2005). Geology, geochronology and tectonic setting of late Cenozoic volcanism along the southwestern Gulf of México: The Eastern Alkaline Province revisited. *Journal of Volcanology and*

Geothermal Research, 146(4), 284–306.
<https://doi.org/10.1016/J.JVOLGEORES.2005.02.004>

Ferrari, L., Orozco-Esquivel, T., Bryan, S. E., López-Martínez, M., & Silva-Fragoso, A. (2018). Cenozoic magmatism and extension in western México: Linking the Sierra Madre Occidental silicic large igneous province and the Comondú Group with the Gulf of California rift. *Earth-Science Reviews*, 183, 115–152. <https://doi.org/10.1016/j.earscirev.2017.04.006>

Fitz-Díaz, E., Lawton, T. F., Juárez-Arriaga, E., & Chávez-Cabello, G. (2018). The Cretaceous-Paleogene Mexican orogen: Structure, basin development, magmatism and tectonics. *Earth-Science Reviews*, 183, 56–84. <https://doi.org/10.1016/j.earscirev.2017.03.002>

Fritz, P., & Fontes, J. C. (1986). Handbook of Environmental Isotope Geochemistry. In The Terrestrial Environment, B (Vol. 2).

Fontes, J. -C, & Garnier, J. -M. (1979). Determination of the initial ^{14}C activity of the total dissolved carbon: A review of the existing models and a new approach. *Water Resources Research*, 15(2), 399–413. <https://doi.org/10.1029/WR015i002p00399>

Fontes, J. C., & Gonfiantini, R. (1967). Comportement Isotopique Au Cours De L ' Evaporation. *Earth and Planetary Science Letters*, 3, 258–266.

Gale, A., Dalton, C. A., Langmuir, C. H., Su, Y., & Schilling, J. G. (2013). The mean composition of ocean ridge basalts. *Geochemistry, Geophysics, Geosystems*, 14(3), 489–518. <https://doi.org/10.1029/2012GC004334>

Gat, J. R. (1981). Lakes. Stable Isotope Hydrology-Deuterium and Oxygen-18 in the Water Cycle In: J.R. Gat, R. Gonfiantini (Eds.). IAEA Technical Report Series No. 210, Vienna, pp. 203-221.

Gat, J. R., & Levy, Y. (1978). Isotope hydrology of inland sabkhas in the Bardawil area, Sinai. *Limnol. Oceanogr.*, 23(5), 841–850.

Gat, J. R., Bowser, C. J., & Kendall, C. (1994). The contribution of evaporation from the Great Lakes to the continental atmosphere: estimate based on stable isotope data. *Geophysical Research Letters*, 21(7), 557–560. <https://doi.org/10.1029/94GL00069>

Gat, J. R., Ben-Mair, R., Yam, R., Yakir, D., & Wernli, H. (2005). The isotope composition of atmospheric waters in Israel's coastal plain, Isotopic composition of precipitation in the Mediterranean Basin in relation to air circulation patterns and climate. International Atomic Energy Agency, Isotope Hydrology Section. Retrieved from http://www.iaea.org/inis/collection/NCLCollectionStore/_Public/36/110/36110957.pdf#page=132

- Gautheron, C., & Moreira, M. (2002). Helium signature of the subcontinental lithospheric mantle. *Earth and Planetary Science Letters*, 199(1-2), 39–47. [https://doi.org/10.1016/S0012-821X\(02\)00563-0](https://doi.org/10.1016/S0012-821X(02)00563-0)
- Gibson, J. J. (2002). Short-term evaporation and water budget comparisons in shallow Arctic lakes using non-steady isotope mass balance. *Journal of Hydrology*, 264(1-4), 242–261. [https://doi.org/10.1016/S0022-1694\(02\)00091-4](https://doi.org/10.1016/S0022-1694(02)00091-4)
- Gibson, J. J., & Reid, R. (2010). Stable isotope fingerprint of open-water evaporation losses and effective drainage area fluctuations in a subarctic shield watershed. *Journal of Hydrology*, 381(1-2), 142–150. <https://doi.org/10.1016/j.jhydrol.2009.11.036>
- Gibson, J. J., Edwards, T. W. D., & Prowse, T. D. (1999). Pan-derived isotopic composition of atmospheric water vapour and its variability in northern Canada. *Journal of Hydrology*, 217(1-2), 55–74. [https://doi.org/10.1016/S0022-1694\(99\)00015-3](https://doi.org/10.1016/S0022-1694(99)00015-3)
- Gibson, J. J., Birks, S. J., & Edwards, T. W. D. (2008). Global prediction of δ_A and $\delta^2\text{H}$ - $\delta^{18}\text{O}$ evaporation slopes for lakes and soil water accounting for seasonality. *Global Biogeochemical Cycles*, 22(2), n/a-n/a. <https://doi.org/10.1029/2007GB002997>
- Gibson, J. J., Birks, S. J., & Yi, Y. (2016). Stable isotope mass balance of lakes: A contemporary perspective. *Quaternary Science Reviews*, 131, 316–328. <https://doi.org/10.1016/j.quascirev.2015.04.013>
- Giggenbach, W. F., Sano, Y., & Wakita, H. (1993). Isotopic composition of helium, and CO₂ and CH₄ contents in gases produced along the New Zealand part of a convergent plate boundary. *Geochimica et Cosmochimica Acta*, 57(14), 3427–3455. [https://doi.org/10.1016/0016-7037\(93\)90549-C](https://doi.org/10.1016/0016-7037(93)90549-C)
- Gleason, J. A., & Flores, C. C. (2021). Challenges of water sensitive cities in México: The case of the metropolitan area of Guadalajara. *Water (Switzerland)*, 13(5), 1–19. <https://doi.org/10.3390/w13050601>
- Gómez-Tuena, A., Orozco-Esquivel, Ma. T., & Ferrari, L. (2005). Petrogénesis ígnea de la Faja Volcánica Transmexicana. *Boletín de La Sociedad Geológica Mexicana*, 57(3), 227–283. <https://doi.org/10.18268/bsgm2005v57n3a2>
- Gómez-Tuena A., Mori L., Straub S.M. (2018) Geochemical and petrological insights into the tectonic origin of the Transmexican Volcanic Belt, *Earth-Science Reviews*, Volume 183, 153-181, ISSN 0012-8252, <https://doi.org/10.1016/j.earscirev.2016.12.006>.
- Gómez-Vasconcelos, M. G., Luis Macías, J., Avellán, D. R., Sosa-Ceballos, G., Garduño-Monroy, V. H., Cisneros-Máximo, G., Layer, P. W., Benowitz, J., López-Loera, H., López, F. M., & Perton, M. (2020). The control of preexisting faults on the distribution, morphology, and volume of monogenetic volcanism in the

- Michoacán-Guanajuato Volcanic Field. *GSA Bulletin*, 132(11–12), 2455–2474. <https://doi.org/10.1130/B35397.1>
- Gonfiantini, R. (1986). Environmental Isotopes in Lake Studies. In J. C. Fritz, P. and Fontes (Ed.), *Handbook of Environmental Isotope Geochemistry. The Terrestrial Environment.* (pp. 113–168). Amsterdam: Elsevier.
- Gonfiantini, R., Wassenaar, L., Araguás-Araguás, L., & Aggarwal, P. K. (2018). A unified Craig-Gordon isotope model of stable hydrogen and oxygen isotope fractionation during fresh or saltwater evaporation. *Geochimica et Cosmochimica Acta*, 235, 224–236. <https://doi.org/10.1016/j.gca.2018.05.020>
- González-Guzmán, R., Inguaggiato, C., Peiffer, L., Weber, B., & Kretzschmar, T. (2019). Fault-controlled geothermal fluids of the northern Trans-Mexican Volcanic Belt: A geochemical and isotopic study of the Los Geysers field (Valley of Querétaro, México). *Journal of Volcanology and Geothermal Research*, 388(November). <https://doi.org/10.1016/j.jvolgeores.2019.106681>
- González-Partida, E., Carrillo-Chávez, A., Levresse, G., Tello-Hinojosa, E., Venegas-Salgado, S., Ramírez-Silva, G., Pal-Verma, M., Tritlla, J., & Camprubi, A. (2005). Hydro-geochemical and isotopic fluid evolution of the Los Azufres geothermal field, Central México. *Applied Geochemistry*, 20(1), 23–39. <https://doi.org/10.1016/J.APGEOCHEM.2004.07.006>
- Graham, D. W. (2002). Noble gas isotope geochemistry of mid-ocean ridge and ocean island basalts: Characterization of mantle source reservoirs. *Reviews in Mineralogy and Geochemistry*, 47. <https://doi.org/10.2138/rmg.2002.47.8>
- Guerrero-Martínez, L., Hernández-Marín, M., & Burbey, T. J. (2018). Estimation of natural groundwater recharge in the Aguascalientes semiarid valley, México. *Revista Mexicana de Ciencias Geológicas*, 35(3), 268–276. <https://doi.org/10.22201/cgeo.20072902e.2018.2.1022>
- Hamon, W. R. (1960). Estimating potential evapotranspiration. Massachusetts Institute of Technology.
- Han, L. F., & Plummer, L. N. (2013). Revision of Fontes & Garnier's model for the initial ^{14}C content of dissolved inorganic carbon used in groundwater dating. *Chemical Geology*, 351, 105–114. <https://doi.org/10.1016/j.chemgeo.2013.05.011>
- Han, Liang Feng, Plummer, L. N., & Aggarwal, P. (2012). A graphical method to evaluate predominant geochemical processes occurring in groundwater systems for radiocarbon dating. *Chemical Geology*, 318–319, 88–112. <https://doi.org/10.1016/j.chemgeo.2012.05.004>
- Hasenaka, T. (1994). Size, distribution, and magma output rate for shield volcanoes of the Michoacán-Guanajuato volcanic field, Central México. *Journal of Volcanology and Geothermal Research*, 63(1-2), 13-31.

- Hasenaka, T., & Carmichael, I. S. (1985). The cinder cones of Michoacán—Guanajuato, central México: Their age, volume and distribution, and magma discharge rate. *Journal of Volcanology and Geothermal Research*, 25(1-2), 105-124.
- Hegg, D. A., Clarke, A. D., Doherty, S. J., & Ström, J. (2011). Measurements of black carbon aerosol washout ratio on Svalbard. *Tellus, Series B: Chemical and Physical Meteorology*, 63(5), 891–900. <https://doi.org/10.1111/j.1600-0889.2011.00577.x>
- Hernández-Antonio, A., Mahlknecht, J., Tamez-Meléndez, C., Ramos-Leal, J., Ramírez-Orozco, A., Parra, R., Ornelas-Soto, N., & Eastoe, C. J. (2015). Groundwater flow processes and mixing in active volcanic systems: The case of Guadalajara (México). *Hydrology and Earth System Sciences*, 19(9), 3937–3950. <https://doi.org/10.5194/hess-19-3937-2015>
- Hernández-Pérez, E., Levresse, G., Carrera-Hernández, J., & García-Martínez, R. (2020). Short term evaporation estimation in a natural semiarid environment: New perspective of the Craig – Gordon isotopic model. *Journal of Hydrology*, 587(April), 124926. <https://doi.org/10.1016/j.jhydrol.2020.124926>
- Herrera, C., Custodio, E., Chong, G., Lambán, L. J., Riquelme, R., Wilke, H., Jódar, J., Urrutia, J., Urqueta, H., Sarmiento, A., Gamboa, C., & Lictevout, E. (2016). Groundwater flow in a closed basin with a saline shallow lake in a volcanic area: Laguna Tuyajto, northern Chilean Altiplano of the Andes. *Science of the Total Environment*, 541, 303–318. <https://doi.org/10.1016/j.scitotenv.2015.09.060>
- Hiett, C. D., Newell, D. L., & Jessup, M. J. (2021). ³He evidence for fluid transfer and continental hydration above a flat slab. *Earth and Planetary Science Letters*, 556. <https://doi.org/10.1016/j.epsl.2020.116722>
- Hilton, D. R. (1996). The helium and carbon isotope systematics of a continental geothermal system: results from monitoring studies at Long Valley caldera (California, U.S.A.). *Chemical Geology*, 127(4), 269–295. [https://doi.org/10.1016/0009-2541\(95\)00134-4](https://doi.org/10.1016/0009-2541(95)00134-4)
- Hilton, D. R. (2007). Geochemistry: The leaking mantle. *Science*, 318(5855), 1389–1390. <https://doi.org/10.1126/SCIENCE.1151983>
- Hilton, D. R., & Porcelli, D. (2003). Noble Gases as Mantle Tracers. *Treatise on Geochemistry*, 2–9, 277–318. <https://doi.org/10.1016/B0-08-043751-6/02007-7>
- Hilton, David R., Fischer, T. P., & Marry, B. (2002). Noble gases and volatile recycling at subduction zones. *Reviews in Mineralogy and Geochemistry*, 47. <https://doi.org/10.2138/rmg.2002.47.9>
- Horita, J., & Wesolowski, D. J. (1994). Liquid-vapor fractionation of oxygen and hydrogen isotopes of water from freezing to the critical temperature.

- Geochimica et Cosmochimica Acta, 58(16), 3425–3437. Retrieved from papers2://publication/uuid/F9BCD32F-8569-4ACF-81AF-08518BF40A32
- Hooker, P. J., Bertrami, R., Lombardi, S., O’Nions, R. K., & Oxburgh, E. R. (1985). Helium-3 anomalies and crust-mantle interaction in Italy. *Geochimica et Cosmochimica Acta*, 49(12), 2505–2513. [https://doi.org/10.1016/0016-7037\(85\)90118-8](https://doi.org/10.1016/0016-7037(85)90118-8)
- Husker, A., & Davis, P. M. (2009). Tomography and thermal state of the Cocos plate subduction beneath México City. *Journal of Geophysical Research: Solid Earth*, 114(B4), 4306. <https://doi.org/10.1029/2008JB006039>
- Huang, J., Wang, T., Wang, W., Li, Z., & Yan, H. (2014). Journal of geophysical research. *Journal of Geophysical Research: Atmospheres*, 119(11), 11,398–11,416. <https://doi.org/10.1038/175238c0>
- Inguaggiato, S., & Rizzo, A. (2004). Dissolved helium isotope ratios in ground-waters: a new technique based on gas–water re-equilibration and its application to Stromboli volcanic system. *Applied Geochemistry*, 19(5), 665–673. <https://doi.org/10.1016/J.APGEOCHEM.2003.10.009>
- Jácome-Paz, M. P. (2019). Two new geothermal prospects in the Mexican Volcanic Belt: La Escalera and Agua Caliente – Tzitzio geothermal springs, Michoacán, México. *Geothermics*, 80(February), 44–55. <https://doi.org/10.1016/j.geothermics.2019.02.004>
- Khalil, M. M., Tokunaga, T., & Yousef, A. F. (2015). Insights from stable isotopes and hydrochemistry to the Quaternary groundwater system, south of the Ismailia canal, Egypt. *Journal of Hydrology*, 527, 555–564. <https://doi.org/10.1016/j.jhydrol.2015.05.024>
- Kennedy, B. M., Kharaka, Y. K., Evans, W. C., Ellwood, A., DePaolo, D. J., Thordsen, J., Ambats, G., & Mariner, R. H. (1997). Mantle fluids in the San Andreas fault system, California. *Science*, 278(5341), 1278–1281. <https://doi.org/10.1126/science.278.5341.1278>
- Kennedy, B. M., & van Soest, M. C. (2007). Flow of mantle fluids through the ductile lower crust: Helium isotope trends. *Science*, 318(5855), 1433–1436. https://doi.org/10.1126/SCIENCE.1147537/SUPPL_FILE/KENNEDY.SOM.PDF
- Kennedy, B. mac, & van Soest, M. C. (2006a). A helium isotope perspective on the Dixie Valley, Nevada, hydrothermal system. *Geothermics*, 35(1), 26–43. <https://doi.org/10.1016/j.geothermics.2005.09.004>
- Kim, Y., Clayton, R. W., & Jackson, J. M. (2010). Geometry and seismic properties of the subducting Cocos plate in central México. *Journal of Geophysical Research: Solid Earth*, 115(B6). <https://doi.org/10.1029/2009JB006942>

- Klemperer, S. L., Kennedy, B. M., Sastry, S. R., Makovsky, Y., Harinarayana, T., & Leech, M. L. (2013). Mantle fluids in the Karakoram fault: Helium isotope evidence. *Earth and Planetary Science Letters*, 366, 59–70. <https://doi.org/10.1016/j.epsl.2013.01.013>
- Kumar, B., & Nachiappan, R. P. (1999). On the sensitivity of Craig and Gordon model for the estimation of the isotopic composition of lake evaporates. *Water Resources Research*, 35(5), 1689–1691. <https://doi.org/10.1029/1999WR900011>
- Kulongoski, J. T., Hilton, D. R., Barry, P. H., Esser, B. K., Hillegonds, D., & Belitz, K. (2013). Volatile fluxes through the Big Bend section of the San Andreas Fault, California: Helium and carbon-dioxide systematics. *Chemical Geology*, 339, 92–102. <https://doi.org/10.1016/j.chemgeo.2012.09.007>
- Laaksoharju, M., Skårman, C., & Skårman, E. (1999). Multivariate mixing and mass balance (M3) calculations, a new tool for decoding hydrogeochemical information. *Applied Geochemistry*, 14(7), 861–871. [https://doi.org/10.1016/S0883-2927\(99\)00024-4](https://doi.org/10.1016/S0883-2927(99)00024-4)
- Lindau, R. (1995). A New Beaufort Equivalent Scale. *Proceedings of the International COADS Wind Workshop*, 232–252.
- Liu, X., Yu, J., Wang, P., Zhang, Y., & Du, C. (2016). Lake evaporation in a hyper-arid environment, northwest of China-measurement and estimation. *Water*, 8(11), 1–21. <https://doi.org/10.3390/w8110527>
- López-Alvis, J., Carrera-Hernández, J. J., Levresse, G., & Nieto-Samaniego, Á. F. (2019). Assessment of groundwater depletion caused by excessive extraction through groundwater flow modeling: the Celaya aquifer in central México. *Environmental Earth Sciences*, 78(15), 1–22. <https://doi.org/10.1007/S12665-019-8497-4/FIGURES/16>
- López Martínez M., Aguirre Díaz, G., & Valdez Moreno, G. (1998). El volcán La Joya, estados de Querétaro y Guanajuato: un estrato volcán miocénico del Cinturón Volcánico Mexicano. *Revista mexicana de ciencias geológicas*, 15(2), 8.
- Luhr, J. F., & Aranda-Gómez, J. J. (1997). Mexican Peridotite Xenoliths and Tectonic Terranes: Correlations among Vent Location, Texture, Temperature, Pressure, and Oxygen Fugacity. *Journal of Petrology*, 38(8), 1075–1112. <https://doi.org/10.1093/PETROJ/38.8.1075>
- Luhr, J. F., Kimberly, P., Siebert, L., Jorge Aranda-Gómez, J., Housh, T. B., & Mattietti, G. K. (2006). México's Quaternary volcanic rocks: Insights from the MEXPET petrological and geochemical database. *Special Paper of the Geological Society of America*, 402, 1–44. [https://doi.org/10.1130/2006.2402\(01\)](https://doi.org/10.1130/2006.2402(01))

- Luna-Niño, R., & Cavazos, T. (2018). Formation of a coastal barrier jet in the Gulf of México due to the interaction of cold fronts with the Sierra Madre Oriental Mountain range. *Quarterly Journal of the Royal Meteorological Society*, 144(710), 115–128. <https://doi.org/10.1002/qj.3188>
- Lyon Giggenbach, W.F, Singleton, R.J, Glasby, G.P, G. L. (1977). Isotopic and chemical composition of submarine geothermal gases from the Bay of Plenty New Zealand. In *Geochemistry*.
- Mahlknecht, J., Horst, A., Hernández-Limón, G., & Aravena, R. (2008). Groundwater geochemistry of the Chihuahua City region in the Rio Conchos Basin (northern México) and implications for water resources management. *Hydrological Processes*, 22(24), 4736–4751. <https://doi.org/10.1002/hyp>
- Majidi, M., Alizadeh, A., Farid, A., & Vazifedoust, M. (2015). Estimating evaporation from lakes and reservoirs under limited data condition in a semi-arid region. *Water Resources Management*, 29(10), 3711–3733. <https://doi.org/10.1007/s11269-015-1025-8>
- Makkink, G. F. (1957). Ekzameno De La Formulo De Penman. *Neth. J. Agri. Sci.*, 5, 290–305. Retrieved from https://hydrologie.org/BIB/Curiosa/Makkink_Neth.J.AgricSci1957.pdf
- Mamyrin, B. A. (Boris A., & Tolstikhin, I. N. (Igor' N. (1984). Helium isotopes in nature. 273.
- Marín-Camacho, P., Velasco-Tapia, F., Bernard-Romero, R., Weber, B., & González-Guzmán, R. (2022). New geochemical evidence constraining the water-rock-gas interaction on geothermal fluids of the Querétaro Graben, northern Trans-Mexican Volcanic Belt. *Journal of South American Earth Sciences*, 114(October 2021). <https://doi.org/10.1016/j.jsames.2021.103702>
- Martini, M., Solé, J., Garduño-Martínez, D. E., Puig, T. P., & Omaña, L. (2016). Evidence for two Cretaceous superposed orogenic belts in central México based on palaeontologic and K-Ar geochronologic data from the Sierra de los Cuarzos. *Geosphere*, 12(4), 1257–1270. <https://doi.org/10.1130/GES01275.1>
- Méjean, P., Pinti, D. L., Kagoshima, T., Roulleau, E., Demarets, L., Poirier, A., Takahata, N., Sano, Y., & Larocque, M. (2020). Mantle helium in Southern Quebec groundwater: A possible fossil record of the New England hotspot. *Earth and Planetary Science Letters*, 545, 116352. <https://doi.org/10.1016/j.epsl.2020.116352>
- Menzies, C. D., Teagle, D. A. H., Niedermann, S., Cox, S. C., Craw, D., Zimmer, M., Cooper, M. J., & Erzinger, J. (2016). The fluid budget of a continental plate boundary fault: Quantification from the Alpine Fault, New Zealand. *Earth and Planetary Science Letters*, 445, 125–135. <https://doi.org/10.1016/j.epsl.2016.03.046>

- Morales, I., Villanueva-Estrada, R. E., Rodríguez, R., & Armienta, M. A. (2015). Geological, hydrogeological, and geothermal factors associated to the origin of arsenic, fluoride, and groundwater temperature in a volcanic environment "El Bajío Guanajuatense", México. *Environmental Earth Sciences*, 74(6), 5403–5415. <https://doi.org/10.1007/s12665-015-4554-9>
- Morales-Arredondo, J. I., Armienta Hernández, M. A., Ortega-Gutiérrez, J. E., Flores-Ocampo, I. Z., & Flores-Vargas, R. (2020). Evaluation of the carbon dioxide behavior in a thermal aquifer located at Central México and its relation to silicate weathering. *International Journal of Environmental Science and Technology*, 17(7), 3411–3430. <https://doi.org/10.1007/s13762-020-02683-3>
- Mori, L., Gómez-Tuena, A., Cai, Y., & Goldstein, S. L. (2007). Effects of prolonged flat subduction on the Miocene magmatic record of the central Trans-Mexican Volcanic Belt. *Chemical Geology*, 244(3–4), 452–473. <https://doi.org/10.1016/J.CHEMGEO.2007.07.002>
- Murgulet, D., Cook, M., & Murgulet, V. (2016). Groundwater mixing between different aquifer types in a complex structural setting discerned by elemental and stable isotope geochemistry. *Hydrological Processes*, 30(3), 410–423. <https://doi.org/10.1002/hyp.10589>
- Newell, D. L., Jessup, M. J., Hilton, D. R., Shaw, C. A., & Hughes, C. A. (2015). Mantle-derived helium in hot springs of the Cordillera Blanca, Peru: Implications for mantle-to-crust fluid transfer in a flat-slab subduction setting. *Chemical Geology*, 417, 200–209. <https://doi.org/10.1016/J.CHEMGEO.2015.10.003>
- Nicolli, H. B., Bundschuh, J., Blanco, M. del C., Tujchneider, O. C., Panarello, H. O., Dapeña, C., & Rusansky, J. E. (2012). Arsenic and associated trace-elements in groundwater from the Chaco-Pampean plain, Argentina: Results from 100 years of research. *Science of The Total Environment*, 429, 36–56. <https://doi.org/10.1016/J.SCITOTENV.2012.04.048>
- Nieto-Samaniego, Á. F., Ferrari, L., Alaniz-Álvarez, S. A., Labarthe-Hernández, G., & Rosas-Elguera, J. (1999). Variation of Cenozoic extension and volcanism across the southern Sierra Madre Occidental volcanic province, México. *Bulletin of the Geological Society of America*, 111(2–3), 347–363. [https://doi.org/10.1130/0016-7606\(1999\)111<347>2.0.co;2](https://doi.org/10.1130/0016-7606(1999)111<347>2.0.co;2)
- Nieva, D., Verma, M., Santoyo, E., Barragán, R.M., Portugal, E., Ortíz, J. and Quijano, L. (1987) Chemical and Isotopic Evidence of Steam Upflow and Partial Condensation in Los Azufres Reservoir. Proceedings of 12th Workshop on Geothermal Reservoir Engineering Stanford University, Stanford, CA, 20-22 January 1987, 253-259.

- Ochoa-González, G. H., Carreón-Freyre, D., Cerca, M., & López-Martínez, M. (2015). Assessment of groundwater flow in volcanic faulted areas. A study case in Querétaro, México. *Geofísica Internacional*, 54(3), 199–220. <https://doi.org/10.1016/J.GI.2015.04.016>
- O'Nions, R. K., & Oxburgh, E. R. (1988). Helium, volatile fluxes and the development of continental crust. *Earth and Planetary Science Letters*, 90(3), 331–347. [https://doi.org/10.1016/0012-821X\(88\)90134-3](https://doi.org/10.1016/0012-821X(88)90134-3)
- Power, J. F., & Schepers, J. S. (1989). Nitrate contamination of groundwater in North America. *Agriculture, Ecosystems and Environment*, 26(3–4), 165–187. [https://doi.org/10.1016/0167-8809\(89\)90012-1](https://doi.org/10.1016/0167-8809(89)90012-1)
- Palacios-García, N. B., & Martini, M. (2014). From back-arc rifting to arc accretion: The Late Jurassic-Early Cretaceous evolution of the Guerrero terrane recorded by a major provenance change in sandstones from the Sierra de los Cuarzos area, central México. *International Geology Review*, 56(11), 1377–1394. https://doi.org/10.1080/00206814.2014.938367/SUPPL_FILE/TIGR_A_938367_SM8937.DOC
- Pérez-Campos, X., Kim, Y., Husker, A., Davis, P. M., Clayton, R. W., Iglesias, A., Pacheco, J. F., Singh, S. K., Manea, V. C., & Gurnis, M. (2008). Horizontal subduction and truncation of the Cocos Plate beneath central México. *Geophysical Research Letters*, 35(18). <https://doi.org/10.1029/2008GL035127>
- Pérez-Martínez, I., Villanueva-Estrada, R. E., Cardona-Benavides, A., Rodríguez-Díaz, A. A., Rodríguez-Salazar, M. T., & Guadalupe, J. (2020). Hydrogeochemical reconnaissance of the Atotonilco el Alto-Santa Rita geothermal system in the northeastern Chapala graben in México. *Geothermics*, 83, 101733. <https://doi.org/10.1016/j.geothermics.2019.101733>
- Pérez-Venzor, J. A., Aranda-Gómez, J. J., McDowell, F., & Solorio-Munguía, J. G. (1996). Geología del volcán Palo Huérano, Guanajuato, México. In *Revista Mexicana de Ciencias Geológicas* (Vol. 13, Issue 2, pp. 174–183).
- Penman, H. L. (1948). Natural evaporation from open water, bare soil and grass. *Proceedings of the Royal Society A.*, 193(1032).
- Penman, H. L. (1956). Estimating evaporation. *Eos, Transactions American Geophysical Union*, 37(1), 43–50. <https://doi.org/10.1029/TR037i001p00043>
- Pérez-Quezadas, J., Cortés-Silva, A., Inguaggiato, S., Salas-Ortega, M., Cervantes-Pérez, J., & Heilweil, V. M. (2015). Meteoric isotopic gradient on the windward side of the Sierra Madre Oriental area, Veracruz - México. *Geofísica Internacional*, 54(3), 267–276. <https://doi.org/10.1016/j.gi.2015.04.021>

- Pinti, D. L., Castro, M. C., Shouakar-Stash, O., Tremblay, A., Garduño, V. H., Hall, C. M., Hélie, J. F., & Ghaleb, B. (2013). Evolution of the geothermal fluids at Los Azufres, México, as traced by noble gas isotopes, $\delta^{18}\text{O}$, δD , $\delta^{13}\text{C}$ and $87\text{Sr}/86\text{Sr}$. *Journal of Volcanology and Geothermal Research*, 249, 1–11. <https://doi.org/10.1016/J.JVOLGEORES.2012.09.006>
- Plank, T., Kelley, K. A., Zimmer, M. M., Hauri, E. H., & Wallace, P. J. (2013). Why do mafic arc magmas contain ~4 wt% water on average? *Earth and Planetary Science Letters*, 364, 168–179. <https://doi.org/10.1016/J.EPSL.2012.11.044>
- Poulin, C., Hamelin, B., Vallet-Coulomb, C., Amngar, G., Loukman, B., Cretaux, J. F., et al. (2019). Unraveling the hydrological budget of isolated and seasonally contrasted subtropical lakes. *Hydrology and Earth System Sciences*, 23(3), 1705–1724. <https://doi.org/10.5194/hess-23-1705-2019>
- Priestley C. H. B. and Taylor, R. J. (1972). On the assessment of surface heat flux and evaporation using large-scale parameters. *Weather Review*, 100(2), 81–92.
- Prol-Ledesma, R. M., Carrillo-de la Cruz, J. L., Torres-Vera, M. A., Membrillo-Abad, A. S., & Espinoza-Ojeda, O. M. (2018). Heat flow map and geothermal resources in México. *Terra Digitalis*, 2(2), 1–15. <https://doi.org/10.22201/igg.25940694.2018.2.51>
- Ray, M. C., Hilton, D. R., Muñoz, J., Fischer, T. P., & Shaw, A. M. (2009). The effects of volatile recycling, degassing and crustal contamination on the helium and carbon geochemistry of hydrothermal fluids from the Southern Volcanic Zone of Chile. *Chemical Geology*, 266(1–2), 38–49. <https://doi.org/10.1016/J.CHEM GEO.2008.12.026>
- Rizzo, A. L., Barberi, F., Carapezza, M. L., di Piazza, A., Francalanci, L., Sortino, F., & D'Alessandro, W. (2015). New mafic magma refilling a quiescent volcano: Evidence from He-Ne-Ar isotopes during the 2011–2012 unrest at Santorini, Greece. *Geochemistry, Geophysics, Geosystems*, 16(3), 798–814. <https://doi.org/10.1002/2014GC005653>
- Rodríguez, R., Morales-Arredondo, I., & Rodríguez, I. (2016). Geological differentiation of groundwater threshold concentrations of arsenic, vanadium and fluorine in El Bajío Guanajuatense, México. *Geofísica Internacional*, 55(1), 5–15. <https://doi.org/10.22201/igeof.00167169p.2016.55.1.1708>
- Rudnick, R. L., & Gao, S. (2003). Composition of the Continental Crust. *Treatise on Geochemistry*, 3–9, 1–64. <https://doi.org/10.1016/B0-08-043751-6/03016-4>
- Sano, Y., & Wakita, H. (1985). Geographical distribution of $3\text{He}/4\text{He}$ ratios in Japan: Implications for arc tectonics and incipient magmatism. *Journal of Geophysical Research: Solid Earth*, 90(B10), 8729–8741. <https://doi.org/10.1029/JB090IB10P08729>

- Sánchez, R., Rodríguez, L., & Tortajada, C. (2018). Transboundary aquifers between Chihuahua, Coahuila, Nuevo Leon and Tamaulipas, México, and Texas, USA: Identification and categorization. *Journal of Hydrology: Regional Studies*, 20(January), 74–102. <https://doi.org/10.1016/j.ejrh.2018.04.004>
- Shaw, D. M., & Sturchio, N. C. (1992). Boron-lithium relationships in rhyolites and associated thermal waters of young silicic calderas, with comments on incompatible element behavior. *Geochimica et Cosmochimica Acta*, 56(10), 3723–3731. [https://doi.org/10.1016/0016-7037\(92\)90165-F](https://doi.org/10.1016/0016-7037(92)90165-F)
- Siegenthaler, U., & Oeschger, H. (1980). Correlation of ^{18}O in precipitation with temperature and altitude. *Nature*, 285(5763), 314–317. <https://doi.org/10.1038/285314a0>
- Skrzypek, G., Mydłowski, A., Dogramaci, S., Hedley, P., Gibson, J. J., & Grierson, P. F. (2015). Estimation of evaporative loss based on the stable isotope composition of water using Hydrocalculator. *Journal of Hydrology*, 523, 781–789. <https://doi.org/10.1016/j.jhydrol.2015.02.010>
- Smith, S. P., & Kennedy, B. M. (1983). The solubility of noble gases in water and in NaCl brine. *Geochimica et Cosmochimica Acta*, 47(3), 503–515. [https://doi.org/10.1016/0016-7037\(83\)90273-9](https://doi.org/10.1016/0016-7037(83)90273-9)
- Sow, M., & Lemaitre, P. (2016). Influence of electric charges on the washout efficiency of atmospheric aerosols by raindrops. *Annals of Nuclear Energy*, 93, 107–113. <https://doi.org/10.1016/j.anucene.2015.12.036>
- Straub, S. M., Gomez-Tuena, A., Stuart, F. M., Zellmer, G. F., Espinasa-Perena, R., Cai, Y., & Iizuka, Y. (2011). Formation of hybrid arc andesites beneath thick continental crust. *Earth and Planetary Science Letters*, 303(3–4), 337–347. <https://doi.org/10.1016/J.EPSL.2011.01.013>
- Tolstikhin, I. N., & Marty, B. (1998). The evolution of terrestrial volatiles: a view from helium, neon, argon and nitrogen isotope modelling. *Chemical Geology*, 147(1–2), 27–52. [https://doi.org/10.1016/S0009-2541\(97\)00170-8](https://doi.org/10.1016/S0009-2541(97)00170-8)
- Torgersen, T. (1993). Defining the role of magmatism in extensional tectonics: Helium-3 fluxes in extensional basins. *Journal of Geophysical Research: Solid Earth*, 98(B9), 16257–16269. <https://doi.org/10.1029/93JB00891>
- Torgersen T., Drenkard S., Stute M., Schlosser P., & Shapiro A. (1995). Mantle helium in ground waters of eastern North America: Time and space constraints on sources. *Geology*, 23(8), 675–678. https://pubs.geoscienceworld.org/gsa/geology/article/23/8/675/188103/Mantle-helium-in-ground-waters-of-eastern-North?casa_token=kSEddFjWs5AAAAAA:TA9W9Wz71LwiTsE0htIBpyHhVBKCfuqMdSpzdGkQqZVAKAvPxa2fltJPcei33y_uts_yzg

- Torgersen, T., & Jenkins, W. J. (1982). Helium isotopes in geothermal systems: Iceland, The Geysers, Raft River and Steamboat Springs. *Geochimica et Cosmochimica Acta*, 46(5), 739–748. [https://doi.org/10.1016/0016-7037\(82\)90025-4](https://doi.org/10.1016/0016-7037(82)90025-4)
- Trolldborg, L., Refsgaard, J. C., Jensen, K. H., & Engesgaard, P. (2007). The importance of alternative conceptual models for simulation of concentrations in a multi-aquifer system. *Hydrogeology Journal*, 15(5), 843–860. <https://doi.org/10.1007/s10040-007-0192-y>
- Urrutia-Fucugauchi, J., & Flores-Ruiz, J. H. (1996). Bouguer Gravity Anomalies and Regional Crustal Structure in Central México. <Http://Dx.Doi.Org/10.1080/00206819709465330>, 38(2), 176–194. <https://doi.org/10.1080/00206819709465330>
- Valenzuela-Vásquez, L., Ramírez-Hernández, J., Reyes-López, J., Sol-Uribe, A., & Lázaro-Mancilla, O. (2006). The origin of fluoride in groundwater supply to Hermosillo City, Sonora, México. *Environmental Geology*, 51(1), 17–27. <https://doi.org/10.1007/s00254-006-0300-7>
- Valiantzas, J. D. (2006). Simplified versions for the Penman evaporation equation using routine weather data. *Journal of Hydrology*, 331(3–4), 690–702. <https://doi.org/10.1016/j.jhydrol.2006.06.012>
- Valdez-Moreno, G., Aguirre-Díaz, G. J., & López-Martínez, M. (1998). El volcán La Joya, Estados de Querétaro y Guanajuato-Un Estratovolcán miocénico del Cinturón Volcánico Mexicano. *Revista Mexicana de Ciencias Geológicas*, 15(2), 181–197.
- Van Der Ent, R. J., Savenije, H. H. G., Schaeffli, B., & Steele-Dunne, S. C. (2010). Origin and fate of atmospheric moisture over continents. *Water Resources Research*, 46(9), 1–12. <https://doi.org/10.1029/2010WR009127>
- Verma, S. P., & Carrasco-Núñez, G. (2010). Reappraisal of the Geology and Geochemistry of Volcán Zamorano, Central México: Implications for Discriminating the Sierra Madre Occidental and Mexican Volcanic Belt Provinces. <Http://Dx.Doi.Org/10.2747/0020-6814.45.8.724>, 45(8), 724–752. <https://doi.org/10.2747/0020-6814.45.8.724>
- Vitòria, L., Soler, A., Canals, À., & Otero, N. (2008). Environmental isotopes (N, S, C, O, D) to determine natural attenuation processes in nitrate contaminated waters: Example of Osuna (NE Spain). *Applied Geochemistry*, 23(12), 3597–3611. <https://doi.org/10.1016/j.apgeochem.2008.07.018>
- Webb, E. K. (1966). A pan-lake evaporation relationship. *Journal of Hydrology*, 4, 1–11.
- Welhan, J. A., & Fritz, P. (1977). Evaporation pan isotopic behavior as an index of isotopic evaporation conditions. *Geochimica et Cosmochimica Acta*, 41(5), 682–686. [https://doi.org/10.1016/0016-7037\(77\)90306-4](https://doi.org/10.1016/0016-7037(77)90306-4)

- Wen, X., Yang, B., Sun, X., & Lee, X. (2016). Evapotranspiration partitioning through in-situ oxygen isotope measurements in an oasis cropland. *Agricultural and Forest Meteorology*, 230–231, 89–96. <https://doi.org/10.1016/j.agrformet.2015.12.003>
- Werner, R. A., & Brand, W. A. (2001). Referencing strategies and techniques in stable isotope ratio analysis. *Rapid Communications in Mass Spectrometry*, 15(7), 501–519. <https://doi.org/10.1002/rcm.258>
- Zhang, W., Du, J., Zhou, X., & Wang, F. (2016). Mantle volatiles in spring gases in the Basin and Range Province on the west of Beijing, China: Constraints from helium and carbon isotopes. *Journal of Volcanology and Geothermal Research*, 309, 45–52. <https://doi.org/10.1016/J.JVOLGEORES.2015.10.024>
- Zimmerman, U. (1979). Determination by stable isotopes of underground inflow and outflow and evaporation of young artificial groundwater lake. In *Isotopes in lake studies*. In *Isotopes in lake studies* (pp. 97–94). Vienna: International Atomic Energy Agency.
- Zúñiga, F. R., Pacheco, J. F., Guzmán-Speziale, M., Aguirre-Díaz, G. J., Espíndola, V. H., & Nava, E. (2003). The San Fandila earthquake sequence of 1998, Querétaro, México: activation of an undocumented fault in the northern edge of central Trans-Mexican Volcanic Belt. *Tectonophysics*, 361(3–4), 229–238. [https://doi.org/10.1016/S0040-1951\(02\)00606-6](https://doi.org/10.1016/S0040-1951(02)00606-6)

ANEXOS

Anexo 1: Material suplementario del artículo:

Hernández-Pérez, E., Levresse, G., Carrera-Hernández, J., & García-Martínez, R. 2020. Short term evaporation estimation in a natural semiarid environment: New perspective of the Craig–Gordon isotopic model. *Journal of Hydrology*, V. 587, p. 124926.

- Datos meteorológicos.
- Resultados isotopía $\delta^2\text{H}$ y $\delta^{18}\text{O}$ en agua de lluvia.
- Resultados isotopía $\delta^2\text{H}$ y $\delta^{18}\text{O}$ en vapor atmosférico.
- Resultados isotopía $\delta^2\text{H}$ y $\delta^{18}\text{O}$ en agua superficial.
- Cálculos y resultados de fracción evaporada modelo Craig-Gordon-Gonfiantini.
- Cálculos y resultados de evaporación Dalton-Penman.

Descargar el material suplementario en el siguiente link:

<https://www.sciencedirect.com/science/article/abs/pii/S0022169420303863>

Anexo 2: Material suplementario del artículo:

Eliseo Hernández-Pérez, Gilles Levresse, Jaime Carrera-Hernandez, Claudio Inguaggiato, Marina Vega-González, Fernando Corbo-Camargo, Dora Carreón-Freyre, Andrea Billarent-Cedillo, Francisco Javier Sancén Contreras, Paola. Physicochemical impact of geothermal input in shallow volcanic groundwater in Central México. *Hydrogeology Journal*,

- Identificación de procesos geoquímicos en el agua subterránea mediante métodos gráficos de $\delta^{13}\text{C}$ and ^{14}C .
- Fechamiento mediante radiocarbono y modelos de corrección de fechamiento ($\Delta^{14}\text{C}$).
- Cálculos y resultados de los modelos de Corrección de edades de radiocarbono (Mook, Pearson y F&G).
- Análisis de Componentes Principales (PCA) y modelo de mezcla de aguas subterráneas.

Descargar el material suplementario en el siguiente link:

<https://link.springer.com/article/10.1007/s10040-022-02536-y>

Anexo 3: Material Suplementario del artículo:

Andrea Billarent Cedillo, Eliseo Hernández-Pérez, Gilles Levresse, Claudio Inguaggiato, Luca Ferrari, Salvatore Inguaggiato, 2022. Mantellic degassing of helium in an extensional active tectonic setting at front of magmatic arc (Central México). *Geosphere*.

- Datos fisicoquímicos e isotópos de $\delta^{18}\text{O}$ and $\delta^2\text{H}$ de lluvia, manantiales y agua subterránea en los acuíferos de Celaya Querétaro y San Juan del Río.

Descargar el material suplementario en el siguiente link:

<https://doi.org/10.1130/GEOS.S.21513981>